DTU Vindenergi

# The Wave Loads project

Henrik Bredmose, Jesper Mariegaard
Bo Terp Paulsen, Bjarne Jensen, Signe Schløer,
Torben Juul Larsen, Taeseong Kim and Anders
Melchior Hansen

DTU Wind Energy
DHI
DTU Mechanical Engineering

DTU Wind Energy Report E–0045
December 2013

DTU Vindenergi
Institut for Vindenergi

**Author:** Henrik Bredmose, Jesper Mariegaard, Bo Terp Paulsen, Bjarne Jensen, Signe Schløer, Torben Juul Larsen, Taeseong Kim and Anders Melchior Hansen

**DTU Wind Energy E–0045**

**Title:** The Wave Loads project

**Department:** Wind Energy

**Dec 2013**

**ISBN** 978-87-92896-77-3

Technical University of Denmark
DTU Wind Energy
P.O.Box 49
4000 Roskilde
Denmark
Telephone +45 4677 5085
savi@dtu.dk

# Preface and acknowledgements

'The Wave Loads project' (2010-2013) was a three-year research project with the purpose to establish more accurate models for wave loads on offshore wind turbines. 'Wave loads' was carried out collaboratively by DTU Wind Energy, DTU Mechanical Engineering and DHI.

'Wave Loads' was funded by the ForskEL programme under grant ForskEL-10495 by Energinet.dk. Additional funding was provided by Statkraft under the Statkraft Ocean Energy Research Program, and from internal funding at DHI and DTU. The funding provided a fantastic opportunity for the participants to advance the knowledge and tools for wave loads on offshore wind turbines. The funding and cooperation of the funding bodies is gratefully acknowledged.

An advisory board with participation of Niels Jacob Tarp Johansen (DONG Energy), Erik Asp Hansen (DNV KEMA), Jørgen Ranum Krokstad (Statkraft) and Erik Damgaard Christensen (DTU Mechanical Engineering) was established. The advisory board met twice a year with the project partners where the research results were discussed along with future directions for the project. The Advisory board members are gratefully thanked for sharing their insight with us. Further collaboration has taken place through mutual research visits with Statkraft and two joint MSc projects with DONG. These collaborations are highly appreciated.

Many researchers have contributed to the Wave Loads project. At DTU Mechanical Engineering: Bo Terp Paulsen and Harry Bingham. At DHI: Jesper Mariegaard, Bjarne Jensen, Iris Pernille Lohmann, Xerxes Mandviwalla, Flemming Schlütter, Anders Wedel Nielsen, Hans Fabricius Hansen, Jacob Tornfeldt Sørensen and Ole Svendstrup Petersen. At DTU Wind Energy: Henrik Bredmose, Signe Schløer, Robert Mikkelsen, Stig Øye, Torben Juul Larsen, Taeseong Kim and Anders Melchior Hansen. All are thanked for their efforts in turning research needs and ideas into practical tools and quantified knowledge.

Further, collaboration with Paul Taylor, University of Oxford and Jun Zang, University of Bath on measured data for focussed wave group impacts; Ole Hededal and Rasmus Klinkvort, DTU Civil Engineering on a monopile soil model with hysteresis and Allan Engsig-Karup, DTU Compute, on the OceanWave3D wave model is gratefully acknowledged.

The present report provides a summary of the main results of the project. Detailed lists of publications, and suggestions for future work are given inside. Enjoy and make use!

On behalf of the full team

Henrik Bredmose
DTU Wind Energy
Project manager for the Wave Loads project
30 December 2013

# Contents

# 1 Introduction

Offshore wind turbines are erected at increasing depths and with increasing rotor size. Both effects add to the wave loads on the substructure and in some cases the wave loads can be dimensioning. At the same time, a reduction of the cost of energy is a necessity to realize the planned expansion of offshore wind energy in the North Sea in an efficient manner. This has been the motivation behind the Wave Loads project with the purpose to develop improved models and methods for accurate determination of wave loads on offshore wind turbines.

The present desig practice for offshore wind turbine substructures is limited to linear wave theory for irregular waves and regular wave theory for nonlinear waves. Further directionality of the waves is usually only taken into account through empirical correction factors. During the last 10 years, however, a number of advanced wave models have been developed (e.g. Madsen et al. 2003, Engsig-Karup et al. 2009) that allow computation of fully nonlinear irregular waves over varying bathemetry. A central focus of the project has been the development, application and validation of such models within the context of offshore wind energy.

The research is in line with the Danish Megavind strategy (MegaVind n.d.) that lists development of improved design models as a way to obtain decreased cost of energy. Also, investigations by the UK-driven Carbon Trust, has highlighted the need for an improved understanding of load effects from nonlinear waves for offshore wind turbines.

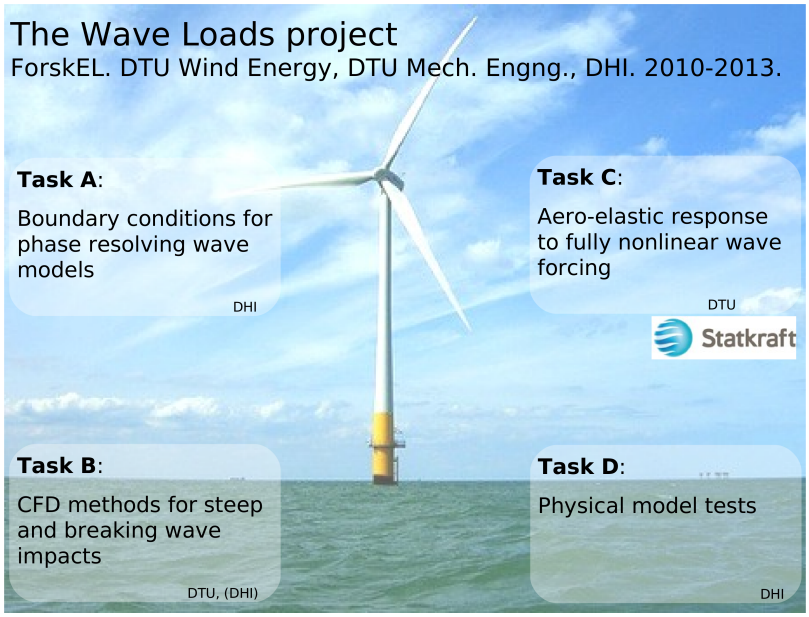


*Figure 1*: The Wave Loads project at a glance.

The research was conducted in four work packages (tasks), focussing on boundary conditions for phase resolving wave models, CFD methods for steep and breaking waves, aero-elastic response to nonlinear wave forcing and physical model tests. The four areas cover the full chain from met-ocean design data to detailed wave-structure interaction and the associated loads. A schematic overview of the project is given in figure 1.

## 1.1 Main achievements of the Wave Loads project

The main achievements and further work are outlinend below. They are described in detail in the present report and in the project publications.

**Task A: Boundary conditions for phase resolving wave models**

- Derivation of a directional second-order transfer function for the Mike 21 Boussineq wave model
- Development and implementation of second-order wave generation based on a directional spectrum from the MIKE 21 SW wave model
- Validation and applicability study of the new method that includes 2D and 3D tests with an accelerated model

**Task B: CFD methods for steep and breaking wave impacts**

- Development and validation of an efficient and fully nonlinear domain decomposed solver for wave load computations and careful verification and validation of the OpenFoam® and NS3 CFD solvers for computation of wave impacts on monopile structures
- A detailed study of the run-up from regular waves and successful comparison to the measurements of Kriebel (1992)
- A detailed study of the inline force from steep regular waves at intermediate water depth and explanation of the physical mechanism that leads to the secondary load cycle
- Computations of structural loads form uni- and multi-directional irregular waves. This includes a detailed investigation into wave loads from uni- and bi-directional phase-focused waves
- Presentation of an optimized utilization strategy of the domain decomposed solver

**Task C: Aero-elastic response to nonlinear wave forcing**

- Incorporation of fully nonlinear wave loads in the aero-elastic codes Flex5 and HAWC2 for the NREL 5MW reference wind turbine placed on a monopile and a jacket structure, respectively
- Detailed investigation of the effect of wave nonlinearity on static loads, dynamic response and lifetime fatigue damage for five combined wind-wave states. Further investigation of mis-aligned wind-wave conditions and and stand still.
- Application of CFD-based wave loads in aero-elastic computations for the monopile wind turbine and comparison to Morison-based wave loads. Assessment of response-effects from fully nonlinear directionally spread waves
- Incorporation of a new soil model with frictional damping effects into the monopile description in Flex5. Determination of hydrodynamic radiation damping for the true deflection shapes of the monopile.
- Development of a super-element formulation for the jacket substructure in HAWC2. Further, development of a consistent incorporation of added mass into the HAWC2 solver and utilization of pre-generated wave kinematics

**Task D: Physical model tests.**

- Establishment of an all-round data set for wave forces on monopile cylinders, that covers a wide range of regular and irregular 2D and 3D wave conditions
- Measurements of the structural response for a flexible cylinder, including ringing-type responses
- Successful numerical reproduction of the measurements with a CFD solver and a combined fluid-structure approach based on a potential flow wave model and a finite element solver

## 1.2 Structure of the present report

A condensed account of the results within the four workpackages are given in sections 2–6. Each section provides an introduction to the work carried out, a detailed list of achievements and then the main text on the obtained results. Suggestions for further work are given at the end of each section.

## 1.3 Publications from the Wave Loads project

A full description of the obtained results can be looked up in the full publications of the project. These are listed below.

### Journal papers

Paulsen, B. T., Bredmose, H., Bingham, H. B. & Jacobsen, N. G., 'Forcing of a bottom mounted circular cylinder by steep regular water waves at finite depth'. Submitted for publication.

Paulsen, B. T., Bredmose, H. & Bingham, H. B., 'An efficient domain decomposition strategy for violent wave loads on surface piercing circular cylinders'. Submitted for publication.

Schløer, S., Bredmose, H. and Bingham H. B. 'Fully nonlinear wave forces and their effect on monopile wind turbines. Draft paper at final stage.

### Conference proceedings papers

Bredmose, H. & Jacobsen, N. (2011), Vertical wave impacts on offshore wind turbine inspection platforms, *in* 'Proceedings of the ASME 2011 30th International Conference on Ocean, Offshore and Arctic Engineering'.

Bredmose, H., Schløer, S. & Paulsen, B. (2012), Higher-harmonic response of a slender cantilever beam to fully nonlinear regular wave forcing, *in* 'Proceedings of the ASME 2012 31th International Conference on Ocean, Offshore and Arctic Engineering'.

Bredmose, H., Slabiak, P., Sahlberg-Nielsen, L. & Schlütter, F. (2013), Dynamic excitation of monopiles by steep and breaking waves. Experimental and numerical study, *in* 'Proceedings of the ASME 2013 32st International Conference on Ocean, Offshore and Arctic Engineering'.

Christensen, E. D., Lohmann, I. P., Hansen, H. F., Haerens, P., Mercelis, P. & Demuynck, A. (2011) Irregular wave loads on a gravity based foundation in shallow water, *in* 'Proceedings of the ASME 2011 30th International Conference on Ocean, Offshore and Arctic Engineering'.

M. O. L Hansen, H. Bredmose & S. Schler (2011) 'Examples of important ongoing research topics for offshore wind energy. 4th International Conference on Computational Methods in Marine Engineering. Lisbon, Portugal, September 2011.

Hansen, H., Lohmann, I., Sørensen, J. S. & Schlütter, F. (2012), A model for long-term distribution of wave induced loads in steep and breaking shallow water waves, *in* 'Proc. of the ASME 31th 2012 Int. Conf. on Ocean, Offshore and Arctic Engng', ASME.

Larsen, T., Kim, T., Schløer, S. & Bredmose, H. (2011), Comparisons of wave kinematics models for an offshore wind turbine mounted on a jacket substructure, *in* 'Proceedings of the EWEA, Offshore 2011, Amsterdam, Netherlands'.

Nielsen, A., Schlütter, F., Sørensen, J. & Bredmose, H. (2012), 'Wave loads on a monopile in 3D waves', *in* 'Proc. of the ASME 31th 2012 Int. Conf. on Ocean, Offshore and Arctic Engng', ASME.

Paulsen, B. T., Bredmose, H. & Bingham, H. B., (2012). 'Higher harmonic hydrodynamic wave loads on a bottom fixed circular cylinder at finite water depth'. EWEA Offshore 2011, Amsterdam, The Netherlands

Paulsen, B. T., Bredmose, H. & Bingham, H. B., (2012). 'Accurate computation of wave loads on a bottom fixed circular cylinder'. International workshop for water waves and floating bodies, IWWWFB. Copenhagen, Denmark

Paulsen, B. T., Bredmose, H. & Bingham, H. B.,(2013). 'Focused wave impact on a vertical cylinder: Experiment, numerical reproduction and a note on higher harmonics'. International workshop for water waves and floating bodies, IWWWFB. Marseilles, France

Paulsen, B. T., Bredmose, H., Bingham, H. B. & Schløer, S. (2013). 'Steep wave loads from irregular waves on an offshore wind turbine foundation'. *in* 'Proceedings of the ASME 2013 32st International Conference on Ocean, Offshore and Arctic Engineering'.

Schløer, S., Bredmose, H. & Bingham, H. (2011), Irregular wave forces on monopile foundations. Effect of full nonlinearity and bed slope, *in* 'Proceedings of the ASME 2011 30th International Conference on Ocean, Offshore and Arctic Engineering'.

Schløer, S., Bredmose, H., Bingham, H. & Larsen, T. (2012), Effects from fully nonlinear irregular wave forcing on the fatigue life of an offshore wind turbine and its monopile foundation., *in* 'Proceedings of the ASME 2012 31th International Conference on Ocean, Offshore and Arctic Engineering'.

### Conference posters

Bredmose, H., Schlü tter, F., Paulsen, B. T. & Schlö er, S. (2013), 'Ringing and impulsive exication of offshore wind turbines. Results from the Wave Loads project'. Poster at EWEA Offshore 2013, Frankfurt, Germany.

Hansen, A. M., Larsen, T. J. & Yde, A. (2013), 'Influence of foundation model complexity on the design loads for offshore WTG on jacket foundation. Poster at EWEA2013.

Larsen T.J., Kim, T, Schler, S & Bredmose H. (2011) 'Comparisons of wave kinematic models for an offshore wind turbine mounted on a jacket substructure . Poster at European Offshore Wind 2011, Amsterdam, The Netherlands. Was awarded a Best poster prize.

Schløer, S., Bredmose, H., Bingham, H. B. & Larsen, T. J. (2012), 'Fully nonlinear wave foricing on an offshore wind turbine. structural response and fatigue. Poster at the 9th Deep Sea Offshore Wind R&D Seminar, Trondheim, Norway, January 2012. NOWITECH. Was awarded a shared Best poster prize.

Schløer, S., Bredmose, H., & Klinkvort, R. T. (2012), 'Nonlinear irregular wave forcing off offshore wind turbines. Effect of soil damping and misaligned wind and waves. Poster at EWEA Offshore 2013, Frankfurt, Germany.

### Technical reports

Mariegaard, J. S. (2011), Task A1: Boundary conditions for phase resolving wave models, Technical report, DHI.

DHI (2012), *Mike 21 Toolbox - Mike by DHI 2012*, chapter 14. Generation of random waves, pp. 153–170.

Mariegaard, J. S. (2013), Task A3: Study of the applicability of a new method with second order wave generation, Technical report, DHI.

Jensen, B. (2012), Technical Note on: Extreme Wave Loads and Run-up on Circular Cylinders, Technical report, DHI, Hørsholm, DK-2970.

Schlütter, F. (2013), Wave loads on offshore wind turbine foundations. experiment description, Technical report, DHI.

### PhD theses

Schløer, S. (2013), *Fatigue and extreme wave loads on bottom fixed offshore wind turbines Effects from fully nonlinear wave forcing on the structural dynamics*, PhD thesis, DTU Wind Energy.

Paulsen, B. T., (2013). *Efficient computations of wave loads on offshore structures*, PhD thesis, DTU Mechanical Engineering.

### MSc projects

Slabiak, P. & Sahlberg-Nielsen, L. (2013), *Dynamics of a monopile structure in irregular waves: Experimental and numerical investigation*, Master's thesis, DTU Wind Energy.

Bairíc, A. & Holmen, C. (2013) *Loads and structural response for focused waves*, Master's thesis, DTU Wind Energy

### BSc projects

Nielsen, J. K. & Dam, C. (2012), *Numerical reproduction of measured wave loads and response for a monopile foundation*, BSc project, DTU Wind Energy.

# 2 Task A: Boundary Conditions for Phase-Resolving Wave Models

**Jesper Mariegaard (DHI)**
with contributions from Jacob Tornfeldt Sørensen (DHI)

## 2.1 Introduction

The overall goal of the Wave Loads project was to improve the description of wave loads on offshore wind turbines and to provide accurate tools for determining these loads. The topics addressed in Task A 'Boundary conditions for phase-resolving wave models' concern the transfer of wave data obtained with macro-scale stochastic spectral wave models meso-scale deterministic phase resolving wave models that allow a more detailed wave description.

Accurately describing the waves that hit an offshore wind farm requires a downscaling technique e.g. consisting of these three steps, as illustrated in figure 2

**Macro** Long-term (30 years) metocean statistics provided by phase-averaged models e.g. a MIKE 21 Spectra Wave (SW) on macro scale (1000 km to 1 km).

**Meso** More detailed modelling including the non-linear wave transformation of a few design giving storms of 3-6 hours in a deterministic phase-resolving wave model e.g. MIKE 21 Boussinesq Waves (BW) by DHI or OceanWave3D by DTU. The domain size could be in the order of 1-10 km.

**Micro** The most complex, highly non-linear effects like wave breaking and run-up are modelled for single waves or groups of waves in CFD models (1-10 minutes) or in physical scale tests (typically 3 hours).

The wave generation in the phase-resolving wave model should be based on relevant sea states retrieved from the long-term SW modelling of the linear waves. The current practice is to use first-order generation based on 1D spectra (e.g. JONSWAP) and a spreading function (e.g. $\cos^n$). But often in real applications the wave climate consists naturally of multiple dominant wave directions and in many cases the generation boundary cannot be positioned at adequately deep waters to justify linear wave generation.

The objective of Task A has been to improve the utilization of results from spectral wave models that include nonlinear shoaling and refraction of waves over varying bed-topography. This allows an improved description of wave fields with interacting components from swell and storm waves. It has been a central aim to include the developments into the MIKE by DHI tool for random wave generation, RanWave, which is part of MIKE 21 Toolbox, to allow direct application by external users and in consultancy.

### 2.1.1 Main achievements

The main achievements of the work are

- Derivation of a directional second-order transfer function for the Mike 21 Boussineq wave model development of of second-order wave generation based on a directional spectrum from MIKE 21 SW
- Implementation into the Mike 21 RanWave tool
- Validation and study of second-order wave generation

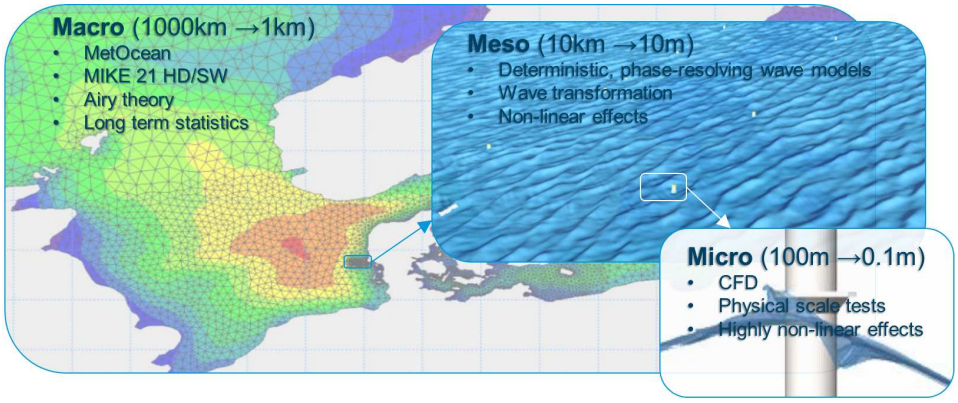


*Figure 2*: Downscaling from macro over meso to micro scale.

- Applicability of the new method in terms of 2D and 3D tests with an accelerated model

A condensed presentation of the results is provided in the following. Detailed desciptions of the work is provided in the following documents that are linked to the three subtasks A1-A3:

A1 Method statement and theory Mariegaard (2011)

A2 Implementation in MIKE by DHI DHI (2012)

A3 Study of the applicability of the new method Mariegaard (2013)

## 2.2 Second-order wave generation

Second-order waves consist of first-order waves and second-order correction terms which are small in deep waters but increase in size as the water depth decreases. The second-order corrections consist of sub-harmonics, which are bound long waves seen as a set-down under energetic wave groups, and super-harmonics, which affect the shape of individual waves making them steeper with higher crests and flatter troughs.

The theory of second-order wave generation for directional Stokes waves was described by Sharma and Dean in Sharma & Dean (1981) while the second-order theory for generation of unidirectional Boussinesq waves was developed by Madsen and Sørensen in Madsen & Sørensen (1993). Task A1 of this project generalised second-order Boussinesq wave generation to directional waves Mariegaard (2011).

Applying a Stokes expansion technique to the governing equations for the wave motion allows the derivation of the second-order solution for a bichromatic wave pair (see e.g. Sharma & Dean (1981)). The solution for the pair $s_n$ and $s_m$ of wave components $s_j(t,\mathbf{x}) = A_j e^{i\psi_j} + c.c.$ where $\psi_j = \omega_j t - \mathbf{k}_j \cdot \mathbf{x}$ and $\omega_j = 2\pi f_j$ is the angular frequency and $\mathbf{k}_j$ is the wave number vector has a first order part

$$\eta^{(1)}(t,\mathbf{x}) = s_n + s_m \tag{1}$$

and a second-order part

$$\eta^{(2)}(t,\mathbf{x}) = s^-_{mn} + s^+_{mn} + s^+_{2m} + s^+_{2n} \tag{2}$$

where the sub (-) and super (+) harmonics (bound waves) are defined as

$$s^{\pm}_{mn} = G^{\pm}_{mn} A_m A_n e^{i\psi^{\pm}_{mn}} + c.c., \quad \psi^{\pm}_{mn}(t,\mathbf{x}) = (\omega_n \pm \omega_m)t - (\mathbf{k}_n \pm \mathbf{k}_m)\cdot\mathbf{x} \tag{3}$$

The second-order bichromatic transfer function for Stokes waves originally derived by Sharma & Dean (1981) but here in the notation of Bredmose et al. (2005) (with minor adjustments) reads

$$G^{\pm}_{mn} = \frac{2-\delta_{mn}}{g}\left((\omega_n \pm \omega_m)\frac{H_{n,\pm m}}{D_{n,\pm m}} - L_{n,\pm m}\right) \tag{4}$$

where $\delta_{mn}$ is the Kronecker delta and

$$H_{n,m} = (\omega_n+\omega_m)\left(\omega_n\omega_m - \frac{g^2\mathbf{k}_n\cdot\mathbf{k}_m}{\omega_n\omega_m}\right) + \frac{1}{2}(\omega_n^3+\omega_m^3) - \frac{g^2}{2}\left(\frac{|\mathbf{k}_n|^2}{\omega_n}+\frac{|\mathbf{k}_m|^2}{\omega_m}\right) \tag{5}$$

$$D_{n,m} = g|\mathbf{k}_n+\mathbf{k}_m|\tanh(|\mathbf{k}_n+\mathbf{k}_m|h) - (\omega_n+\omega_m)^2 \tag{6}$$

$$L_{n,m} = \frac{1}{1}\left(\frac{g^2\mathbf{k}_n\cdot\mathbf{k}_m}{\omega_n\omega_m} - \omega_n\omega_m - (\omega_n^2+\omega_m^2)\right) \tag{7}$$

In the expressions for $H$, $D$ and $L$ the convention $\omega_{-m} = -\omega_m$ and $\mathbf{k}_{-m} = -\mathbf{k}_m$ is used for $n,-m$.

Similarly, a second-order bichromatic transfer function exists for Boussinesq waves (see Madsen & Sørensen (1993) and Mariegaard (2011)). The directional second-order bichromatic Boussinesq transfer function derived in Mariegaard (2011) reads

$$G^{\pm}_{mn} = \frac{g}{\beta_0}\mathbf{k}_p\cdot\mathbf{k}_p + \frac{\omega_n\omega_m\left(k_{nx}k_{my}(\frac{k_{ny}}{k_{nx}}+\frac{k_{mx}}{k_{my}}) + k_{ny}k_{mx}(\frac{k_{my}}{k_{mx}}+\frac{k_{nx}}{k_{ny}}) \pm 2\mathbf{k}_n\cdot\mathbf{k}_m\right)}{h\beta_0\mathbf{k}_n\cdot\mathbf{k}_m} \tag{8}$$

where $\mathbf{k}_p = \mathbf{k}_n \pm \mathbf{k}_m$ and the subscript $nx$ on $k_{nx}$ denotes the $x$ component of the vector $\mathbf{k}_n$ and so forth. $\beta_0$ is defined by

$$\beta_0 \equiv \omega_p^2 - gh|\mathbf{k}_p|^2 - Bg^3|\mathbf{k}_p|^4 + (B+\tfrac{1}{3})h^2\omega_p^2|\mathbf{k}_p|^2. \tag{9}$$

Unfortunately, this transfer function has not been fully validated (see future work below) and consequently, for the study of the applicability of the new method Stokes theory was used.

The second-order solution for a general irregular sea is obtained by summing over all bichromatic pairs. The algorithm is explained in Section 2.3.3.

## 2.3 Implementation in MIKE by DHI

The goal of Task A2 was to implement the new features in the RanWave tool in the MIKE by DHI software framework. This was done in 2012 and released with MIKE by DHI in October 2012 DHI (2012).

The overall steps in the wave generation with RanWave are the following:

a. Input: Read input from configuration file and optionally read data from dfs file (e.g. spectrum or time series).

b. Initialize: Make vector of discrete frequencies **f** based on the length of the requested output time series.

c. Spectrum: Make spectral energy vector **Sf** corresponding to **f** (from generic spectrum or loaded from file—see below).

d. Wave number: Compute corresponding wave numbers and store in **k**.

e. Coefficients: Make coefficient vector **A** based on **Sf** and random phases.

f. Directions: For each discrete frequency determine one random direction from the cumulative directional distribution and store all in **d** (single summation).

g. Synthesis: For each point on the generation line determine the final $(x,y)$-dependent coefficients and make time series by inverse FFT. Optionally: add second-order corrections (see below) to $(x,y)$-coefficients.

h. Save: store results in dfs files.

### 2.3.1 An algorithm for import of directional spectra

The typically coarse directional spectrum needs to be loaded from file and then interpolated and directionally integrated to obtain the (fine) spectral energy vector **Sf** corresponding to **f**. The coarse directional spectrum is also kept for later selection of directions (see Section 2.3.2).

1. The directional spectrum $S$ is read from a dfs2 file and stored in a two-dimensional array **Sftht** (and nullified outside the user-selected directional bounds $\theta_{min}$ to $\theta_{max}$).
2. A directional array $\theta$ with user-selected $\theta_{min}$ to $\theta_{max}$ is initialized
3. For each discrete frequency $f_j$ do:
   (a) loop over directions $\theta_n$ and determine the spectral energy $S(f_j,\theta_n)$ by bilinear interpolation in **Sftht** and temporarily store in vector **D**.
   (b) Directionally integrate **D** to obtain frequency spectral component $Sf_j$.

### 2.3.2 An algorithm for selecting directions

In the single summation method (see e.g. Sand & Mynett (1987)) used in RanWave each frequency component has only one direction which is randomly determined from the directional distribution. The below algorithm cover the most general case where the directional distribution varies with frequency.

For each frequency component $f_j$ do the following to determine the corresponding direction $d_j$

1. Initialize the directional sector array $\theta$ going from the user-selected $\theta_{min}$ to $\theta_{max}$.
2. Determine the probability distribution function **pdf** corresponding to $\theta$ for this frequency $f_j$ by bilinear interpolation in the directional input spectrum **Sftht**.
3. Compute the cumulative distribution function **cdf** by taking the antiderivative of **pdf** and add integration constant and normalize so it goes from 0 to 1.
4. Get random number between 0 and 1.
5. Find the corresponding direction $d_j$ by linear interpolation in **cdf**.

### 2.3.3 An algorithm for second-order wave generation

The synthesis of second-order waves is carried out for each point $p_n$ with coordinates $(x_n,y_n)$ on the generation line by the following procedure.

1. Determine primary $(x,y)$-coefficients (first order) based on **A**.
   For each discrete frequency component $f_j$ do
   (a) Compute the inner product $\mathbf{k}_j \cdot \mathbf{x}_n$ (note $\mathbf{k}_j$ has a random direction—see above)

(b) Determine coefficients for surface elevation by multiplying the coefficient $A_j$ by the $(x,y)$-dependent part $e^{-\mathbf{k}_j \cdot \mathbf{x}_n}$

(c) Determine the coefficients for surface slope and wave flux by multiplying the coefficients of (b) by $\omega_j/|\mathbf{k}_j|$ and $|\mathbf{k}_j|$, respectively, and projecting onto the normal of the wave generation line.

2. Determine sub-harmonic $(x,y)$-coefficients (second order).
   For each sub-harmonic frequency candidate $f_p$ do
   For each frequency component $f_i$ do

   (a) Denote $f_j = f_i + f_p$ and find $\mathbf{k}_p = \mathbf{k}_j - \mathbf{k}_i$.

   (b) Compute transfer function $G_{ji}^-$

   (c) Compute the inner product $\mathbf{k}_p \cdot \mathbf{x}_n$

   (d) Determine corrections to primary $(x_n,y_n)$-coefficients in the same way as in 1(b) and 1(c) but using $A_p = A_j A_i$ and the wave number vector $\mathbf{k}_p$. Add corrections to the primary coefficients.

3. Determine super-harmonic $(x,y)$-coefficients (second order) in the same way as sub-harmonic coefficients but loop only over super-harmonic candidates and let $p = j + i$ and use the transfer function $G_{ji}^+$.

## 2.4 A study of the applicability of a new method

The purpose of Task A3 was to study the applicability and limitations of the new methodology for wave generation and to compare it to the existing methodology.

### 2.4.1 Existing approach

The downscaling described in the introduction contains long-term wave modelling in deep waters by means of a phase-averaging wave model like MIKE 21 SW. Relevant sea states are retrieved from this model either as bulk parameters ($H_s$, $T_p$) or frequency spectra ($S(f)$).

In a phase-resolving wave model like MIKE 21 BW, a wave generation line is placed at sufficiently deep waters to justify linear wave generation. Random linear waves based on selected sea states are generated from a standard spectrum (e.g. from $H_s$, $T_p$) or from a frequency spectrum ($S(f)$) from MIKE 21 SW. If directional waves are wanted a prescribed spreading function is applied. The non-linear shoaling of the waves is carried out on a sloping bathymetry in the MIKE 21 BW model.

### 2.4.2 New approach

By the improvements to the random wave generation tool, RanWave, of MIKE 21 ToolBox described in Task A1 and implemented in Task A2 in this project, it is now possible to improve the current downscaling practice in two ways.

1. More direct use of SW results including full directional information.

2. Decreasing the model domain size due to second-order wave generation which means that less shoaling is necessary inside MIKE 21 BW and hence the wave generation may be positioned in shallower water. It also means less computational time or alternatively higher model resolution with same computational effort.

### 2.4.3 An offshore wind farm case

In order to study the applicability of the new methodology a BW model with a 700-by-700 m basin (plus a 250 m thick surrounding sponge layer) with a 1:25 slope going from h=30 m to h=16.8 m was set up. The layout, of which a side view can be seen in Figure 3 (top), corresponds

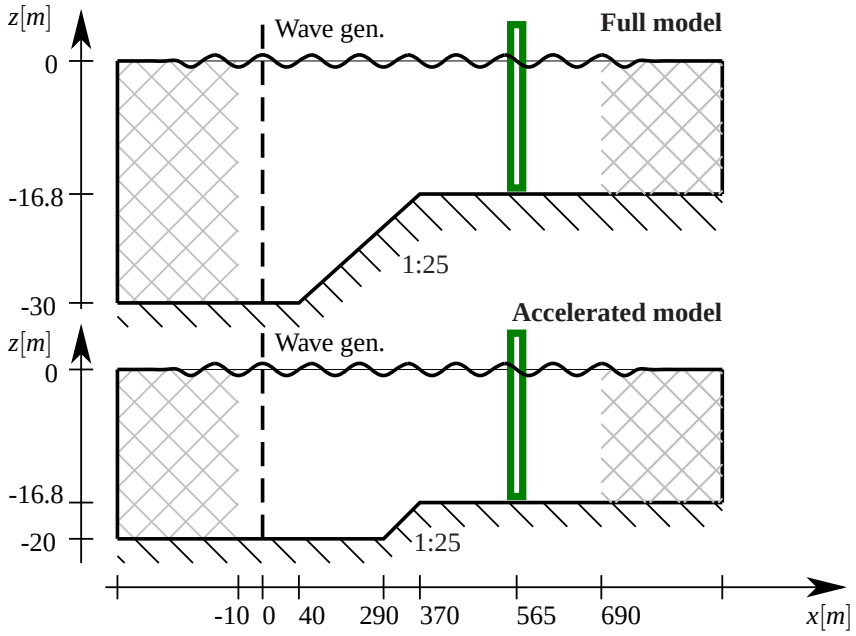


*Figure 3*: The full (top) and accelerated (bottom) models studied in Task A3.

to the physical scale model layout used in Task D of the wave loads project (scale 1 : 36.6).

### 2.4.4 Method of study

The Task A3 study Mariegaard (2013) of the new methodology compared to the existing approach featured two BW models:

(1) Full model with 1st order waves generated at $h = 30\ m$ (Figure 3 (top)).

(2) Accelerated model with 2nd order waves at $h = 20\ m$ (Figure 3 (bottom)).

Note that the generation line of the accelerated model is positioned at the same place as in the full model for comparability reasons only. In a ”true” accelerated model the generation line would be positioned with same distance to the beginning of the slope as in the full model and the domain size would be correspondingly smaller.

The study consisted of three parts:

I First and second-order wave generation

II Full and accelerated BW models with *uni*directional waves (flume)

UniH4T10. JONSWAP $H_s = 4\ m$, $T_p = 10\ s$.

UniH4T12. JONSWAP $H_s = 4\ m$, $T_p = 12\ s$.

UniH4T14. JONSWAP $H_s = 4\ m$, $T_p = 14\ s$.

UniH6T12. JONSWAP $H_s = 6\ m$, $T_p = 12\ s$.

III Full and accelerated BW models with *directional* waves (basin) generated from directional spectra (see Figure 4) from a SW model forced with a standard JONSWAP spectrum and a $\cos^n$ directional distribution with $n = 12.5$. This model performs the linear shoaling and refraction of the directional wave fields.

DirH4T14. JONSWAP $H_s = 4\ m$, $T_p = 14\ s$.

DirH6T12. JONSWAP $H_s = 6\ m$, $T_p = 12\ s$.

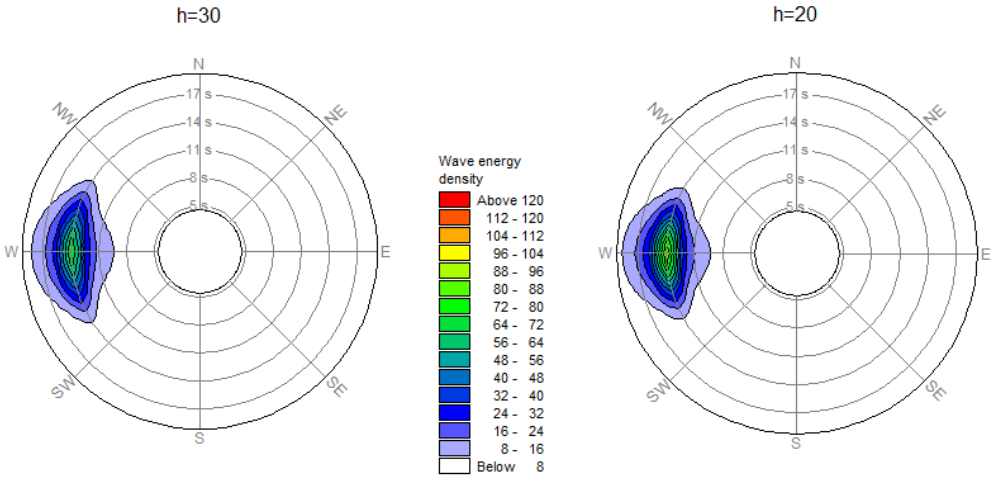


*Figure 4*: Test DirH4T14: Directional spectra obtained from MIKE 21 SW at two different depths.

### 2.4.5 Selected results (DirH4T14)

The directional SW-spectra used as input to the wave generation for the two BW models in the Test DirH4T14 can be seen in Figure 4. Waves were generated according to the procedures described in Section 2.3. Summary figures can be seen in Table 1. Notice that although called

*Table 1*: Summary of the generated waves applied to the basin test DirH4T14. $h$[m] is the water depth, $kh$[-] the relative depth, $Ur = HL^2/h^3$[-] the Ursell number, $T_{cut}$ is the cut-off period (waves with shorter periods are nullified), $|\partial_t \eta|_{99.9}$[m/s] the 99.9th percentile surface slope, $H_s$[m] the significant wave height, $H_{99}$[m] the 99th percentile wave height.

| Series | $h$ | order | $kh$ | $Ur$ | $T_{cut}$ | $\lvert\partial_t\eta\rvert_{99.9}$ | $H_s$ | $H_{99}$ |
|---|---|---|---|---|---|---|---|---|
| DirH4T14(1) | 30 | 1st | 0.88 | 6.87 | 8.5 | 1.62 | 4.09 | 5.74 |
| DirH4T14(2) | 20 | 2nd | 0.69 | 16.67 | 6.5 | 2.24 | 4.21 | 5.82 |

H**4**T14 the significant wave height is $H_s = 4.09\ m$ at $h = 30\ m$ which is due to scaling intended to match $H_s$ at $h = 20\ m$. See full study Mariegaard (2013) for details. Notice also that a larger cut-off period $T_{cut} = 8.5\ s$ ($f_{cut} = 0.117$) was needed in the deeper full model to keep the computations stable. This has an effect of the spectral tail of the results—see Figure 6.

Figure 5 showing the wave height distributions, Figure 6 showing the spectra, and Table 2 at the pile indicate that the accelerated model performs quite well compared to the full model. Both significant and extreme waves are well produced in the accelerated model as is the extreme 99th percentile crest height which is of great importance in offshore applications.

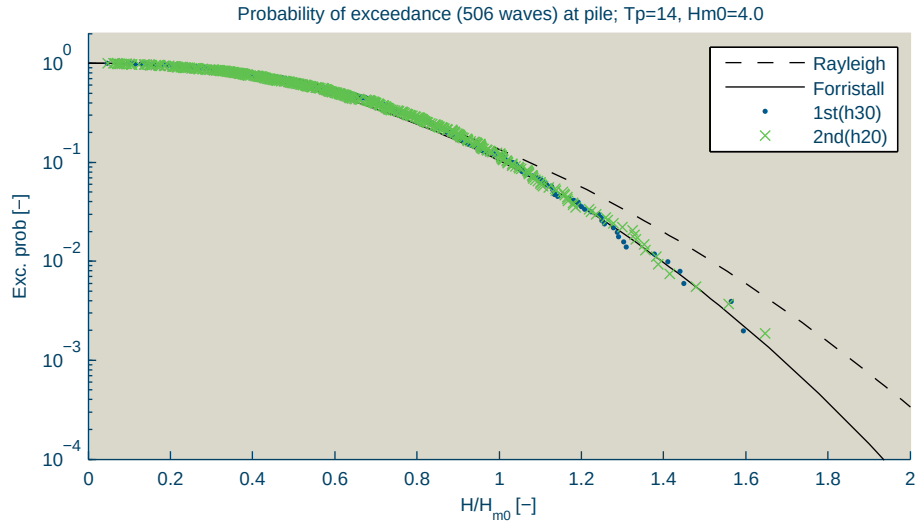


*Figure 5*: Test DirH4T14: Probability of exceedance for relative wave heights at pile position ($h = 16.8\ m$) compared to Rayleigh (dashed line) and Forristall (solid line) distributions.

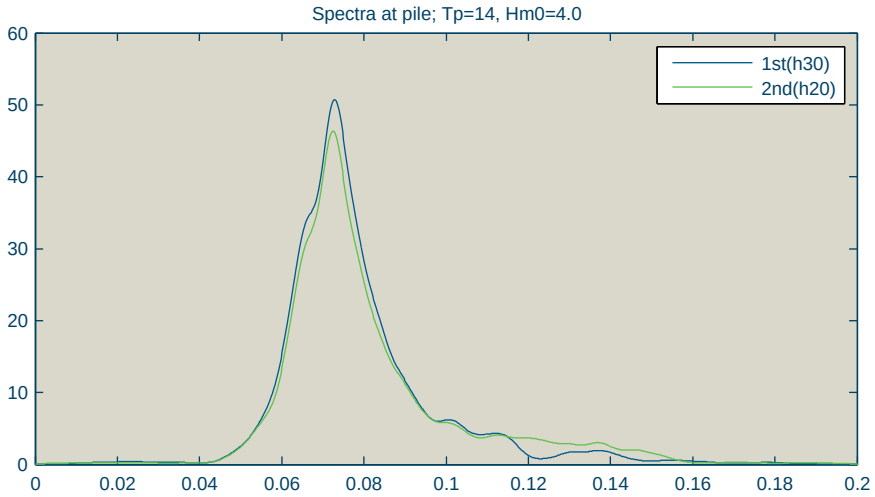


*Figure 6*: Test DirH4T14: Wave spectra at pile position.

*Table 2*: Results at pile position for test DirH4T14. $|\partial_t \eta|_{99.9}$[m/s] the 99.9th percentile surface slope, $H_s$[m] the significant wave height, $H_{99}$[m] the 99th percentile wave height, and $Cr_{99}$[m] the 99th percentile crest height.

| Series | $\|\partial_t \eta\|_{99.9}$ | $H_s$ | $H_{99}$ | $Cr_{99}$ |
|---|---|---|---|---|
| DirH4T14(1) | 2.03 | 4.40 | 6.02 | 3.71 |
| DirH4T14(2) | 2.13 | 4.31 | 5.91 | 3.64 |

## 2.5 Summary of study findings

The study Mariegaard (2013) featured a number of tests as explained in Section 2.4.4. A summary of experiences and conclusions from these tests are listed below.

### Second-order wave generation

It is well known that the second-order contributions increase with wave height and period.

- When outside the second-order validity criteria $H < H_B/4$ ($H_B = 0.8h$) and $Ur = HL^2/h^3 <$ 26 secondary waves start to appear which can be seen as an increase in the 2nd/1st ratio of 99th percentile wave height.
- The relative 99th percentile crest height (2nd/1st) increase with wave height but only to a minor extent with period.
- The 99.9th percentile surface slope increases significantly with second-order contributions - up to 50% still within the validity range of second-order theory.
- Skewness is surprisingly small for unidirectional waves due to a singular behaviour of the transfer function.

#### Unidirectional tests in full and accelerated models

- At water depths of $h = 30$ to 20 $m$ only seas with long waves have significant second-order contributions.
- The spatial distribution of skewness indicates that the model responds negatively to the applied waves both in the first- and second-order cases (in theory second-order waves should ”fit” better to the model and hence be ”accepted” without the release of spurious waves).
- A tendency towards underestimation of the extreme crest heights seems present in the accelerated (second order) tests compared to the full model most likely due to an overestimation of the sub-harmonics.

#### Directional tests in full and accelerated models

- The transfer of directional spectra from MIKE 21 SW was carried out succesfully.
- The accelerated model performs better than in the unidirectional case and predict extreme crest heights well probably due to the smaller subharmonic content of directional seas.

## 2.6 Conclusion

Task A provided two improvements to the random wave generation tool in MIKE 21: 1) wave generation based on directional spectra from MIKE 21 SW, 2) second-order wave generation. Both features have been implemented and released with MIKE by DHI 2012. A study of a new approach with an accelerated model with second-order generation compared to the existing approach with first-order generation in a full model has been conducted for an offshore wind farm case.

Second-order wave generation is mainly relevant in shallow water. Hence, this tool is mostly relevant for wind farms placed in shallow water. For offshore wind farms in deep to intermediate depth water second-order wave contributions will be small for typical storm situations (e.g. $H_s = 7$ $m$ and $T_p = 9$ $s$).

In relevant environments, the benefits of using a smaller accelerated BW model with second-order wave generation instead of a larger model with wave shoaling from greater depth are obvious. Modelling of Boussinesq waves is depth restricted ($kh$) and a less deep Boussinesq model is more stable and can be run with larger time steps and smaller cut-off period $T_{cut}$. Furthermore, a smaller model is computational cheaper.

## 2.7 Suggestions for further work

The following developments are suggested for further work on wave generation for phase-resolving wave models:

**Directional Boussinesq transfer** Verification and validation of second-order directional Boussinesq transfer function presented in Mariegaard (2011).

**3D wave generation** Extending the wave generation tool to also outputting wave kinematics and thereby providing boundary conditions also for 3d CFD-type phase-resolving wave models.

**Double summation method revisited** The presented wave generation tool is in the directional case based on the so-called single summation technique (see e.g. Sand & Mynett (1987)) preferred in the 80s and 90s partially due to restricted computational power as the alternative double summation method require are large number of terms in the synthesis to avoid phase-locking Sand & Mynett (1987). Computers nowadays are, however, much more powerful and it could be interesting to re-study and compare the results of single and double summation in this light.

**Wave generation with spatial variation** In models with large geographical extent, e.g. 10 km, assuming constant wave conditions (spectrum) along the generation line is, in some cases, unrealistic and unsatisfactory. It is not trivial how to include spatially varying wave conditions along the wave generation line, but it could be an important topic of a future project.

**Time-varying wave generation** In long time simulations the assumption on stationarity is questionable. A good topic of a future project could be how to include time-varying wave generation.

**Wave generation at varying depth** Finally, one of the most limiting conditions with current day wave generation is the requirement of constant depth which is hard to justify and accommodate on real bathymetries. A future project should address wave generation along varying depths.

# 3 Task B: CFD methods for steep and breaking wave impacts

**Bo Terp Paulsen (DTU Mechanical Engng.) and Bjarne Jensen (DHI)**
with contributions from Henrik Bredmose, Harry Bingham and Niels Gjøl Jacobsen

## 3.1 Introduction

In recent years computational fluid dynamics (CFD) has become an important supplement to physical model tests for the investigation of wave-structure interaction. The advantage of CFD is that prototypes and complicated bathymetries are easily tested. Furthermore, the high resolution in space and time of the CFD-computations makes it possible to study detailed flow phenomena, which might be difficult to investigate from model tests.

Traditionally, computations of realistic multi-directional irregular waves have been a challenge due to the large computational domains needed and the associated computational cost. Further, due to complexities involved in tracking the motion of the free surface numerical diffusion might be a problem in some implementations. To address these issues a domain decomposed solver was developed as a part of the Wave Loads project. Here, a fully nonlinear potential flow solver was combined with a Navier-Stokes solver.

The new solver enables computations of wave loads from realistic multi-directional irregular waves. For these sea states, wave impacts from steep and breaking waves are of particular concern as they may lead to either “ringing”, “springing” or slamming responses. These phenomenons all have the potential to significantly reduce the structural life time or cause failure. Due to the high accuracy of the domain decomposed solver it can be used for benchmarking of simpler models. The coupled solver has been validated against regular and irregular waves in 2D and 3D. The CFD model and combined solver has further been used to carry out a systematic study of forcing from steep regular waves and bi-directional wave groups.

### 3.1.1 Main achievements

The main achievements of the task can be summarized as

- Careful verification and validation of the OpenFoam® and NS3 CFD solvers for computation of wave impacts on monopile structures
- Development and validation of an efficient and fully nonlinear domain decomposed solver for wave load computations
- A detailed study of the run-up from regular waves and successful comparison to the measurements of Kriebel (1992)
- A detailed study of the inline force from steep regular waves at intermediate water depth
- An explanation of the physical mechanism that leads to the secondary load cycle
- Computations of structural loads form uni- and multi-directional irregular waves
- A detailed investigation into wave loads from uni- and bi-directional phase-focused waves
- Presentation of an optimized utilization strategy of the domain decomposed solver

The work has been published in 2 journal articles (Paulsen, Bredmose, Bingham & Jacobsen 2013, Paulsen, Bredmose & Bingham 2013); six conference papers (Bredmose & Jacobsen

2011, Christensen et al. 2011, Paulsen et al. 2011, 2012, Paulsen, Bredmose & Bingham 2013, Paulsen, Bredmose, Bingham & Schløer 2013), one Ph.d. thesis (Paulsen 2013) and one technical report (Jensen 2012).

### 3.1.2 Structure of section

The reminder of this chapter is organized as follows. First in section 3.2 an initial validation of the Navier-Stokes solver is presented. In section 3.3 the principal of the newly developed domain decomposed solver is outlined and two of the test-cases from Paulsen, Bredmose & Bingham (2013) are shown. In section 3.4, parts of the discussion of "ringing" wave loads from steep near breaking wave is repeated. Originally this study was published in Paulsen, Bredmose, Bingham & Jacobsen (2013). This section includes a comparison with the Morison equation and analytic higher order wave loads theories. Finally, selected results from the discussion of uni - and bi-directional phase focused wave groups are presented in section 3.5. A summary of the obtained results and findings are given in section 3.6.

## 3.2 Initial validation of the numerical solvers

### 3.2.1 Forces on vertical cylinders

For estimating the force on a body one approach is to apply the numerical model to simulate the loads directly on the structure i.e. the structure is included and resolved in the numerical grid. This methodology has been described and compared to conventional design methods for mono-piles in terms of the Morison-equation in Christensen et al. (2007) where the NS3 code was used. The NS3 code has further been applied for loads on gravity based wind turbine foundation as described in Bredmose et al. (2006). Other structural applications have been reported in Mayer and Nielsen (2005) in terms of loads on rectangular beams and in Nielsen & Mayer (2004) where green water incidents on a ship deck were investigated. Based on the solid background of the NS3 code a reference simulation has been prepared in terms of wave loads on a vertical cylinder exposed to very steep non-linear waves. These results are used for comparison with the OpenFOAM model. The OpenFOAM model has recently been applied in combination with waves2Foam for simulation of wave impact on offshore wind turbine foundations as presented in Bredmose & Jacobsen (2010) and for wave loads on inspection platforms shown in Bredmose & Jacobsen (2011). All results are in the following furthermore compared to loads predicted by the Morison-equation.

A test case has been setup with the following characteristics. Cylinder diameter, $D = 6$ m, wave height, $H = 15.14$ m, wave period, $T = 11.75$ s, water depth, $h = 30$ m. The waves are generated as stream function waves and will for this case results in a Keulegan-Carpenter number of KC$= 15$ and a Reynolds number of Re$= 4.7 * 10^7$.

A rectangular model domain has been setup with a total length of 800 m. At the inlet and outlet boundary a relaxation zone with a length of 200 m is used for generating and absorbing the waves respectively. In the vertical direction uniform grid spacing is applied with a resolution at 0.86 m. In the horizontal direction grid refinement is applied near the cylinder with a minimum resolution at 0.5 m. A total of approximately $800,000$ computational cells are applied. Forces on the cylinder are computed by integrating the pressure over the entire cylinder surface.

Figure 7 presents the results of the NS3 simulation in terms of in-line forces on the cylinder. The force variation follows with good agreement the previous results reported for mono-piles in Christensen et al. (2007). Furthermore the loads are calculated based on the Morison-equation in combination with the theoretical wave kinematic found from stream function theory. The comparison is also shown in Figure 7 where good agreement is found. The load coefficients

applied in the Morison-equation are $C_D = 0.7$ and $C_M = 1.7$.

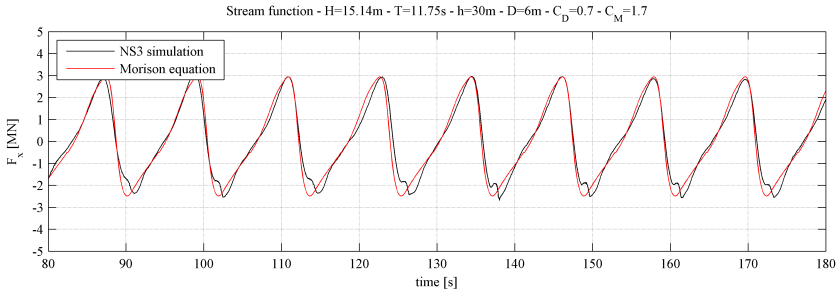


*Figure 7*: In-line forces from the NS3 simulation compared to Morison equation with stream function theory. $H = 15.14$ m, $T = 11.75$ s.

Following the reference simulation with the NS3 code a corresponding simulation is performed with the OpenFOAM code. The computational domain is identical to that applied for the NS3 simulations. The waves2Foam frame work is applied to generate a stream function wave with the same characteristics. The results are presented in Figure 8 as both the in-line forces on the cylinder as well as the surface elevation upstream the cylinder. Comparing to the NS3 results in Figure 7 it is seen how the forces show a very similar variation over time. Also the comparison to Morison-equation shows good agreement for the OpenFOAM model. It is noted that slightly higher forces are found in the OpenFOAM model compared to the NS3 model. The explanation for this is not found yet but it should be mentioned that the deviation is of a size where it cannot be conclusively determined whether the NS3 results or the OpenFOAM results are most correct. However the overall impression is that both models are capable of reproducing the forces within an acceptable accuracy.

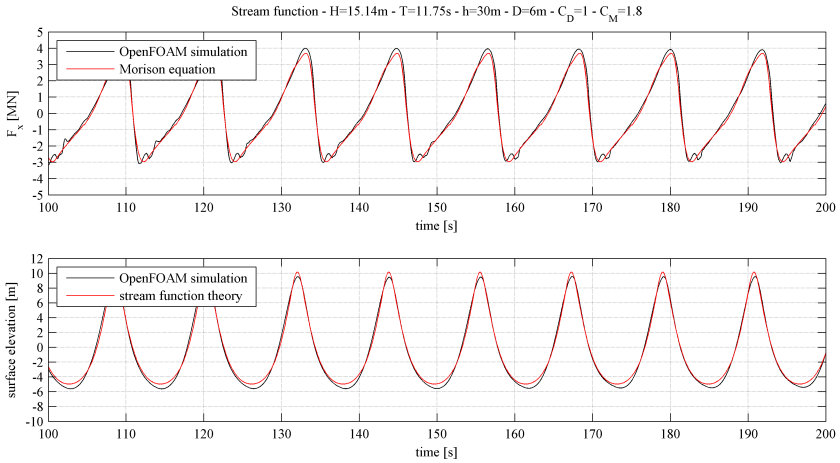


*Figure 8*: Results from the OpenFoam simulation compared to Morison equation with stream function theory. Top panel: in-line forces, bottom panel: surface elevation upstream cylinder. $H = 15.14$ m, $T = 11.75$ s.

### 3.2.2 A note on near-surface kinematics

The above results show a good agreement between NS3 and OpenFOAM and motivates further validation of the freely available OpenFOAM solver for wave force calculations. A successful convergence study for regular wave propagation has been carried out by Paulsen (2013) where

grid-convergence towards the stream function theory solution of Fenton (1988) was demonstrated. The test showed that the OpenFOAM model is capable to model the wave propagation accurately, although, numerical diffusion will induce damping over long distances. With a grid resolution of 15 points over the wave height, the diffusive error for 10 cyclic turn-around of the stream function wave in a periodic domain was about 3% for a wave height of $kH = 0.325$, where $k$ is the wave number. The diffusive error was defined as the root-mean-square of the wave profile (after phase alignment; the phase error was measured separately), normalised with the wave height.

For computation of wave kinematics close to the free surface, discrepancies between OpenFOAM and the reference solution for stream function waves, however, have been observed. Typically the velocities are biased significantly towards the direction of wave propagation, stretching over a handful of grid points around the free surface. OpenFOAM computes the flow not only in water but also in the air above the free surface. In progressive waves, the air flow will generally have opposite horizontal velocity relatively to the water phase. The horizontal velocity thus contains a discontinuous jump in horizontal velocity at the free surface, along with a jump in density associated with the difference between water and air.

As the wave convergence test and further validation tests of the present report shows that OpenFOAM is able to compute the wave motion accurately, it is reasonable to assume that the discrepancies in the near-surface kinematics emerge in the post-processing, where the velocities are likely obtained by division of the momentum variable $\rho u$ by the density variable $\rho$. As both fields contain a sharp gradient at the interface that will both be subject to some numerical smearing, their ratio may not be accurate close to the free surface. It is noted, though, that for the applications in the present project, no extraction of free surface kinematics have been done as all forces are obtained by direct pressure integration.

### 3.2.3 Run-up on vertical cylinders

From the simulations of forces on a vertical cylinder in very steep non-linear waves in the previous section it was seen that a large run-up occurs on the cylinder surface. This may be of interest for at least two reasons: i) the run-up is part of the pressure distribution on the cylinder surface and as such it contributes to the total in-line force, and ii) the run-up may course critical loads on secondary structures if not taken into account when designing and positioning these structures. The simulation of run-up on the vertical surface of a cylinder has previously been investigated by means of the NS3 code as described in Christensen and Hansen (2005) and in Nielsen et al. (2008).

In this section it is investigated how well the OpenFOAM model captures the run-up around a circular cylinder. Experimental data from Kriebel (1992) are used for comparison. These data were also used for the validation of the NS3 code in Christensen & Hansen (2005).

Figure 9 presents a definition sketch of the run-up around the cylinder. The incident wave is magnified as it interacts with the cylinder. Here the run-up, R, is defined as the distance from the mean sea level (MSL) to the position of the free surface on the cylinder at any given time and angular position around the cylinder. The run-up envelope is defined as shown in Figure 9 as the maximum free surface position which has occurred during one wave period around the cylinder. The run-up envelope was experimentally recorded in Kriebel (1992) and will be compared to the numerical results from the OpenFOAM model.

A rectangular model domain has been setup with dimensions corresponding to the experiments reported in Kriebel (1992). A sketch of the layout is shown in Figure 10. The cylinder had a diameter at $D = 0.32$ m and the water depth was $h = 0.45$ m for all experiments. Two cases have been simulated with regular Stokes 2nd order waves given as $kH = 0.215$ ($H = 0.13$ m and $T = 1.95$ s) and $kH = 0.402$ ($H = 0.17$ m and $T = 1.5$ s). At the inlet and outlet boundary

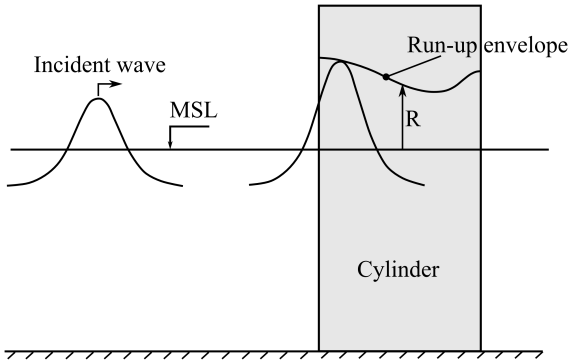


*Figure 9*: Definition sketch of run-up on a circular cylinder. After Kriebel (1992).

a relaxation zone with a length of approximately 1 wave length is used for generating and absorbing the waves respectively.

In the vertical direction uniform grid spacing is applied with a resolution at 0.02 m. In the horizontal direction grid refinement is applied near the cylinder with a minimum resolution at 0.01 m. A total of approximately $700,000$ computational cells are applied.

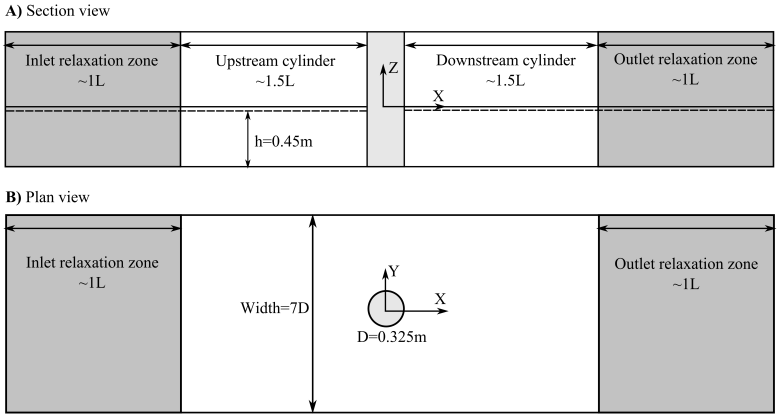


*Figure 10*: Sketch of the numerical model domain.

Figure 10 presents the results of the two cases with kH=0.215 and kH=0.402 respectively. The run-up, R, is normalized with H/2 in order to follow the notation in Kriebel (1992). The results are shown as time stamps of the surface elevation around the cylinder during one wave period. Experiments are shown as the envelope of the surface elevation i.e. the maximum position of the water surface at any angular position around the cylinder.

The simulated run-up is seen to be in good agreement with the experimental data. The maximum run-up is captured both on the leading edge (0deg) and trailing edge (180deg). For $kH = 0.402$ some deviation is seen from 90deg-150deg where the maximum run-up is underestimated. However, the overall impression is that the model is capable of reproducing the measured run-up. Figure 12 and Figure 13 presents an iso-surface contour plot of the free surface around the cylinder at maximum run-up on the leading and trailing edge respectively.

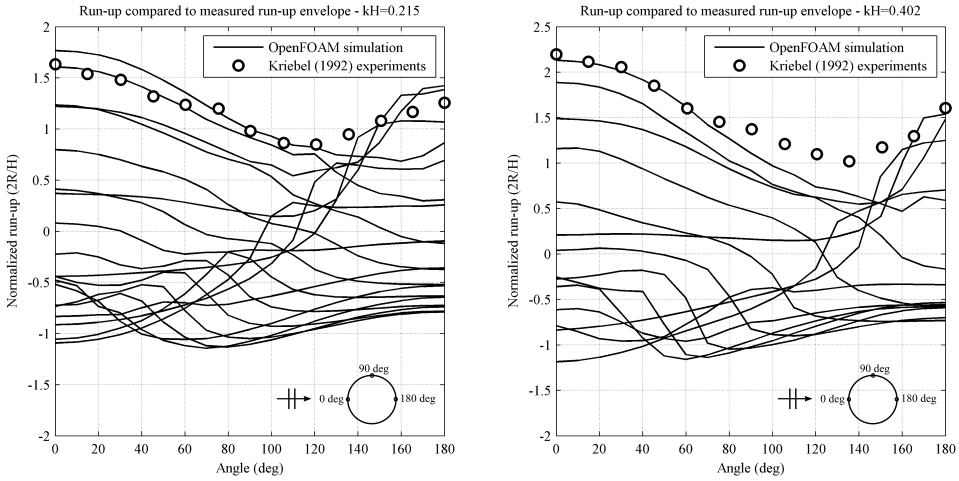


(a) (b)

*Figure 11*: Results of run-up simulations compared to experimental data. Solid lines represent results of the numerical simulation as time stamps of the surface elevation around the cylinder during one wave period. Experimental data are shown as circles representing the envelope of the maximum surface elevation.

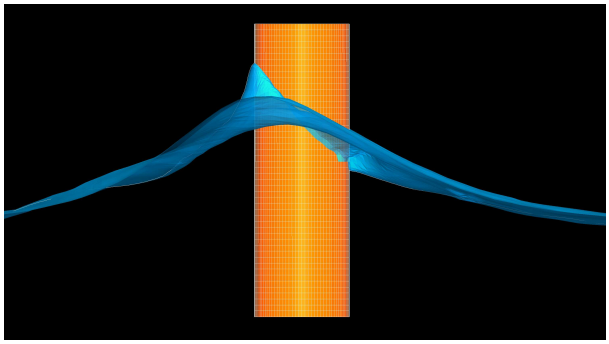

*Figure 12*: Maximum run-up at the leading edge for kH=0.402

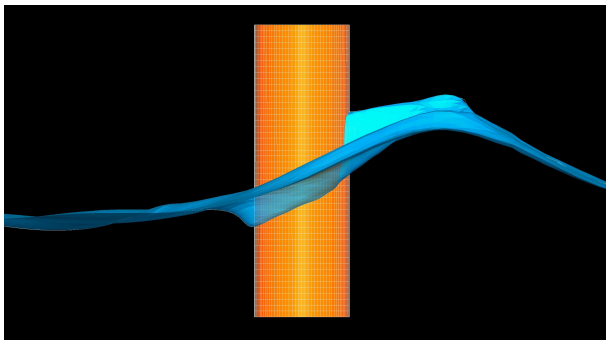

*Figure 13*: Maximum run-up at the trailing edge for kH=0.402

## 3.3 Efficient domain decomposed CFD-model

In this section the domain decomposed solver is briefly discussed. A through discussion of the solver and the governing equations can be found in Paulsen, Bredmose & Bingham (2013). Here, the numerical model is carefully validated and verified against experimental measurements and reference solutions.

The domain decomposed solver consist of an outer flow domain governed by a three-dimensional, fully nonlinear potential flow solver, and an inner domain, which is described by a fully nonlinear Navier-Stokes/VOF solver. A sketch of the numerical domains is shown in figure 14. The outer numerical domain is denoted, $\Omega$. Here the fully nonlinear three-dimensional potential flow problem is solved for the wave motion only. To account for local diffraction effects, wave breaking at the structure and viscous effects a local inner domain, $\Gamma$, is defined, covering a confined volume around the structure. Here, the Navier-Stokes equations are solved in combination with a VOF surface capturing scheme. In designated coupling zones, information from the outer numerical domain, $\Omega$, is interpolated onto the local domain, $\Gamma$, to provide the driving boundary conditions for the inner flow around the structure. In this manner, fully nonlinear boundary conditions are applied for the inner domain, which includes the effect of nonlinear wave transformation and wave-wave interaction. It may be noted that the potential flow solver is orders of magnitudes faster than the Navier-Stokes/VOF solver. Hereby, large numerical domains and/or long time series can be considered. This was otherwise not computationally feasible. Further, due to the higher-order numerical discretization applied in the potential flow solver, water waves can be propagated over long distances with a minimum of numerical diffusion and phase error. This is opposite to the finite volume based Navier-Stokes/VOF solver, which is locally accurate but in general suffers from numerical diffusion.

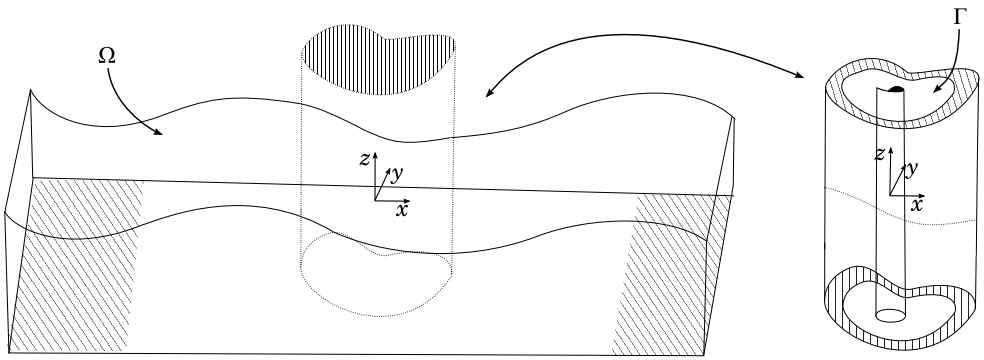


*Figure 14*: Sketch of the numerical domain.

Recently the open-source wave generation utility, waves2Foam, developed by Jacobsen et al. (2012) was released. For the one-way coupling we took advantage of the generic implementation of relaxation zones provided by the waves2Foam utility. An important implication of the applied coupling strategy is that information is only propagating in one direction; from the outer to the inner flow domain. This is based on the assumption that a slender body can not be sensed in the far field.

### 3.3.1 Reflection analysis

As a consequence of the one-way domain decomposition strategy the inner domain has to be truncated at a certain distance, $l$, from the structure. In the case of strong diffraction and reflections, one has to assure that the solution in the vicinity of the structure is independent of the distance $l$. In Paulsen, Bredmose & Bingham (2013) this is carefully investigated and

it was shown that this, in general, do not impose any severe restrictions on the size of the computational domains. To illustrate this, the inline force on a circular cylinder from regular stream function waves with $kR = 0.1$, $kh = 1.0$ and $kA = 0.2$ are considered. In figure 15, the time history of the depth integrated inline force is presented for three different distances between the coupling zone and the cylinder. Due to the restriction of the grid in the vicinity of the cylinder it was not possible to locate the coupling zone closer than $5D \approx L/6$ from the cylinder. As seen from the figure, the force is practically independent of the distance $l$, which indicates that for this set of wave parameters the inline force converges rapidly in terms of the domain length.

It may be noted that during the development and the later use of the domain decomposed solver we have experienced no limitations related to the one-way coupling strategy.

In the following sections, two of the test cases presented in Paulsen, Bredmose & Bingham (2013) are repeated. First, regular waves on a sloping bed are considered. Secondly, multi-directional irregular waves on a sloping bed are considered in section 3.3.3. In Paulsen, Bredmose & Bingham (2013), the domain decomposed solver is also applied for computations of a uni-directional phase-focused wave group and irregular, uni-directional waves.

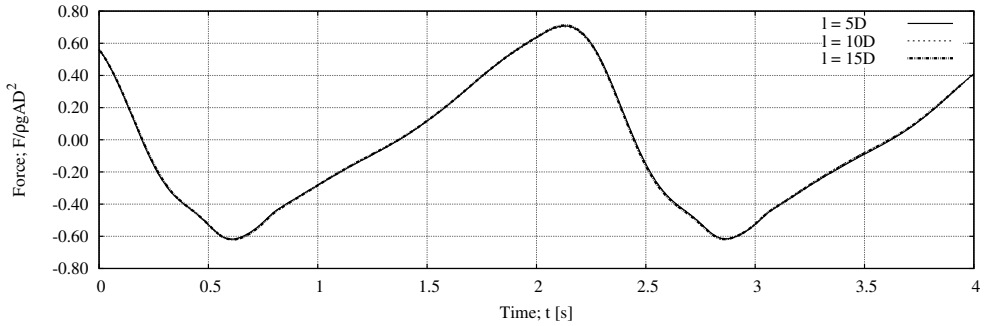


*Figure 15*: Time history of the depth integrated inline force on a circular cylinder for different distances, $l$, from the relaxation zone to the wall.

### 3.3.2 Validation for regular waves

Experimental measurements of regular waves on a sloping bed were numerically reproduced in the time domain. The experiments were carried out as a part of the wave loads project task A and a detailed description of the experiments can be found in Nielsen et al. (2012). A sketch of the numerical domain is shown in figure 16, with relevant dimensions stated in table 4. That the experiments were carried out in scale 1:80. The numerical domain closely follows the experimental setup with the exception of the generation and relaxation zones, indicated by regions of shaded grey in figure 16. For the present study information from six wave gauges were applied, all marked on figure 16, with their $(x,y)$-coordinates listed in table 4.

As uni-directional waves were considered, the potential flow computations were carried out in two spatial dimensions in the $xz$-plane, which significantly reduces the computational cost. Further, as small and short waves with a Keulegan-Carpenter number of $\mathrm{KC} \approx 2$ were considered, the wave force on the cylinder was mainly inertia dominated and a slip condition on the cylinder was applied. It may be noted that the slip condition implies symmetry around the vertical plane of the cylinder, so, without any further assumptions lateral symmetry could by utilized, for which reason only half of the cylinder was considered.

As the paddle signal for the wave maker was unknown the incident wave field was linearly reconstructed as described in Bredmose et al. (2010), Paulsen, Bredmose, Bingham & Schløer

| | Model scale [m] | Full scale[a] [m] | Non-dimension[b][-] |
|---|---|---|---|
| $h_1$ | 0.78 | 62.4 | 1.46 |
| $h_{cyl}$ | 0.51 | 40.8 | 0.96 |
| $h_2$ | 0.42 | 33.6 | 0.79 |
| $D$ | $7.50 \cdot 10^{-2}$ | 6.00 | 0.14 |
| $H$ | $9.59 \cdot 10^{-2}$ | 7.67 | 0.18 |
| $L$ | 3.34 | $2.67 \cdot 10^{2}$ | $2\pi$ |

[a] Scaled by the Froude number.
[b] Non-dimensional by the wave number $k$.

*Table 3*: Dimensional and non-dimensional length scales for experiments and computations of regular waves.

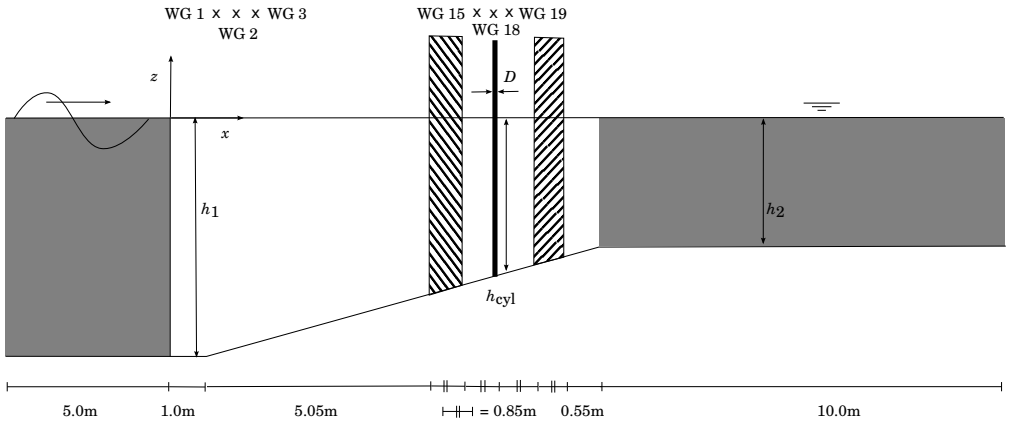


*Figure 16*: Sketch of the numerical domain applied for computations of regular waves impinging on a circular cylinder. In the figure, regions of shaded grey indicates relaxation zones of the potential flow solver, whereas hatched areas indicate the coupling zones between the two solvers.

(2013). Here, information from three wave gauges located at $x \in \{1.00; 1.25; 1.35\}$ m from the wave maker was used. In figure 17 the linearly reconstructed and the measured free surface elevation at the location of wave gauge 1 is shown, and a fair agreement between the two signals is seen.

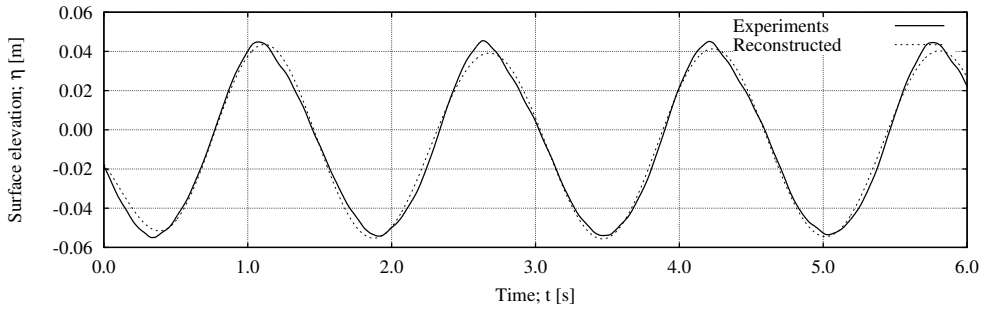


*Figure 17*: Measured and linearly reconstructed free surface elevation at the location of wave gauge 1, located at $x = 1.00$ m.

| Wave gauge | 1 | 2 | 3 | 15 | 18 | 19 |
|---|---|---|---|---|---|---|
| $x$ [m] | 1.00 | 1.25 | 1.35 | 7.50 | 7.75 | 7.95 |
| $y$ [m] | 0.00 | 0.00 | 0.00 | 0.00 | $-1.00/-0.50^a$ | 0.00 |

[a] The physical wave gauge was located outside the numerical domain, so surface elevation at the lateral boundary was applied.

*Table 4*: Location of relevant wave gauges in the experiments of the "Wave Loads" project.

Convergence of the potential flow solver (OceanWave3D) has previously been shown by Engsig-Karup et al. (2009), with respect to analytic stream function waves. For the inner domain, convergence of the numerical model has been shown by Paulsen, Bredmose, Bingham & Jacobsen (2013), where a consistent first-order grid convergence rate towards an analytic solution was demonstrated. For the present study, grid independence was motivated by considering three spatial resolutions, with an average cell length of $dl \in \{1.2; 1,0; 0.8\} \cdot 10^{-2}$ m, which corresponds to a total number of $n \in \{0.71; 1.22; 2.4\} \cdot 10^6$ cells. As seen from figure 18 and 19, both the computed free surface elevation and inline force are practically independent of the spatial resolution.

In figure 18, the computed and measured free surface elevations at the location of wave gauge 15, 18 and 19 are presented, see table 4. In figure 18a, the free surface elevation measured at the location of wave gauge 18 is presented. Here, the flow is measured at the lateral side of the cylinder and is particularly uninfluenced by the presence of the cylinder. In general a good agreement between the measured and the computed free surface elevation is seen, although the magnitude of the free surface elevation at the wave trough is slightly underestimated. The discrepancies are most likely related to the linear reconstruction of the incident wave field, where higher harmonic energy was filtered out as a consequence of the linear assumption.

In figure 18b, the free surface elevation at wave gauge 15, placed 15cm $= 2D$, upstream of the cylinder is presented. Again, the magnitude of the free surface elevation, at the wave trough, is slightly underestimated. However, both the shape and the phase are correctly captured and diffracted waves from the cylinder are observed in both the measured and the computed signals as a small secondary peaks in the wave troughs. The free surface elevation at wave gauge 19, located 20 cm$= 2.67D$ downstream of the cylinder is presented in figure 18c. Here, an excellent agreement between the measurements and the computations is seen. The reason that the best agreement between the measured and the computed free surface elevation is observed downstream of the cylinder is most likely related to the fact that the influence of the cylinder at this location is strong, making minor discrepancies in the incident wave field of less importance.

In figure 19, the inline force on the cylinder is presented as a function of time. A generally good agreement with the experimental measurement is shown, although the computations slightly underestimate the magnitude of the signal at both the maximum and minimum of the inline force. Again, this is attributed to the small discrepancies in the incident wave field. Despite the small underestimation, both the phase and the shape of the force curve are in excellent agreement with the measurements. In figure 19b, a closeup of the peak force is presented. From the plot it may be noted that the difference between the three numerical resolutions is diminishing.

### 3.3.3 Multi-directional irregular waves

Finally, wave loads from three-dimensional irregular waves on a circular cylinder placed on a sloping bed are considered. A sketch of the numerical domain is presented in figure 20. As multi-directional waves were considered the full span-wise direction of the test-basin was resolved by the potential flow solver as indicated in figure 20. For the inner domain, coupling

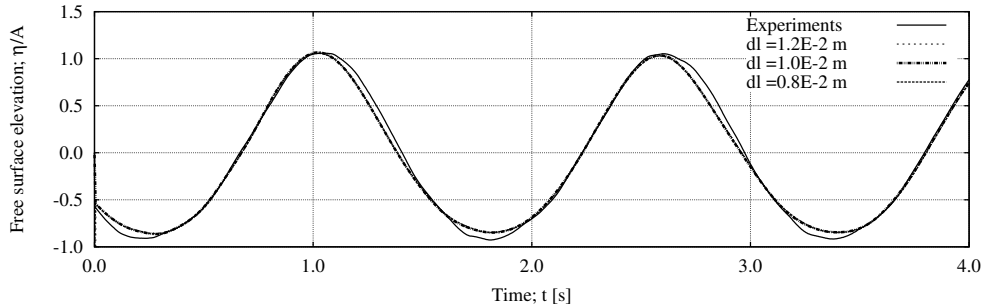


(a) Measured and computed free surface elevation at the location of wave gauge 18, positioned at $\{x;y\} = \{7.75;-1.00\}$ m.

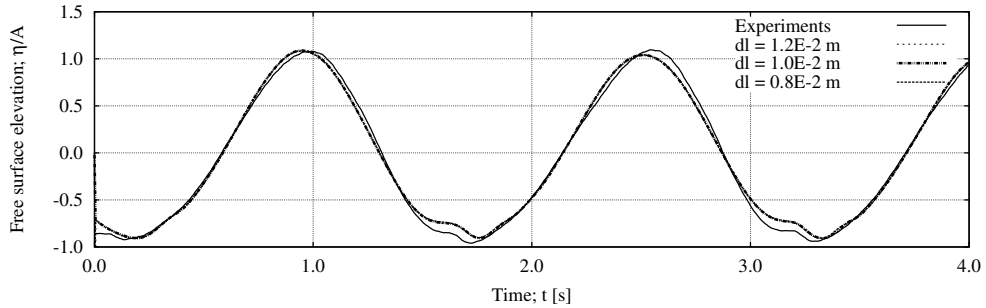


(b) Measured and computed free surface elevation at the location of wave gauge 15, positioned 15 cm$= 2D$ upstream of the cylinder at $\{x;y\} = \{7.50;0.00\}$ m.

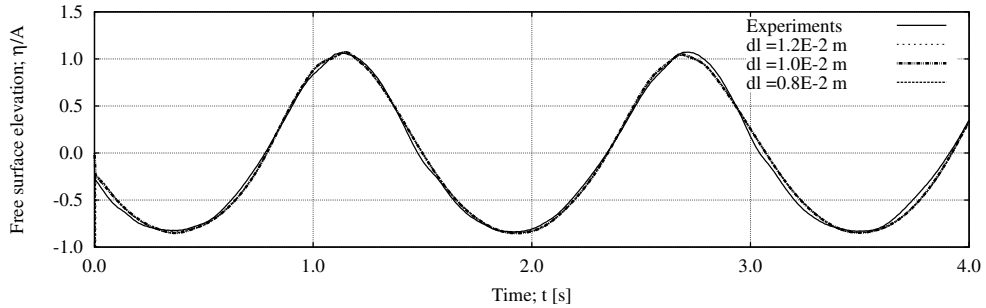


(c) Measured and computed free surface elevation at the location of wave gauge 19, positioned 20 cm$= 2.67D$, downstream of the cylinder at $\{x;y\} = \{7.95;0.00\}$ m.

*Figure 18*: Measured and computed free surface elevation for regular waves.

zones were only placed at boundaries with normal vectors in the principal direction of wave propagation.

For these computations waves were not generated by a relaxation zone, but by a direct flux condition at the inlet boundary. Here the velocities of the wave paddles were imposed as an inhomogeneous flux condition along the inlet boundary of the potential flow solver.

The amplitudes of the incident three-dimensional irregular wave series were given by a JONSWAP spectrum with a full scale significant wave height of $H_s' = 8.3$ m, and a full scale peak period of $T_p' = 12.6$ s. At model scale this corresponds to $H_s = 0.23$ m and $T_p = 2.08$ s. For the present study a non-dimensional spreading factor of $\theta = 0.875$ was used, (see Forristall & Ewans (1998), Nielsen et al. (2012)). In figure 21, a snapshot of the three-dimensional free surface elevation, computed with the potential flow solver is presented for time $t = 15$ s. For the same instance in time the free surface elevation at inner Navier-Stokes/VOF model is presented in figure 22. For both figures the multidirectionallity and complexity of the wave field is seen.

Time series of the free surface elevation up- and downstream of the cylinder are presented in

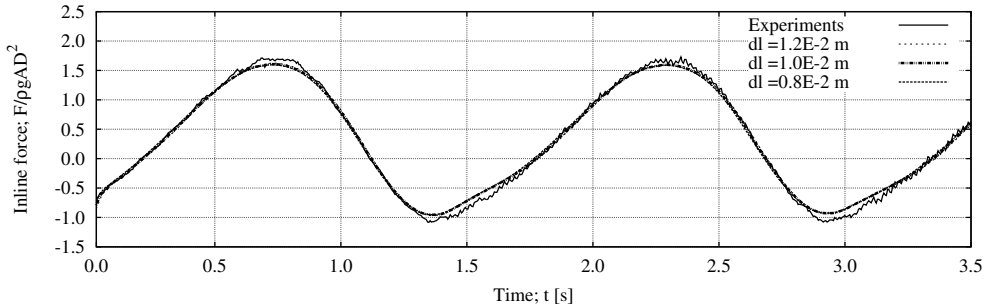


(a) Measured and computed non-dimensional inline force on the cylinder.

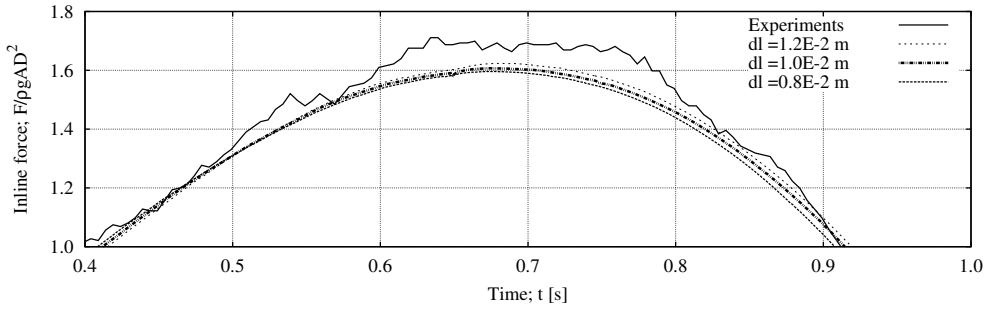


(b) Closeup of the maximum non-dimensional inline force on the cylinder.

*Figure 19*: Inline force on the cylinder for a selected part of the force time history.

figure 23. The location of the wave gauges are stated in table 4. At both locations the free surface elevation was accurately captured by the numerical model in terms of both wave crest and wave trough elevations. For a short time interval between $10-14$ s, small discrepancies between the numerical model and the experimental measurements are seen. The origin of these discrepancies is not known, but it is speculated that they are either a result of spurious second-order waves as discussed in Paulsen, Bredmose & Bingham (2013), or related to absence of active absorption at the wave generation boundary of the potential flow solver.

The horizontal forces on the cylinder, in the $x$- and $y$-direction respectively, are presented in figure 24. As only limited structural vibrations are observed in the measurements the unfiltered force signals are used for the comparison. In general a good agreement between the measured and computed inline force is seen. As for the free surface elevation, minor discrepancies are observed in the time interval $10 < t < 12$. It may be noted that for the largest wave impact the computed inline force is significantly larger than the measured force. It is speculated that this is related to small deflections of the test cylinder due to the non-stiff support of the load cell. These deflection naturally reduces the peak force and may explain the difference in magnitude.

In figure 24b, the force on the cylinder in the $y$-direction is presented. Here, the main features of the wave forcing is captured by the numerical model, but significant discrepancies are also observed. The magnitude of the wave forcing in the $y$-direction is approximately half the magnitude of the wave force in the $x$-direction, why the structural vibrations are more dominant in the force signal and discrepancies appear larger. Structural vibration might explain some of the discrepancies, but not all. Given the good agreement for the inline force and the free surface elevations it is unlikely that the $y$-component of the waves was not correctly captured by the model.

Despite the deviations for the transverse force and the overestimation of the largest inline force an in general a good agreement between the numerical model and the measurements has been shown for both the force and the free surface elevation. Hence the numerical model is able to accurately compute wave impacts from multi-directional, irregular waves on a circular cylinder.

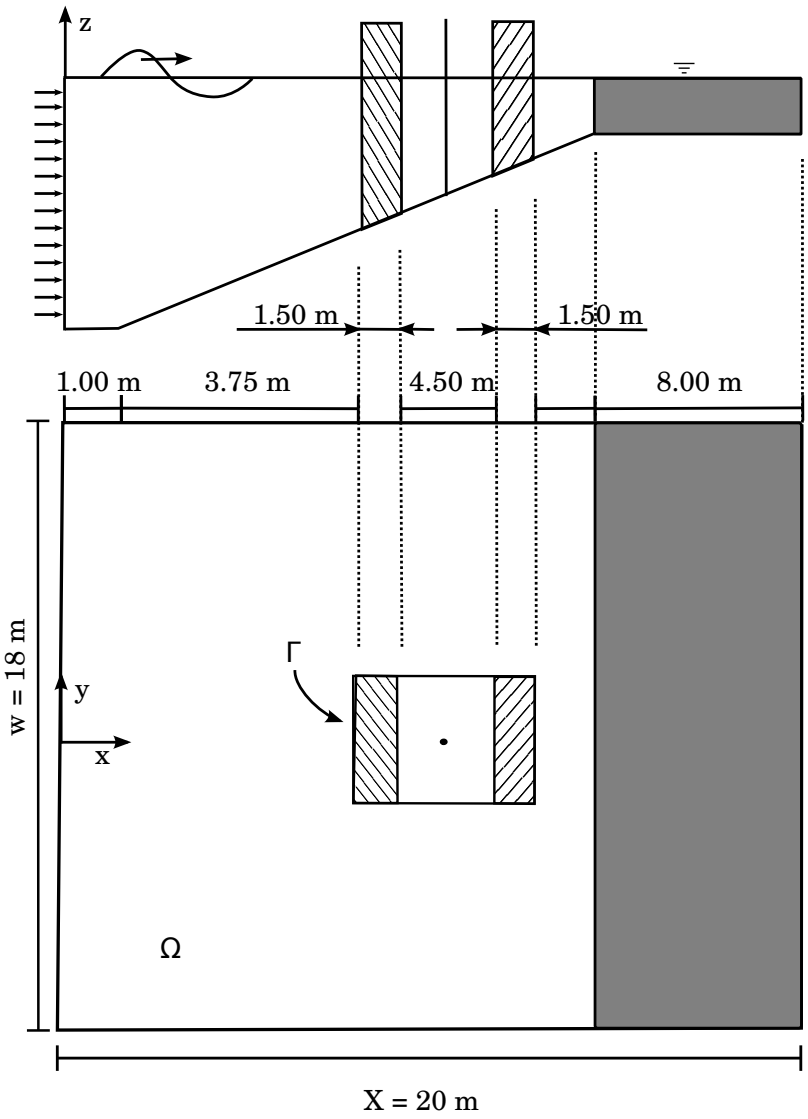


*Figure 20*: Sketch of the numerical domain applied for computations of multi-directional irregular waves. Relxation zone of outer flow solver is indicated by the region of shaded grey and has a total length of 8.0 m. Coupling zones between the two solvers is indicated by cross stripes and both have a length of 1.50 m. The diameter of the cylinder was $D = 16.4 \cdot 10^{-2}$ m.

Therefore, the domain decomposed solver has the potential to describe the forces on monopile foundations of offshore wind turbines from realistic seas.

## 3.4 Higher-harmonic "ringing" loads from steep regular waves

In this section higher-harmonic "ringing" loads from steep regular waves on a flat bed are investigated. In particular, the influence of the relative water depth and the dimensionless wave height is considered. The numerical computations were compared to forces estimated by the force formulation of Rainey (1995).

The chosen wave parameters are typical for the location of monopile foundations for offshore wind turbines and are summarized in table 5. As the computations were carried out with dimensions both dimensional and non-dimensional parameters are listed. An extended study including the effect of the relative cylinder diameter and wave-current interaction is summarized

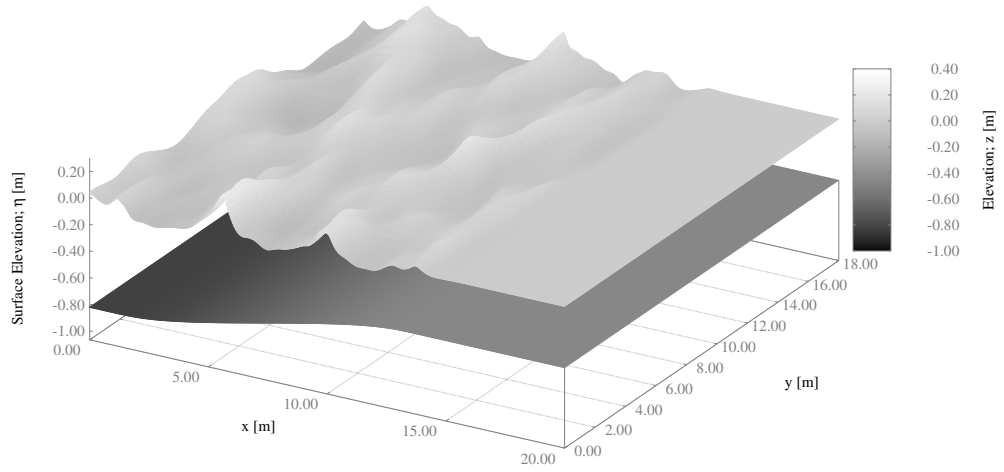


*Figure 21*: Snapshot of the free surface elevation computed by the potential flow solver at time $t = 15$ s.

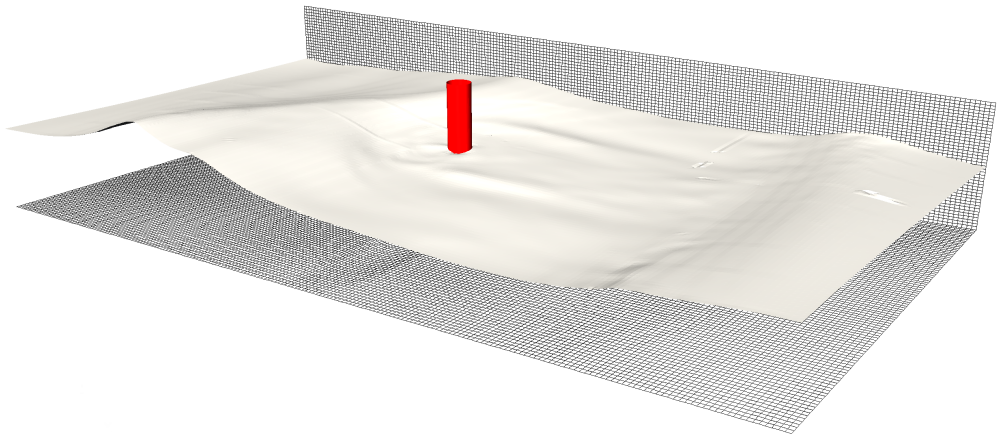

*Figure 22*: Snapshot of the free surface elevation computed by the Navier-Stokes solver at time $t = 15$ s.

in Paulsen, Bredmose, Bingham & Jacobsen (2013) and Paulsen (2013).

The incident waves were all computed according to the fully nonlinear stream function theory of Fenton (1988). The free surface elevation of the undisturbed incident waves are presented in figure 25. The waves are group according to their wave steepness here indicated by the ratio $H/H_{\max}$, where $H$ is the wave height and $H_{\max}$ it the limiting wave height for given wave length and water depth, see Williams (1981), Fenton (1990).

In the figure, a great similarity in the width of the wave crest is observed despite the different water depths and wave steepnesses. The wave crest is here defined as the time between zero-crossings. Further, it may be noted that a direct correlation between the steepness parameter, $\frac{H}{H_{\max}}$, and the temporal curvature of the wave crest, $\eta_{tt}$, is observed.

The depth integrated inline forces for the computations are presented in figure 26, panel a-c. Here the inline force is normalized with the maximum inline force for each computation, $F_{\max}$, and aligned with a zero down crossing at time $t = 0$. For reference, the normalized maximum

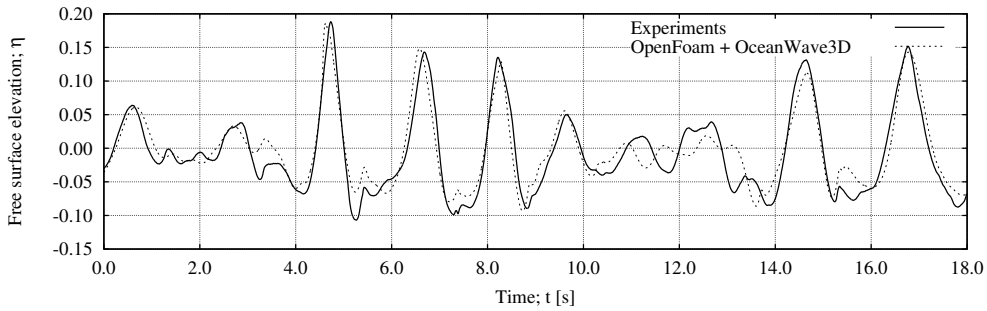


(a) Measured and computed free surface elevation at the location of wave gauge 15, $\{x;y\} = \{7.50;0.00\}$.

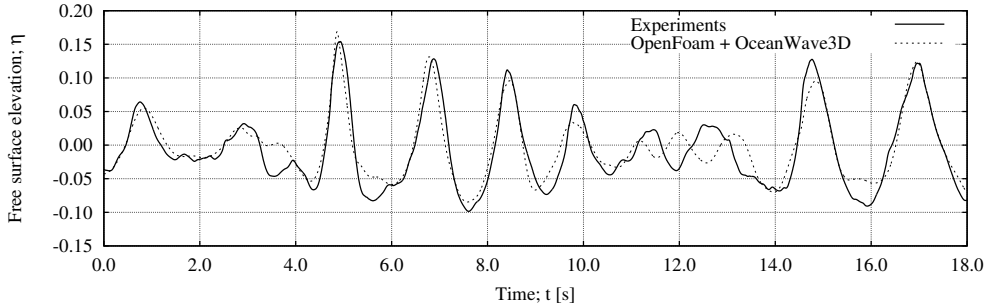


(b) Measured and computed free surface elevation at the location of wave gauge 19, $\{x;y\} = \{7.95;0.00\}$.

*Figure 23*: Measured and computed surface elevation at the location of wave gauge 15 and 19 respectively.

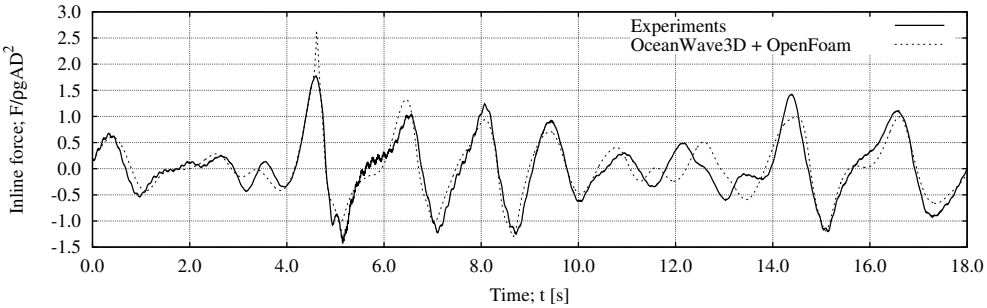


(a) Measured and computed inline force on the cylinder.

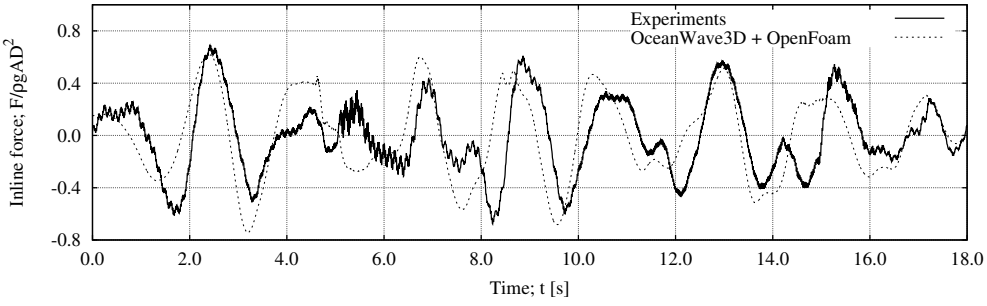


(b) Measured and computed force on the cylinder in the *y*-direction.

*Figure 24*: Measured and computed horizontal forces on the cylinder.

| $H/H_{\max}$ | $h$ | $H$ | $T$ | $L$ | $D$ | $kh$ | $kR\cdot 10$ | $\mathrm{Re}/10^7$ | $KC$ |
|---|---|---|---|---|---|---|---|---|---|
| - | m | m | s | m | m | - | - | - | - |
| | 20 | 8.43 | 13.60 | 188.5 | 6.0 | 0.67 | 1.00 | 1.97 | 11.19 |
| | 25 | 10.02 | 12.70 | 188.5 | 6.0 | 0.83 | 1.00 | 2.06 | 10.90 |
| 0.6 | 30 | 11.35 | 12.10 | 188.5 | 6.0 | 1.00 | 1.00 | 2.13 | 10.75 |
| | 35 | 12.44 | 11.67 | 188.5 | 6.0 | 1.17 | 1.00 | 2.45 | 11.84 |
| | 40 | 13.29 | 11.34 | 188.5 | 6.0 | 1.33 | 1.00 | 2.25 | 10.65 |
| | 20 | 9.83 | 13.38 | 188.5 | 6.0 | 0.67 | 1.00 | 2.47 | 13.74 |
| | 25 | 11.69 | 12.52 | 188.5 | 6.0 | 0.83 | 1.00 | 2.58 | 13.45 |
| 0.7 | 30 | 13.24 | 11.93 | 188.5 | 6.0 | 1.00 | 1.00 | 2.67 | 13.27 |
| | 35 | 14.51 | 11.52 | 188.5 | 6.0 | 1.17 | 1.00 | 2.74 | 13.17 |
| | 40 | 15.51 | 11.22 | 188.5 | 6.0 | 1.33 | 1.00 | 2.81 | 13.12 |
| | 20 | 11.23 | 13.15 | 188.5 | 6.0 | 0.67 | 1.00 | 3.05 | 16.69 |
| | 25 | 13.36 | 12.31 | 188.5 | 6.0 | 0.83 | 1.00 | 3.20 | 16.40 |
| 0.8 | 30 | 15.14 | 11.75 | 188.5 | 6.0 | 1.00 | 1.00 | 3.31 | 16.20 |
| | 35 | 16.58 | 11.35 | 188.5 | 6.0 | 1.17 | 1.00 | 3.40 | 16.08 |
| | 40 | 17.73 | 11.06 | 188.5 | 6.0 | 1.33 | 1.00 | 3.47 | 16.01 |

*Table 5*: Parameters for the incident waves. The dimensionless parameters are defined as: $\mathrm{Re} = \frac{u_{\max} D}{\nu}$ and $KC = u_{\max} T/D$. For all computations $\widetilde{\mathrm{Fr}} = 0$.

inline forces are shown in panel d, as a function of $kh$ and $H/H_{\max}$. For the normalized maximum force a clear dependency on the ratio $H/H_{\max}$ is seen, whereas $F_{\max}$ is seen to be almost independent of the relative water depth, $kh$, for a fixed wave height.

With the chosen alignment and normalization, a remarkable similarity in the temporal development of the force time histories, is seen. Within each panel the force time histories for all water depths almost collapse into a single curve in the time intervals between maximum and minimum loading. These time intervals correspond to the passage of the wave crest, defined as $\eta > 0$, and are indicated in the figure by regions of shaded grey. The indicated time intervals are $t\sqrt{gk} = [-1.03; 0.34]$, $t\sqrt{gk} = [-0.86; 0.40]$ and $t\sqrt{gk} = [-0.69; 0.51]$ for the waves with $H/H_{\max} = 0.6$, $H/H_{\max} = 0.7$ and $H/H_{\max} = 0.8$ respectively. Note that the duration of these time intervals decreases slightly with increasing values of $H/H_{\max}$ and that a relative forward shift in time occurs. The similarity within each of the intervals can be ascribed to the similarity of the incident waves, as documented in figure 25. An important observation from the figure is that the relative water depth is shown to be of little significance in respect to the normalized inline force.

The effect of the wave height on the force time history becomes evident by cross-comparison of the three upper panels in figure 26. Of special interest is the change in loading pattern after the wave crest has passed the cylinder, i.e. the time period after the grey region. For increasing values of $H/H_{\max}$, an additional local force peak is seen to build up close to, and during, the time of minimum loading. This additional loading will be referred to as a secondary load cycle with duration, $T_2$, as indicated by the dashed lines in figure 26b and 26c. The strength of the secondary load cycle can be characterized by the ratio $|F_{\min}|/F_{\max}$, where $F_{\min}$ is the minimum force during the full wave period. It should be noted that this ratio will be affected by other load effects, such as the viscous drag contribution. However, it was found to be a robust and straightforward measure of the strength of the secondary load cycle. Strictly speaking, the ratio $|F_{\min}|/F_{\max}$ is a measure of the skewness in the inline force signal and hence the nonlinearity.

For $H/H_{\max} = 0.6$, the ratio $|F_{\min}|/F_{\max}$ shows a small dependency on the water depth, but is in general close to one, and no distinct secondary load cycles are apparent. For the other computations with $H/H_{\max} \in \{0.7; 0.8\}$, pronounced secondary load cycles are seen and $|F_{\min}|/F_{\max}$

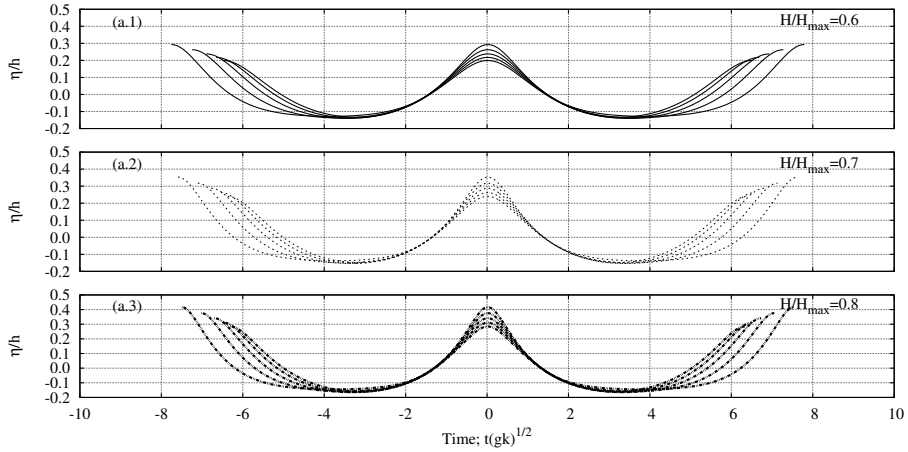


(a) Surface elevation of the incident stream function waves

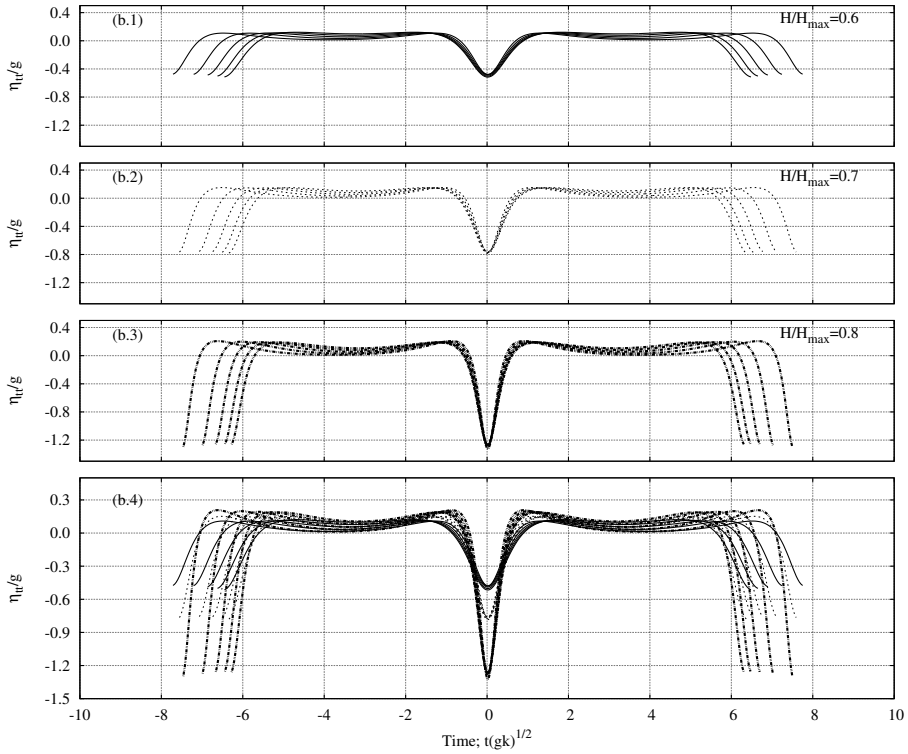


(b) Temporal curvature of the incident stream function waves

*Figure 25*: Curvature and magnitude of the free surface elevation for the waves presented in table 5. Figure (a.1-3) shows the surface elevation with $H/H_{\max} = \{0.6; 0.7; 0.8\}$. Figure (b.1-3) shows the curvature of the waves with $H/H_{\max} = \{0.6; 0.7; 0.8\}$. In figure (b.4) the curvatures of the applied stream function waves are superimposed: ——,$H/H_{\max} = 0.6$; $\cdots$, $H/H_{\max} = 0.7$; —·· ·—, $H/H_{\max} = 0.8$.

drops to 0.7 and 0.6 respectively.

From the figures it is evident that the duration of the secondary load cycle is typically $1/5$ of the wave period or shorter. A similar duration was found by Grue (2002) for steep waves. This implies that the force-contribution from the secondary load cycle will occur within the range of the fifth harmonic in a Fourier decomposition of the inline force and is thus out of reach for the classical ringing theories (Faltinsen et al. (1995), Malenica & Molin (1995)), which predict the third-harmonic forcing. While the secondary load cycle is often directly associated with

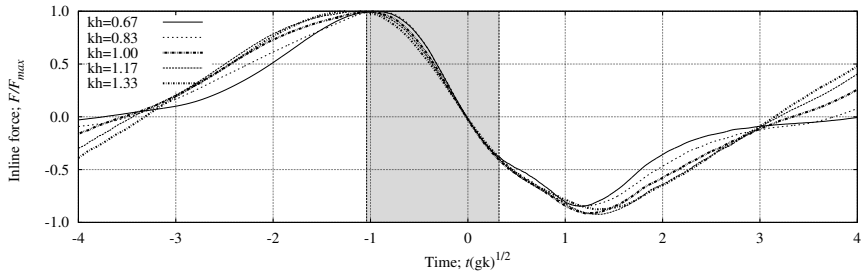


(a) $H/H_{\max} = 0.6$

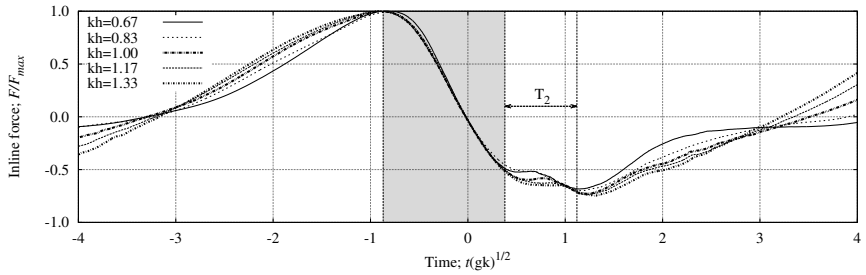


(b) $H/H_{\max} = 0.7$

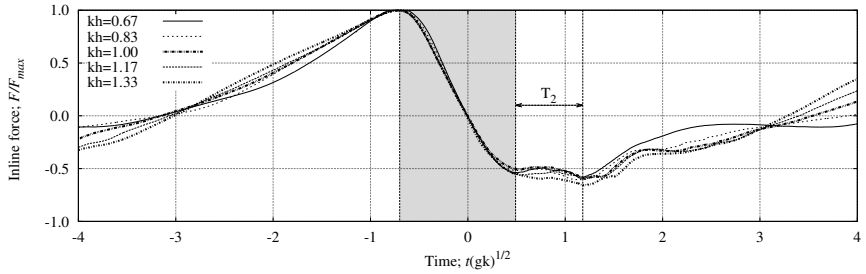


(c) $H/H_{\max} = 0.8$

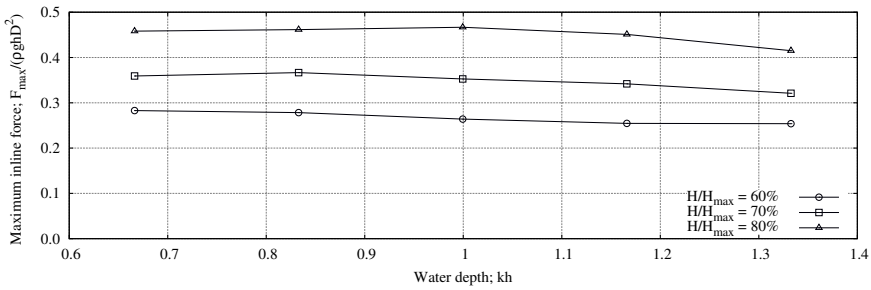


(d) Maximum inline force.

*Figure 26*: Figure a-c: Time histories of the depth integrated inline force grouped by the wave steepness. Notice that all curves have been aligned with a zero down crossing at time $t = 0$. Figure d: Maximum inline force as a function of the water depth and wave steepness.

ringing, the secondary load cycle is here rather seen as an indicator of a highly nonlinear local flow around the cylinder. A thorough discussion of the physics related to the secondary load cycle is presented in Paulsen, Bredmose, Bingham & Jacobsen (2013).

To complete the discussion of the influence of water depth and wave height, the higher-harmonic force components for the computations are considered. The computed higher harmonic forces are compared to results from the extended Morison equation of Rainey (1989) and the third-

order theories of Faltinsen et al. (1995) and Malenica & Molin (1995). In the Morison equation a drag coefficient of $C_D = 0.95$ was estimated from Sumer & Fredsoe (2006); although it was carefully chosen, it should be stressed that it is only an estimate. The results are shown in figure 27, where the magnitude of the $j$th harmonic force was normalized by $\rho g A_1^j D^{(3-j)}$, where $A_1$ is the leading order wave amplitude.

The normalized first harmonic force is seen to decrease with decreasing water depth $kh$. This behaviour is partly due to the decreased wetted area of the cylinder and partly due to the waves being more nonlinear in shallow water. The dependency on the wave height is weak, as all curves collapse into a single curve, independently of $H/H_{\max}$. This confirms the normalization with $A_1$ and shows that the leading order component of the wave force is well predicted by the Morison equation.

For the second-harmonic force an increase in magnitude is seen for decreasing values of $kh$. This is consistent with the fact that waves are more nonlinear in intermediate and shallow water depth, which implies an increase in the higher harmonic forces at reduced depth. For all cases, the computed values of the second harmonic force is smaller than the one predicted by the Morison equation. However, both methods capture the increasing trend and the discrepancies are mainly small.

Similar to the second-harmonic force, the third-harmonic force increases for decreasing water depth. Further, the third-harmonic force shows a clear dependency on the wave height, which indicates that the present computations include more than just the leading-order contribution to the third-harmonic force component.

For $kh < 1.0$ the Morison equation overestimates the magnitude of the third harmonic force, whereas the trend seems to be correctly captured for larger values of $kh$. This discrepancy is attributed to the strong local interactions in the flow around the cylinder, which are not present in the Morison equation.

The deep-water result for the magnitude of the third-harmonic force, given by Faltinsen et al. (1995), is included in the figure as a horizontal dashed (– – –) line. It may be seen that all the computed third-harmonic forces approaches this deep-water limit for increasing values of $kh$. The solution of Malenica & Molin (1995) is indicated by a red $\times$ for $kh = 1.0$. Here an excellent agreement with the computed value for $H/H_{\max} = 60\%$ is apparent. Given that the analytical theory was derived as a weakly nonlinear perturbation solution, the best match with the numerical results should be expected for the smallest of the wave heights considered.

## 3.5 The effect of wave directionality

In this section wave loads from uni- and bi-directional phase-focused waves on a flat bed are numerically investigated. Here, a parameter study of the wave steepness and the influence of wave directionality is presented. The computations are validated in terms of inline forces and free surface elevations obtained experimentally by Zang et al. (2010) and Zang & Taylor (2011).

In section 3.5.1, the numerical domain and the incident waves are presented. Here, the numerical computations are also validated against the experimental measurements. Then, in section 3.5.2 time histories of the free surface elevation in front of the cylinder is discussed. In section 3.5.3, free surface elevations and pressures on the cylinder surface are presented for the main wave impacts. The depth integrated inline force and secondary load cycles are analysed in section 3.5.4.

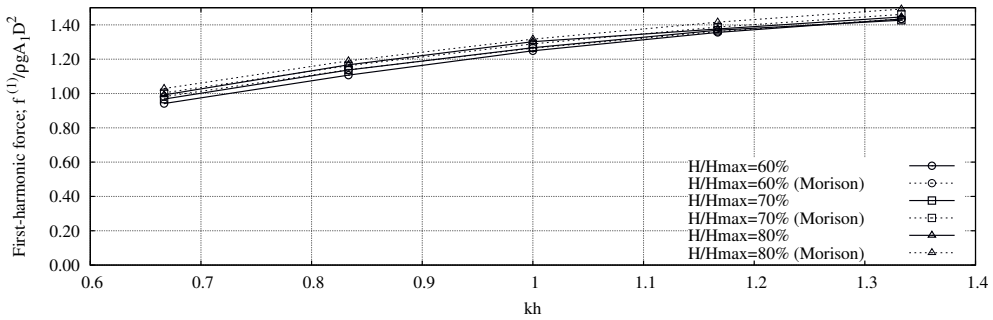


(a) First-harmonic

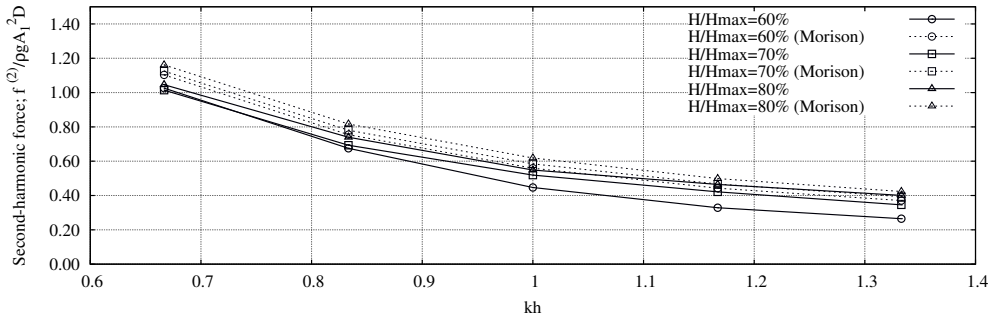


(b) Second-harmonic

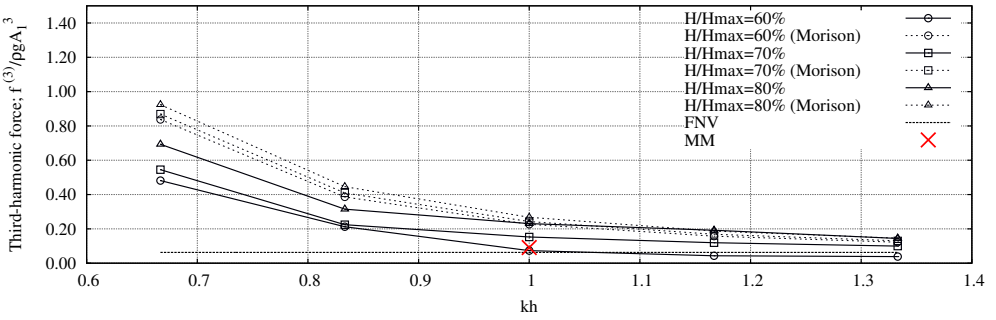


(c) Third-harmonic

*Figure 27*: Non-dimensional magnitudes of higher harmonic forces from the numerical model, the Morison equation and the third order theories of Faltinsen et al. (1995) and Malenica & Molin (1995). For all calculations $kR = 0.1$ and $\widetilde{\mathrm{Fr}} = 0$.

### 3.5.1 Setup and validation

As part of the Hydrolab programme a comprehensive experimental campaign of uni- and bi-directional phase-focused wave groups were carried out at DHI, Denmark. For the uni-directional wave groups, wave loads on a bottom mounted circular cylinder were considered, whereas wave loads on a circular cylinder with a caisson foundation was considered for the bi-directional wave groups. For more information about the test setup and the experiments see Paulsen (2013), Zang & Taylor (2011), Zang et al. (2010), Fitzgerald et al. (2012), Ning et al. (2009). The measurements form this experimental campaign were kindly provided by Jun Zang and Paul Taylor.

For the numerical investigation, the test basin at DHI, Denmark was numerically reproduced by the domain decomposed solver presented in section 3.3. The domain has a total length of 20 m and a width of 18 m. A sketch of the numerical domain is presented in figure 28, where shaded grey indicate the relaxation zone in the potential flow model, whereas hatched areas indicate

the coupling zones between the two numerical domains. As the target paddle signals for the wave maker is known the waves were numerically generated by a flux condition at the inlet boundary of the potential flow solver. This wave generation technique is discussed in Paulsen (2013).

The free surface elevation was considered at three locations; in front of the cylinder, at the lateral side of the cylinder and behind the cylinder. The locations of the three wave gauges are stated in table 6 and indicated in figure 28.

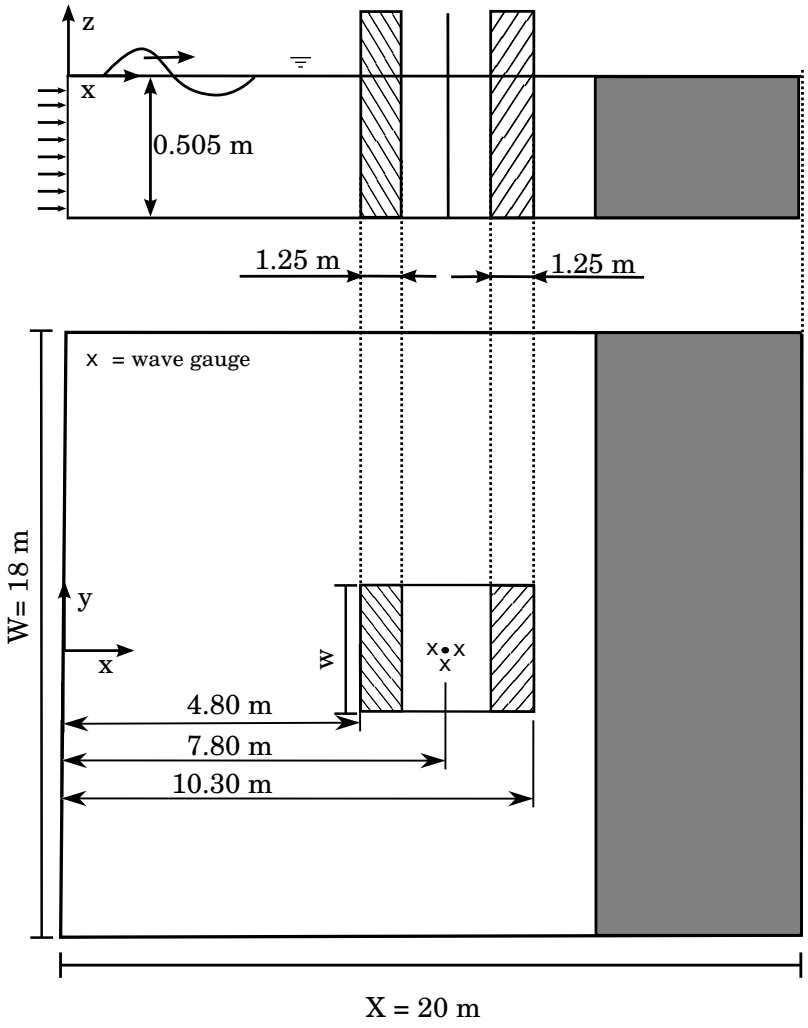


*Figure 28*: Sketch of the numerical domain applied for computations of multi-directionanl phase-focused waves.

| Wave gauge | 1 | 2 | 3 |
|---|---|---|---|
| $x$ [m] | 7.55 | 7.8 | 8.09 |
| $y$ [m] | 9.00 | 8.59 | 9.00 |

*Table 6*: Physical coordinates of the wave gauges used for the investigation of uni- and bi-directional waves.

For the numerical investigation eleven test cases were included, representing six different wave heights and two different wave configurations. The wave heights cover the range from small

linear waves with $k_pA = 0.12$ to steep nonlinear breaking waves with $k_pA = 0.36$, where $k_p$ is the linear wave number based on the peak frequency and $A$ is the linear target wave amplitude at the focus point. The target wave height at the focus point was either created by uni-directional, hence two-dimensional waves, or bi-directional three-dimensional waves. All waves had focus point at $x_0 = 7.8$ m and a peak frequency of $f_p = 0.49$ Hz. A complete list of all cases are presented in table 7. The computations were carried out at a constant water depth of $k_ph = 0.63$, which corresponds to intermediate water depth and is typical for the location of offshore wind turbines. Further, it may be noted that the incident waves were of the "NewWave" type, see Cassidy et al. (2001). The "NewWave" wave group gives the statistically most probable shape of an extreme event, with the limitation of linear wave theory. Here, the free surface elevation is given by the following sum

$$\eta(x',\tau) = \frac{\alpha}{\sigma^2}\sum_{n=1}^{N}\left[S_{\eta\eta}(\omega_n)\mathrm{d}\omega\right]\cos\left(k_n x' - \omega_n\tau\right), \tag{10}$$

where $k_n$ is the wave number of $n'$th component, $\alpha$ is the crest elevation at the focus point, $S_{\eta\eta}(\omega_n)\mathrm{d}\omega$ is the surface elevation spectrum, with standard deviation $\sigma$ and $x' = x - x_0$ is the distance of the focus point relative to the initial position.

The bi-directional waves were created by two wave trains propagating towards the focus point with an angle of $\pm 20$ deg to the principal axis. In figure 29, snapshots of the undisturbed free surface elevation of the bi-directional waves are shown. In the upper panel, figure 29a, the wave group is shown at an early stage and the bi-directionality of the waves is clearly seen. In the lower panel, a fully developed wave group is shown at the time of focusing.

| | $k_pA$ | $f_p/\sqrt{gk_p}$ | $x_0$ [m] | $\angle$ [deg] | Note |
|---|---|---|---|---|---|
| 1 | 0.12 | 0.14 | 7.80 | 0 | Validation |
| 2 | 0.12 | 0.14 | 7.80 | $\pm$ 20 | |
| 3 | 0.18 | 0.14 | 7.80 | 0 | |
| 4 | 0.18 | 0.14 | 7.80 | $\pm$ 20 | Validation |
| 5 | 0.24 | 0.14 | 7.80 | 0 | |
| 6 | 0.24 | 0.14 | 7.80 | $\pm$ 20 | |
| 7 | 0.30 | 0.14 | 7.80 | 0 | |
| 8 | 0.30 | 0.14 | 7.80 | $\pm$ 20 | |
| 9 | 0.33 | 0.14 | 7.80 | 0 | |
| 10 | 0.33 | 0.14 | 7.80 | $\pm$ 20 | |
| 11 | 0.36 | 0.14 | 7.80 | $\pm$ 20 | |

*Table 7*: Wave properties for multi-directional phase-focused waves.

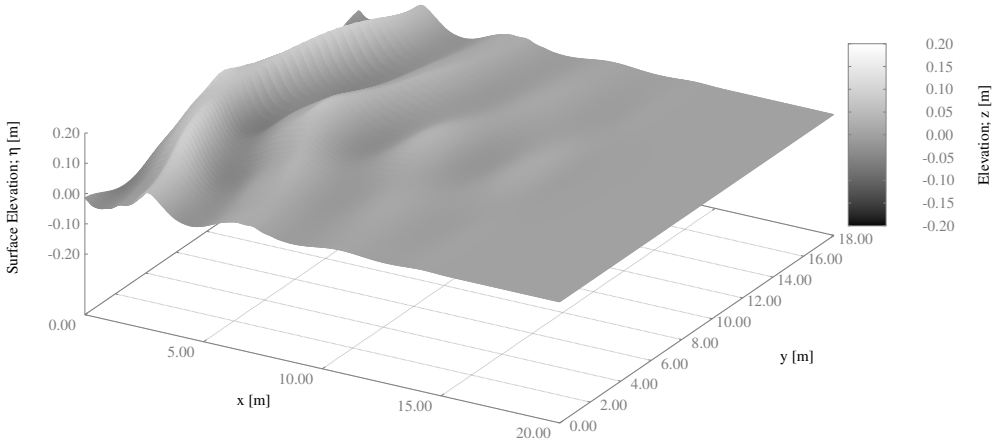


(a) Free surface elevation of a bi-directional phase-focused wave group; $k_pA = 0.24$, $t = 15.8$ s

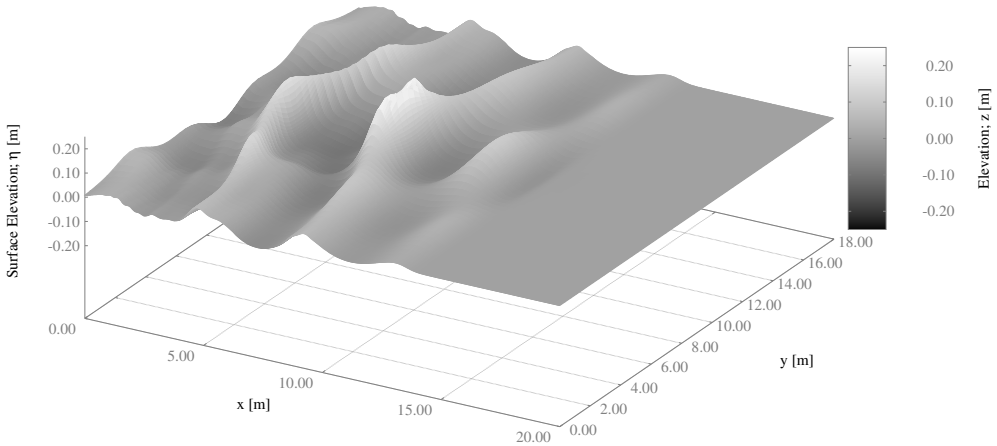


(b) Free surface elevation of a bi-directional phase-focused wave group; $k_pA = 0.36$, $t = 38.4$ s

*Figure 29*: Free surface elevations of the undisturbed bi-directional waves. Upper panel: Initial wave trains. Lower panel: Wave focusing.

### 3.5.2 Time histories of the free surface elevation

In figure 30, the time histories of the free surface elevation at the lateral side of the cylinder are presented for the uni- and the bi-directional wave groups respectively. In the upper panel, the free surface elevation from the uni-directional wave groups are presented, whereas the free surface elevation from the bi-directional wave groups are presented in the lower panel. For the uni-directional waves, a distinct phase difference between the largest waves in the wave group is clearly observed. This is caused by nonlinear dispersion. A clear misalignment between the wave signals is observed for $42 < t < 44$. This phenomenon is most likely related to second-order free spurious waves from the linear wave generation. These small unbound waves with frequency $f = 2f_p$, travel slower than the main wave group and hence arrive later at the cylinder.

For the bi-directional wave groups, presented in figure 30b, both the effect of amplitude dispersion and the second order free spurious waves are observed. However, as the incident waves were less steep prior to the focus point, nonlinearity is less important and both effects are less pronounced.

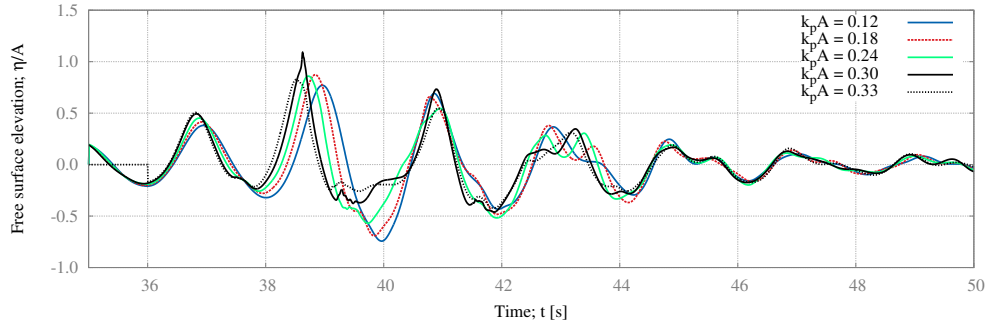


(a) Unidirectional phase-focused waves.

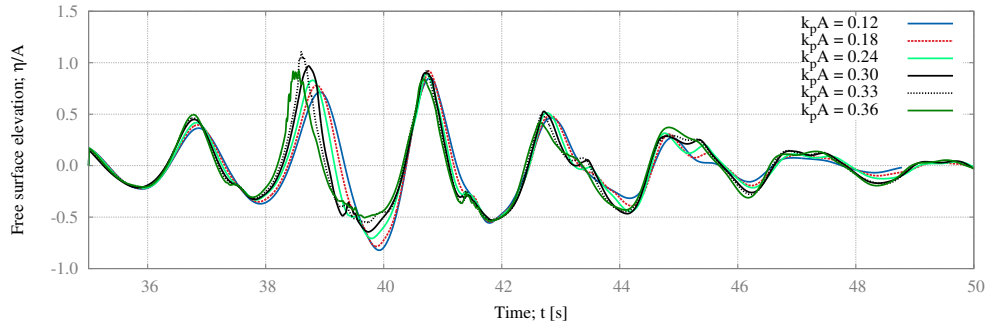


(b) Bi-directional phase-focused waves.

*Figure 30*: Time histories of the free surface elevation at the location of wave gauge 2, located at $\{x,y\} = \{7.80, 8.59\}$ m.

For both the uni- and the bi-directional waves it may be noted that a rise in the crest and trough elevations is seen for increasing wave steepness until $k_pA \geq 0.33$. Beyond this steepness wave breaking starts to decrease the wave height.

In figure 31, the maximum crest elevation of the uni- and the bi-directional wave groups are presented as a function of the wave steepness. The crest elevations are here considered at the location of wave gauge 1. First it may be noted that $k_p$ is the linear wave number and hence constant for all the waves presented here. Further, the crest elevation should, in a linear sense, be proportional to the wave amplitude $A$. So, the observed increase in the non-dimensional crest elevations is entirely a consequence of nonlinearity. Here, two nonlinear effects are expected to be significant: First, the free surface elevation is considered upstream of the focus point, and

hence the crest elevation is not at its maximum. As the wave amplitude increases the focus point moves closer to the wave maker due to amplitude dispersion. Hereby, the observed crest elevation, at the location of wave gauge 1, increases. Secondly, the wave set-up observed in figure 30 is also influencing the maximum crest elevation in a nonlinear way. Surprisingly, the increasing trend of the maximum crest elevations is seen to be linear for both the uni- and the bi-directional wave groups. Naturally, this trend breaks down as wave breaking starts to occur for $k_pA > 0.30$.

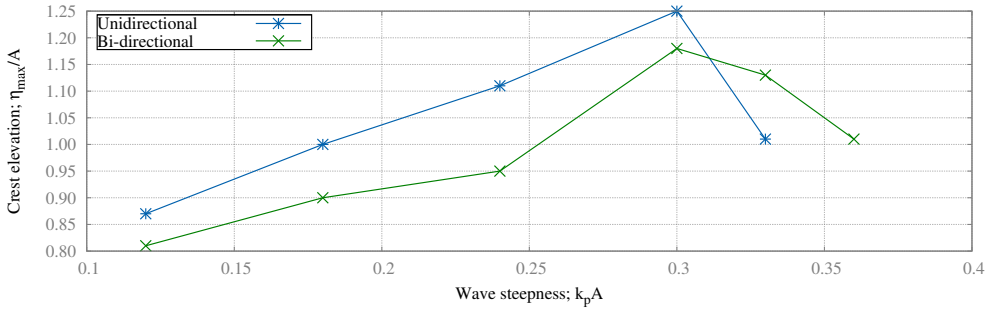


*Figure 31*: Maximum crest elevation in front of the cylinder at the location of wave gauge 1.

### 3.5.3 Selected snapshots of the wave impacts

Snapshots of the free surface elevation and the dynamic pressures, $p^*$, on the cylinder surface are presented for $k_pA = \{0.30; 0.33\}$ in figure 32 and 33. The dynamic pressure is defined as the total pressure with the following linear hydrostatic correction

$$p^* = p + \rho g z \tag{11}$$

here $\rho$ is the instantaneous density of water and air respectively. This is a linearly consistent correction for $z \leq 0$ but pressures in the interval $z \in [0; \eta]$ will be enlarged.

In figure 32, the impacts from the wave groups with a steepness of $k_pA = 0.30$ are presented. For the uni-directional wave group a violent wave impact from a near breaking wave is observed. It may be noted how the free surface elevation at the wave crest is almost vertical at the time of the wave impact. Here, a significant wave run-up is observed at the upstream side of the cylinder. At the downstream side of the cylinder a hole is created due to the blockage of the cylinder. This hole is about to be filled by the diffracted wave propagating around the cylinder. As discussed in Paulsen, Bredmose, Bingham & Jacobsen (2013), this might generate a low pressure at the downstream side, which is then be observed as a secondary load cycle. Due to the steepness of the wave, a slamming like impact is observed. This introduces a high pressure zone beneath the free surface at the time of the wave impact.

For the bi-directional wave impact, shown in figure 32c, the bi-directionality of the incident waves is clearly seen. The incident wave trains have crossed at the center of the domain and the angled wave font is seen in the foreground of the figure. In front of the cylinder, the two waves have interacted and a steep wave front moving perpendicular to the cylinder is observed. Again, a significant wave run-up at the upstream side of the cylinder is seen, with a distinct hole at the downstream side due to the blockage effect.

In figure 33, snapshots of the free surface and the dynamic pressures on the cylinder from the very steep wave groups with $k_pA = 0.33$ are presented. The wave impact form the uni-directional waves seems less violent than the one presented in figure 32a for $k_pA = 0.30$. This is related to the wave breaking filter applied in the outer potential flow model, see discussion in Paulsen (2013).

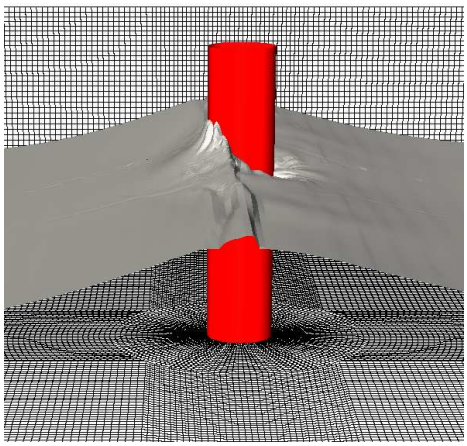

(a) Unidirectional wave impact: Free surface

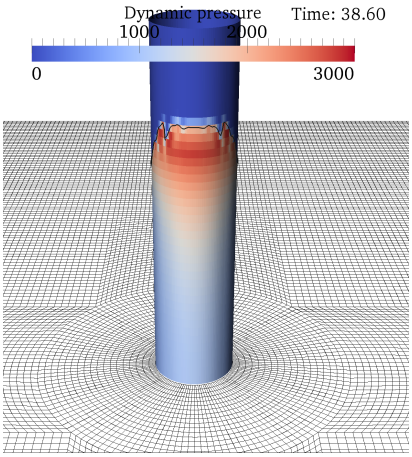


(b) Unidirectional wave impact: Dynamic pressure

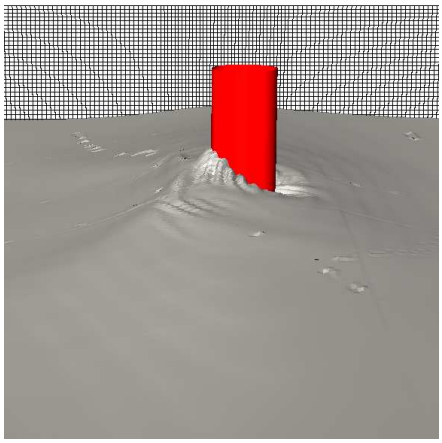

(c) Bi-directional wave impact: Free surface

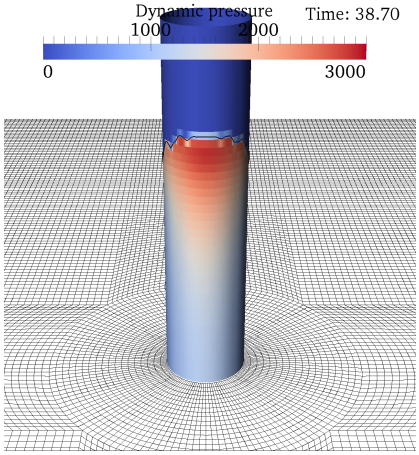


(d) Bi-directional wave impact: Dynamic pressure

*Figure 32*: Snapshots of the free surface elevation during the impact of a uni- or bi-directional wave group respectively. $k_pA = 0.30$

For the bi-directional wave group a slamming type wave impact is seen, with a steep almost vertical wave front hitting the cylinder. The wave is only breaking at the center of the domain, where the two wave trains are focusing. In the free surface region a high local pressure is seen at the center of the cylinder and a significant wave run-up is observed at the upstream side. This type of wave impacts is a clear design driver for offshore structures as foundations for offshore wind turbines. The high local pressure in the free surface zone gives a high bending moment at the mud line and further, due to the impulsive type loading, the structure is exposed to a broad-banded excitation force which might introduce structural resonance. It is of particular concern that this type of wave impacts are expected during violent storms where the turbine is in parked position and the aerodynamic damping is low. It is important to notice that this wave impact is more violent than any of the uni-directional ones. So, in the present example applying uni-directional waves for design calculations is non-conservative in terms of peak loads and bending moments.

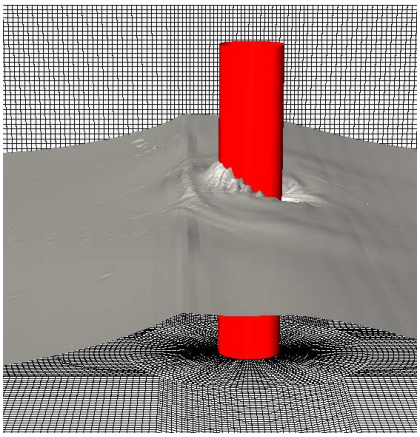

(a) Unidirectional wave impact: Free surface

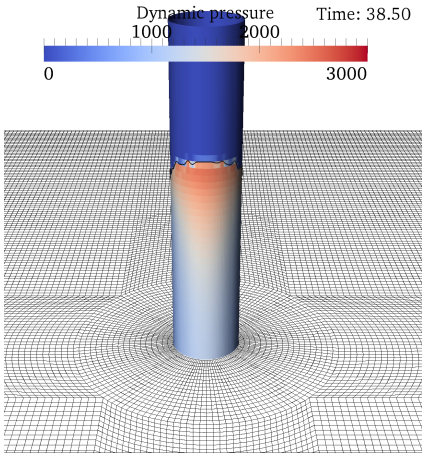


(b) Unidirectional wave impact: Dynamic pressure

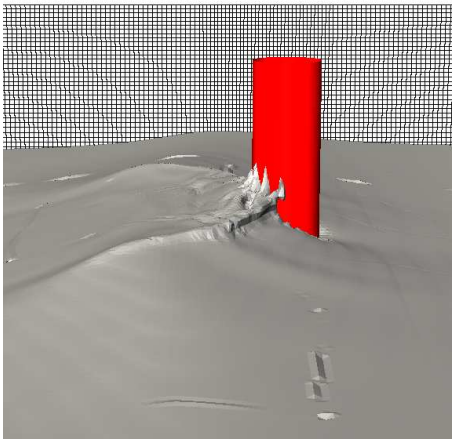

(c) Bi-directional wave impact: Free surface

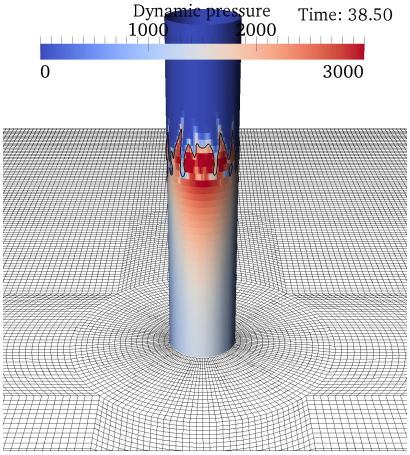


(d) Bi-directional wave impact: Dynamic pressure

*Figure 33*: Snapshots of the free surface elevation during the impact of a uni- or bi-directional wave group respectively. $k_pA = 0.33$

### 3.5.4 Inline forces

In figure 34, the time histories of the uni- and the bi-directional wave groups are presented. In the upper panel the inline force from the uni-directional waves are shown, whereas the force from the bi-directional ones are presented in the lower panel. It may be noted that all forces in the $y-$direction were zero due to symmetry of the incident waves.

In general, the force time histories follow many of the same trends as were observed in the time histories of the free surface elevation presented in figure 3.5.2.

In figure 35, the peak forces are presented as a function of the wave steepness for the uni- and bi-directional wave groups respectively. Here the peak forces are normalized by $\rho gAD^2$, where it may be noted that $\rho gD^2$ is constant, so the normalization is a linear function of $A$. For the uni-directional waves a small almost linear increase in the non-dimensional peak forces is seen for $k_pA \leq 0.30$. This trend is destroyed for $k_pA = 0.33$ due to early onset of wave breaking. For the bi-directional waves an almost exponential increase in the peak forces is seen. Most significant is the increase from $k_pA = 0.30$ to $k_pA = 0.33$, where the non-dimensional peak force is seen to increase by as much as 25%. For the steepest bi-directional wave with $k_pA = 0.36$ early wave

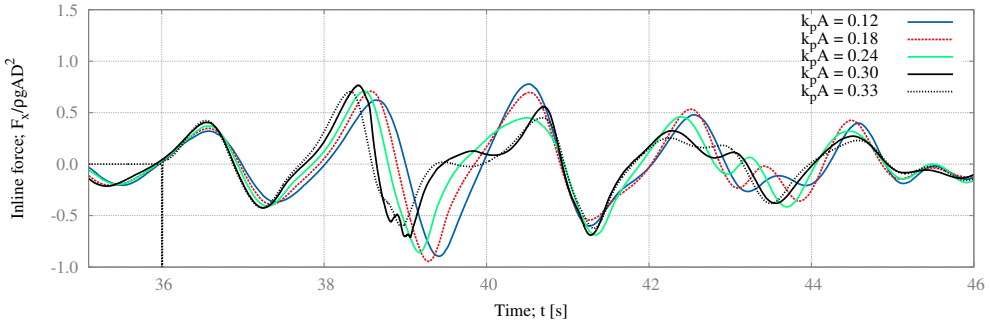


(a) Force time history of the inline force from uni-directional phase-focused waves

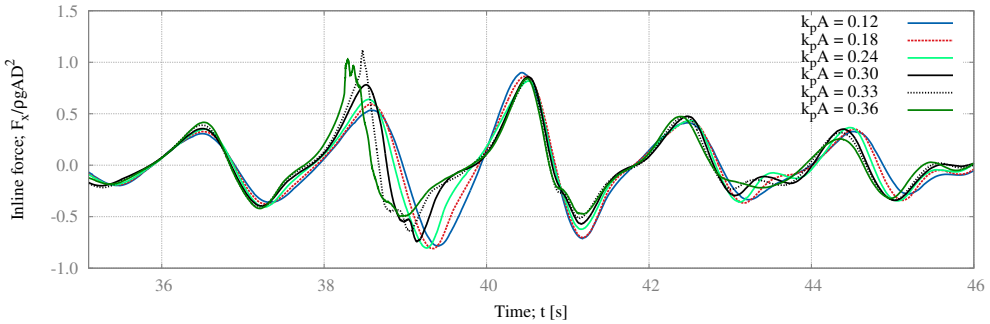


(b) Force time history of the inline force from bi-directional phase-focused waves

*Figure 34*: Force time history of the inline force from uni- and bi-directional phase-focused waves

breaking becomes an issue and the peak force is slightly reduced. The substantial increase in the peak force, observed when the wave steepness is increased from $k_pA = 0.30$ to $k_pA = 0.33$, is rather related to the change in impact type than the increased wave height. For the bi-directional wave with $k_pA = 0.30$ a steep but non-breaking wave is hitting the cylinder, whereas the wave group with $k_pA = 0.33$ gives a slamming type impact from a breaking wave.

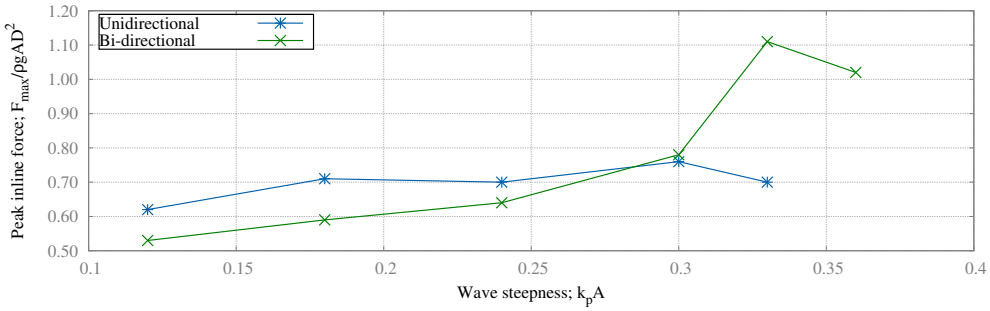


*Figure 35*: Peak inline forces at the cylinder for uni- and bi-directional wave groups respectively.

When comparing the peak forces, presented in figure 35, with the peak crest elevations, presented in figure 31, two different trends are observed. Most surprising is the observation that the crest elevation for the uni-directional wave with $k_pA = 0.30$ is larger than the bi-directional one, whereas the peak force from the bi-directional wave is slightly larger. This is particularly interesting as the wave impact form the uni-directional wave seems more violent than the impact from the bi-directional wave group, see figure 32. This observation indicates that wave directionality may increase the ultimate wave loads even for non-extreme cases. To investigate this

further, the depth integrated pressures on the wetted part of the cylinder surfaces are presented in figure 36. As seen from the figure, the spatial distribution of the depth integrated pressures is similar for the uni- and bi-directional wave impacts, though the magnitude is slightly larger for the bi-directional one. This indicates that a substantial part of the force comes from beneath the free surface region and that the bi-directionality increases the force.

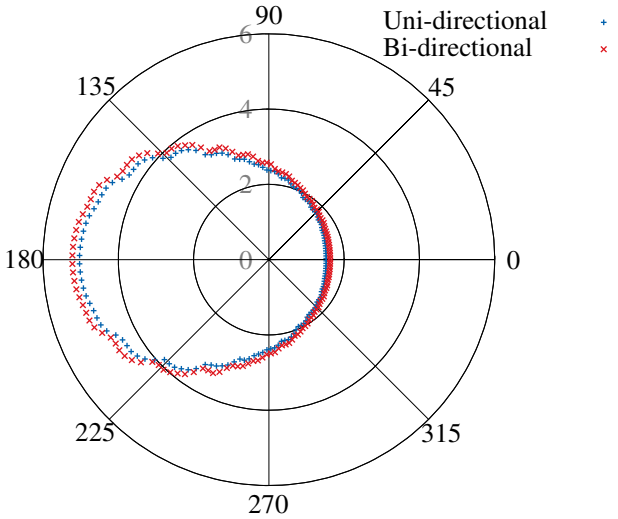


*Figure 36*: Depth integrated dynamic pressures on the cylinder for the uni- and bi-directional wave groups with $k_pA = 0.30$. The time corresponds to the time of peak loading. The unit of the radial axis is Newton.

## 3.6 Summary

A one-way domain decomposition strategy between a fully nonlinear potential flow solver and a fully nonlinear Navier-Stokes/VOF solver has been formulated. The one-way coupling strategy was shown to be a promising alternative to the complicated and inefficient two-way coupling.

The domain decomposed solver has been carefully validated against experimental measurements and in this report two test cases are presented. First, regular waves on a sloping bed were considered. Here, both the free surface elevation and the inline force were seen to be in agreement with the experimental measurements. Secondly, multi-directional irregular waves on a sloping bed were considered. For this test case the entire shallow water basin at DHI, Denmark was resolved by the potential flow solver and a confined volume around the test cylinder was described by the Navier-Stokes/VOF solver. Despite the large computational domain and the complicated physics, which includes both wave breaking and nonlinear wave-wave interaction, a good agreement between the numerical computations and the experimental measurements was seen. For further validation see Paulsen (2013)

Higher-harmonic “ringing” wave loads from steep regular waves were investigated. Special attention was paid to the temporal development of the normalized inline force. For the chosen set of wave parameters the wave steepness was shown to be a strong governing parameter, whereas the normalized inline force was shown to be independent of the water depth.

The magnitude of the first three harmonic forces were computed and compared against the Morison equation and higher-order wave load theories. For the first and second harmonic forces a fair agreement between the computations and the Morison equation was seen. The computed third-harmonic forces were shown to be in agreement with the third order solutions of Faltinsen et al. (1995) and Malenica & Molin (1995), whereas the Morison equation was shown to

significantly overestimate the magnitude of the third harmonic force for $kh < 1$.

The investigation of strongly nonlinear wave loads was extended to include uni- and bi-directional waves. In time histories of the free surface elevation nonlinear effects from amplitude dispersion and spurious second order waves from the linear wave generation were observed. Further, a linear increase in the non-dimensional crest elevations was shown as a function of the wave steepness for non-breaking waves.

For the steep phase-focused wave groups, slamming type impacts were observed, with a high local pressure in the free surface region. These high local pressures have the potential to introduce local buckling in the steel monopile towers and further gives rise to a high bending moment at the mud line. This type of wave impacts are clear design drivers for foundations of offshore wind turbines and should be of major concern.

For the non-dimensional peak force a mild linear increase was shown for the uni-directional wave groups, whereas an almost exponential increase was observed for the bi-direction wave groups. This may partly be related to the impact types, but indicates that directionality may be important for ultimate wave loads. Due to the reduced wave hight of the bi-directional wave trains prior to the focus point, offshore wave breaking was observed for a greater steepness than for the uni-directional waves. Hence, a larger and more violent wave impact could be created at the focus point.

For the steepest non-breaking waves, secondary load cycles were observed and they were, again, associated with a downstream circulation zone caused by local flow interaction. This confirms the observations made for regular waves in Paulsen, Bredmose, Bingham & Jacobsen (2013) and Paulsen (2013). Further, it was shown that wave breaking reduces local diffraction around the cylinder and hence the mechanisms driving the secondary load cycle.

## 3.7 Suggestions for further work

The domain decomposed solver has great potential for further application. It can be used directly to benchmark simpler methods for computation of wave loads. Further, the numerical method itself can also be developed further. Suggestions for further work, that will be of value for cost-reduction of design is

- Numerical quantification of 3D load effects for storm waves with the purpose to establish reliable statistics for the consequence of wave directionality for the extreme wave forces
- Incorporation of the viscous boundary layer in the computations and assessment of the associated load effect
- Further validation of breaking wave loads. This would involve detailed comparison to measured pressure fields
- A detailed assesment of higher-harmonic loads and comparison/re-development to the load theories of Faltinsen et al. (1995) and Rainey (1995)
- Assessment of the structural response to CFD-based loads from steep and extreme waves

# 4 Task C(1): Effect of wave nonlinearity for monopile wind turbines

**Signe Schløer (DTU Wind Energy)**
with contributions from Henrik Bredmose, Robert Mikkelsen, Stig Øye, Harry Bingham, Bo Terp Paulsen and Torben Juul Larsen

## 4.1 Introduction

The structural response of offshore wind turbines is induced from the combined loads of waves and wind. A reliable modelling of the structural lifetime therefore requires a coupled dynamic model of the foundation and wind turbine that takes both load contributions into account. Task C(1) concerned the coupling of fully nonlinear wave loads with the FLEX5 aeroelastic model for determination of structural response and fatigue loads for a monopile wind turbine exposed to fully nonlinear waves.

The NREL 5MW reference wind turbine, Jonkman et al. (2009), was setup in Flex5. The implementation was validated against results of the Offshore Code Comparison Collaboration (OC3) for IEA Task 23 Offshore Wind Technology and Deployment, Jonkman & Musial (2010).

Next, the impact of nonlinear wave forcing was investigated and compared against the impact from linear wave forcing. The wave kinematics were calculated by the potential flow model OceanWave3D, Engsig-Karup et al. (2009). The wave forces were based on Morison's equation with the extensions of Rainey (1995). The analyses were both based on static and dynamic calculations. Based on the dynamic calculations, fatigue analyses were also conducted and the effect from nonlinear wave forcing on the fatigue life of the foundation and wind turbine tower was investigated.

Subsequently the wave forces based on OceanWave3D and Morison's equation were compared against more detailed wave loads based on CFD-calculations. The analysis was both based on static calculation and dynamic calculations in Flex5. The dynamic response due to the more detailed wave loads was analysed and compared against the dynamic response due to wave forces based on Morison's equation, which most often is used in today's design of offshore wind turbines.

Finally, dynamic calculations were analysed where the misalignment between the wind and waves was included. In situations of misaligned wind and waves, the wave loads may dominate due to the smaller aerodynamic damping in the wave direction and the nonlinear wave effects therefore be more important. In such situations other types of damping are important. The magnitude of the hydrodynamic radiation damping on a monopile was therefore also calculated. Also a new soil model was implemented into Flex5 to get a better description of the soil's interaction with the pile displacement and of the soil damping.

### 4.1.1 Main achievements

- Application of fully nonlinear wave loads in the aero-elastic code Flex5
- Detailed investigation of the effect of wave nonlinearity for static hydrodynamic loads for five selected wind-wave climates
- Detailed investigation of effect from wave nonlinearity on dynamic response and lifetime fatigue loads

- Application of CFD-based wave loads in aero-elastic computations and comparison to Morison-based wave loads
- Assessment of response-effects from fully nonlinear directionally spread waves
- Investigation of nonlinear wave effects for misaligned wind-wave conditions
- Determination of hydrodynamic radiation damping for the true deflection shapes of the monopile
- Incorporation of a soil model with frictional damping effects

The work is reported in one journal paper (Schløer et al. 2014), three conference papers (Schløer et al. 2011, 2012, Bredmose et al. 2012) and in the PhD-thesis of Schløer (2013). Here a summary of the most important results is given.

In the following, the typical response types to wave loads are defined. Next, an overview of the results for validation of the wind turbine setup in Flex5 is given (section 4.3), followed by the study of nonlinear wave forcing of the monopile wind turbine (section 4.4). The investigation of life time fatigue damage from nonlinear waves is described in section 4.5 followed by the study of CFD forcing (section 4.6). Section 4.7 provides a description of the wind-wave misaligment study, the hydrodynamic radiation damping and the incorporation of the new soil model into Flex5. The chapter concludes with a summary and suggestions for further work.

## 4.2 Structural response to wave loads

The structural response which occur due to the wave forcing, depends on the properties of the waves and structure. In the following different types of structural responses and how they are defined in the present analysis are explained. Three of the response types are illustrated in figure 37.

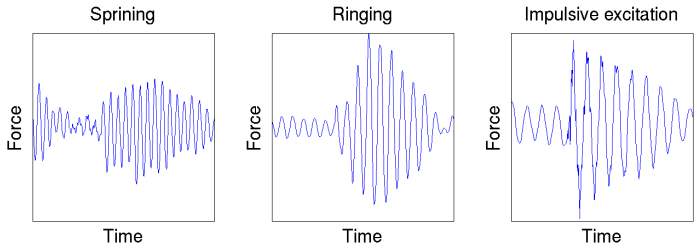


*Figure 37*: Example of springing, ringing and impulsive excitation.

### Broadband forcing

The structural first eigenfrequency of offshore wind turbines on monopile foundations is typically in the range 0.23-0.35 Hz. The peak frequencies of the most common sea states are therefore smaller than the structural eigenfrequency. The high-frequency part of the spectrum can however still contain energy at frequencies around the first structural eigenfrequency. The broad band forcing which can occur if the waves contain energy at the same frequency as the structure is thus very important in the structural design. This effect is linear and can therefore both occur for linear and nonlinear waves.

### Springing

When nonlinear waves develop energy is moved from the peak frequency to lower and higher frequencies. For very nonlinear sea states it is also possible to identify smaller peaks at the higher harmonics, i.e. at multiplies of the peak frequency. When the higher harmonics are close to the structural frequency there exist a larger risk of dynamic excitation of the structure. This type of excitation is happening continuously in time and is defined as springing.

### Ringing

Another nonlinear phenomenon which there has been an increasing focus on the last years in the offshore wind industry is ringing. The ringing phenomenon is related to intermittent resonant forcing of the natural frequency from nonlinear individual steep large waves. The response increases over some periods, before the maximum value is reached. The phenomenon was discussed intensively in the 1990s for deep water TLPs. Chaplin et al. (1997) state that ringing is a non-Gaussian process. Ringing, though is not an effect due to breaking waves or slamming, Faltinsen et al. (1995). Ringing is oftem associated with a secondary load cycle (Grue & Huseby 2002, Krokstad et al. 1998) which occur about one quarter wave period later than the main peak of the force. If the structural frequency is about 4 times the wave period this secondary load cycle causes a resonant response. de Ridder et al. (2011) found that waves with higher harmonics close to the structural eigenfrequency of the wind turbines resulted in excitation of the tower at its first mode. The detailed hydrodynamic forcing that leads to ringing-response in intermediate and shallow water is expected to be stronger than at deep water. This was confirmed by the investigations of Bredmose et al. (2012) and Paulsen, Bredmose, Bingham & Jacobsen (2013). Ringing is therefore also likely to be important in the design of offshore wind turbines both in ULS and perhaps also in FLS. In the standard DNV-OS-J101 (2010), it is said that ringing effects are only important when they are combined with extreme first order events, i.e. when an extreme wave occur and is therefore related to the ultimate design. Others on the other hand argue that ringing itself is a very important effect that can cause significant fatigue damage on a structure. In the research magazine Apollon (Vogt (2013)), John Grue, a professor at Oslo University, claimed that it is very important that ringing is taken into consideration.

### Impulsive excitation

Another type of response is impulsive excitation, which occur due to large steep waves and results in a sudden impulsive response of the structure which afterwards dampens. An example is shown in figure 37, where it is seen that the response experience a very abrupt excitation. This type of response is due to slamming and the response do not depend on what frequencies the energy in the wave has.

## 4.3 Aeroelastic model for wind turbine and inclusion of nonlinear wave loads

The 5MW NREL prototype wind turbine on a monopile foundation has been considered in the present task. The fully nonlinear wave model, the aero-elastic model Flex5 and the application of the wave loads within this code are described in the following.

### 4.3.1 Fully nonlinear wave kinematics

The wave kinematics were calculated by the fully nonlinear potential wave model OceanWave3D, Engsig-Karup et al. (2009), which solves the 3D Laplace equation for the velocity potential with nonlinear boundary conditions at the free surface and the impermeability condition at the sea bed. The model is based on a flexible-order finite difference approximation of the potential flow of non-overturning waves.

The OceanWave3D model was used to calculate unidirectional linear and fully nonlinear irregular waves moving up along a sloping sea bed. The waves were described by a linear JONSWAP-spectrum at the generation zone, as described in DNV-OS-J101 (2010). In this formulation the peak enhancement factor increases as the ratio $T_p/\sqrt{H_s}$ decreases. The larger the peak wave period, $T_p$, is compared with the significant wave height, $H_s$, the more energy is contained around the peak frequency in the spectrum.

The linear and nonlinear wave realizations of each sea state were generated by the same time series at the generation boundary. However the linear and nonlinear wave transformation are different and the significant wave heights are therefore not the same at the water depths where the wave realizations are studied. For a practical application the loads would always be based on a local value of the significant wave height. It was therefore decided to scale the results of the linear computation such that $H_s$ is identical at the position of the structure. Further, in accordance with DNV-OS-J101 (2010) Wheeler stretching was applied for the linear wave kinematics to avoid the over prediction of the particle velocities above the mean water level.

A consequence of using a fully nonlinear wave model is the possibility of wave steepening to the point of physical wave breaking. The wave model is only valid up to wave breaking, and very steep waves can cause a numerical breakdown. To handle the wave breaking a strong local filter was applied in the wave model. This is not an attempt to formulate a model for physical breaking but rather a way to solve the problem with high unphysical accelerations which the model can not handle. The breaking wave filter was applied every time $\frac{dw}{dt} \leq -1g$, where $w$ is the vertical particle velocity and $g$ is the acceleration of gravity. Physically it makes good sense to assume that the wave is breaking when $\frac{dw}{dt} = -1g$ i.e. when the particle experience a "free fall". The filter smoothens a 10-point region centered at the point which exceeds the defined value.

### 4.3.2 Flex5

The aeroelastic code Flex5, Øye (1996) has been used to model the structural dynamics of the monopile configuration. To validate the implementation of the NREL 5MW wind turbine in Flex5 the steady state responses were calculated and compared with the outputs from Jonkman et al. (2009). An example of the comparison is given in figure 38. The responses compare well.

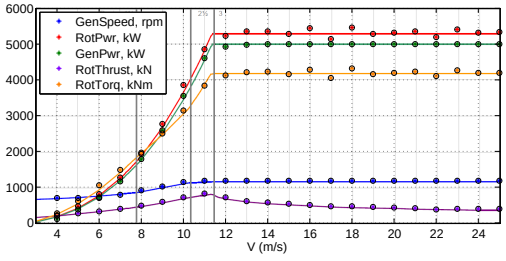


*Figure 38*: Steady-state responses as a function of wind speed. The figure is from Jonkman et al. (2009). The "dots" are plotted on top of the figure and are calculated from the present implementation.

The implementation was further validated against results of the Offshore Code Comparison Collaboration (OC3) for IEA Task 23 Offshore Wind Technology and Deployment, Jonkman & Musial (2010). Figure 39 compares the Flex5 implementation with three other codes for a load case where both wind and waves are present. The tower moment are very similar to University of Stuttgart (SWE) as seen in figure 39a and the inline force and overturning moment in the bottom of the monopile are similar to SWE and Risø, figure 39b and 39c.

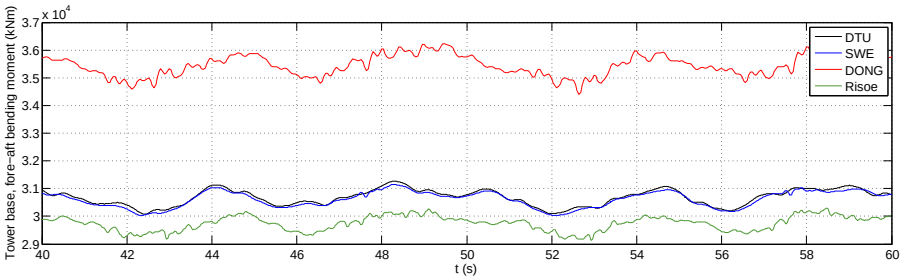


(a) Tower base fore-aft overturning moment.

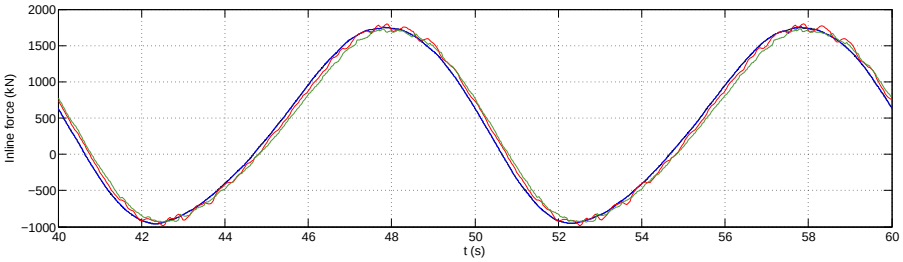


(b) Inline force at the sea bed.

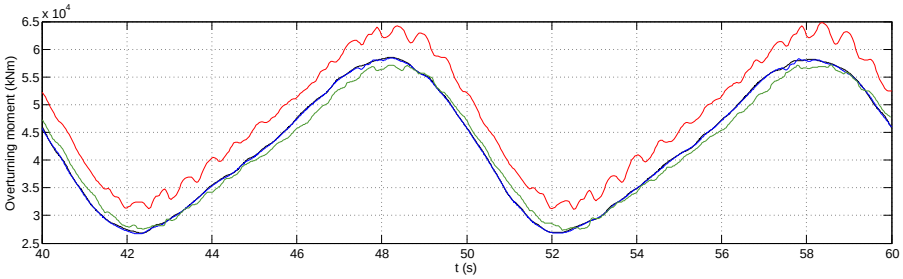


(c) Overturning moment at the sea bed.

*Figure 39*: Comparison of load case with a constant wind speed of $V = 8\,\mathrm{m/s}$ and a regular wave with wave height $H = 6\,\mathrm{s}$ and wave period, $T = 10\,\mathrm{s}$. The aeroelastic codes from SWE and DONG are also Flex5 while the code from Rise is HAWC2.

### The external forces in Flex5

The external forces in Flex5 are the aerodynamic forces from the wind and the hydrodynamic forces from the waves. The aerodynamic loads are calculated by the unsteady BEM method. The idea of the BEM-method is to determine the relative velocity felt by the blades. When this is known it is fairly easy to determine the lift and drag forces on the blades and from this the trust and power. With the unsteady method the dynamics of the incident wind and structural motion of the wind turbine is taken into account when the aerodynamic loads are calculated.

The calculation of wave forces on the monopile is performed within Flex5 by Morison's equa-

tion, (12). In the present analysis the Morison's equation was extended following the work of Rainey (1989) and Rainey (1995),

$$f_(z,t) = \rho\mathscr{A}(z)C_m a(z,t) + \rho\mathscr{A}(z)a(z,t) + \rho\mathscr{A}(z)C_m w_z(z,t)\,(u(z,t) - \dot{u}(z,t)) + \frac{1}{2}\rho C_D D\,(u(z,t) - \dot{u}(z,t))\,|u(z,t) - \dot{u}(z,t))\,|. \tag{12}$$

Here $\rho$ = 1025 m$^2$/s is the density of water; $\mathscr{A}(z)$ is the cross sectional area of the pile; $C_D$ and $C_m$ are the drag- and added mass coefficient respectively. In the main part of the analysis the drag and inertia coefficients had the generic values $C_D = 1$ and $C_M = C_m + 1 = 2$. The horizontal particle velocity and the horizontal particle acceleration are named $u(z,t)$ and $a(z,t)$ respectively, while the structural velocity and acceleration are named $\dot{u}(z,t)$ and $\ddot{u}(z,t)$. The third term in equation (12) is the axial divergence correction, which according to Manners & Rainey (1992) corrects for the assumption that the cylinder is slender in the vertical direction, which it is not. The structural acceleration, $\ddot{u}$ and $\ddot{v}$, is not subtracted from the particle acceleration in the added mass term. Instead the subtraction is included in the mass matrix in the aeroelastic code.

Following Rainey (1995) a final point force was added to the Morison's equation to represent the change of kinetic energy associated with the change of welted area,

$$F_s = -\frac{1}{2}\rho\mathscr{A}C_m\eta_x\,(u(z,t) - \dot{u}(z,t))^2\,. \tag{13}$$

Here $\eta_x$ is the slope of the surface elevation and represents the change of the surface elevation along the pile-diameter. Rainey (1995) explains that the pressure in the free surface region decays over a distance proportional to the cylinder radius. In case of a slender body as the monopile the pressure field constitutes a point load. The point load corresponds to the effect when a cylinder is dragged obliquely out of water. The water loses kinetic energy as the wetted part of the cylinder becomes smaller. The energy loss requires a force at the surface intersection. The axial divergence correction term in equation (12) and the point force, equation (13) are in the following named the "Rainey terms". The Rainey-terms were both included when the linear and nonlinear wave forcing was calculated. In this way it is only the wave kinematics that causes the differences in the linear and nonlinear wave forcing.

## 4.4 Effect of fully nonlinear wave forcing for a monopile wind turbine

The effect of fully nonlinear wave forcing on the structural dynamics of the wind turbine tower and monopile has been investigated by different analyses presented in Schløer et al. (2011), Schløer et al. (2012) and Schløer (2013). Here the main results from Schløer (2013) are repeated. However, in Schløer (2013) the calculated irregular wave realizations were not fully converged for wave frequencies larger than $\sim$0.22 Hz. In the results presented here, the wave realizations have been recalculated with a smaller grid resolution in the wave model to ensure a a converged solution.

The effects from the waves on the structure depend strongly on the properties of the structure. The tower is wind dominated and is only affected by the waves through the motion of the pile. As the monopile itself is relatively stiff compared to the frequencies of the wave forcing, it reacts mainly quasi-statically to the wave loads. The tower, however, is less stiff and gives rise to a first natural frequency of typically 0.23-0.35 Hz for the full structure. High frequency wave loads can thereby excite the tower through quasi-static motion of the monopile. Next the monopile will take part in the structural vibration associated with the first global natural frequency.

### 4.4.1 The wave realizations

Six representative wind speeds, $V$, with corresponding sea states as stated in table 8 was considered. In the table the turbulence intensity, $I_t$ and the six wind and sea states relative probability of occurence, $\hat{P}_{rel}$, are also stated.

| Wind and sea state | | 1a | 1b | 2 | 3 | 4 | 5 |
|---|---|---|---|---|---|---|---|
| $V$ | (m/s) | 2 | 6 | 9 | 15 | 20 | 28 |
| $H_S$ | (m) | 0.99 | 0.99 | 1.41 | 2.57 | 4.40 | 6.76 |
| $T_p$ | (s) | 5.50 | 5.50 | 6.17 | 7.56 | 9.16 | 11.41 |
| $I_t$ | (-) | 0.50 | 0.24 | 0.19 | 0.16 | 0.14 | 0.13 |
| $\hat{P}_{rel}$ | (-) | 0.10 | 0.30 | 0.35 | 0.22 | 0.04 | 0.002 |

*Table 8*: The six wind speeds and corresponding sea states, relative probability of occurrence and turbulence intensity.

The metocean data was provided by DONG Energy and the wave kinematics were considered at four different water depths, 40m, 35m, 30m and 25m, to include the effect of the water depth in the structural analysis. The diameter and thickness of the monopiles were chosen such that the structural first eigenfrequency was $\hat{f} = 0.27$ Hz at all four water depths.

The smallest and largest wind speed is below the cut-in wind speed and above the cut-out wind speed, respectively, to include situations where the wind turbine is parked in the analysis.

For each sea state both linear and fully nonlinear irregular two hour wave realizations were calculated. The waves were shoaled from a depth of 110 m over a uniform slope of 1:100.

The structural response due to the waves depends on the structural eigenfrequency and for which frequencies the waves contain energy. In figure 40 the wave spectrum of the linear and nonlinear wave realization of the third wind and sea state at a water depth of 30 m is shown. It is seen that the linear wave spectrum contains more spectral energy around the structural first eigenfrequency of 0.27 Hz. The energy in the nonlinear spectrum at frequencies larger than 0.35 Hz must therefore come from the part of spectrum between 0.18-0.34 Hz. The same observation was done for the fourth and fifth sea state. It was expected that the spectral energy which is distributed would have been taken more from the peak of the spectrum. This means that it actually is the linear spectra, which has most energy around the structural first eigenfrequency. The same result was found for the two largest sea states.

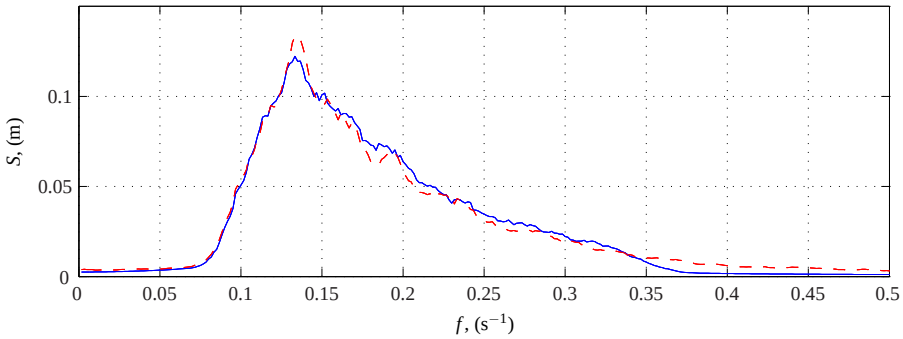


*Figure 40*: Power spectrum of the linear (solid) and nonlinear (dashed) surface elevation at a water depth of 30 m for a wave realization with $H_s = 2.44$m and $T_p = 7.56$s.

### 4.4.2 Morison force on fixed monopile

The linear and nonlinear wave forces are first compared for a fixed monopile. The analysis is interesting because it is independent of the structure and represents a typical load-input to an arbitrary structural model. In order to compare the linear and nonlinear wave realizations the probability of exceedance of the positive peaks of the surface elevation, inline force and overturning moment was calculated. The peak-values were sorted in increasing number and the probability of exceedance calculated.

In figure 41 the probability plots are shown for a water depth of $h = 30\,\mathrm{m}$

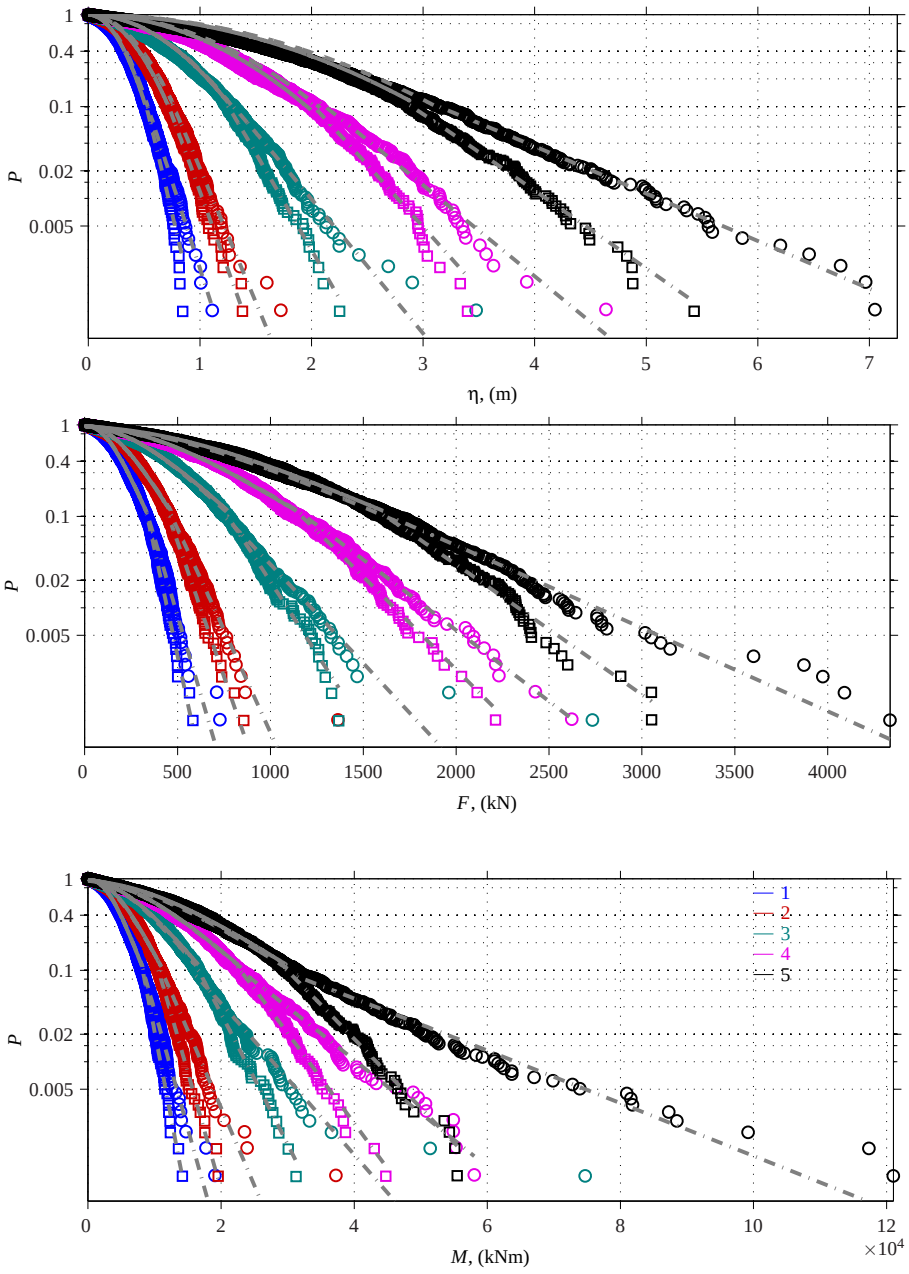


*Figure 41*: The probability of exceedance of the positive crest surface elevation, peak inline forces and peak overturning moments for $h = 30\,\mathrm{m}$. ∘ Nonlinear raw data, □ Linear raw data, – – Rayleigh/Gumbel distribution for linear peaks, – Rayleigh/Gumbel distribution for non-linear peaks, –·– Gumbel distribution for both linear and nonlinear peaks with $P < 0.1$.

The curves are fitted with probability density functions. The probability of exceedance of the surface elevation larger than $P > 0.1$ are fitted with the Rayleigh distribution, which is valid for linear narrow-banded spectra, while the force and moment are fitted with the Gumbel distribution for $P > 0.1$. The Gumbel distribution is normally used as a model for values which are maxima of a large number of independent variables WAFO-Tutorial (2011). Compared to the Weibull and Rayleigh distribution the Gumbel distribution represented the data best. The linear distributions are shown with a full line in the figures and the nonlinear distributions are shown with dashed lines in the figures. The extreme data (data which has a probability of exceedance smaller than $P < 0.1$) for both $\eta$, $F$ and $M$ are compared with the Gumbel distribution. In general the distributions represent the data well.

The peak values for both the linear and nonlinear realizations increase with increasing sea state and the nonlinear peaks are larger than the linear peaks at the same probability of exceedance.

To compare the quantiles more directly the ratio between the linear and nonlinear quantiles is calculated for the 0.01-quantiles and shown in figure 42.

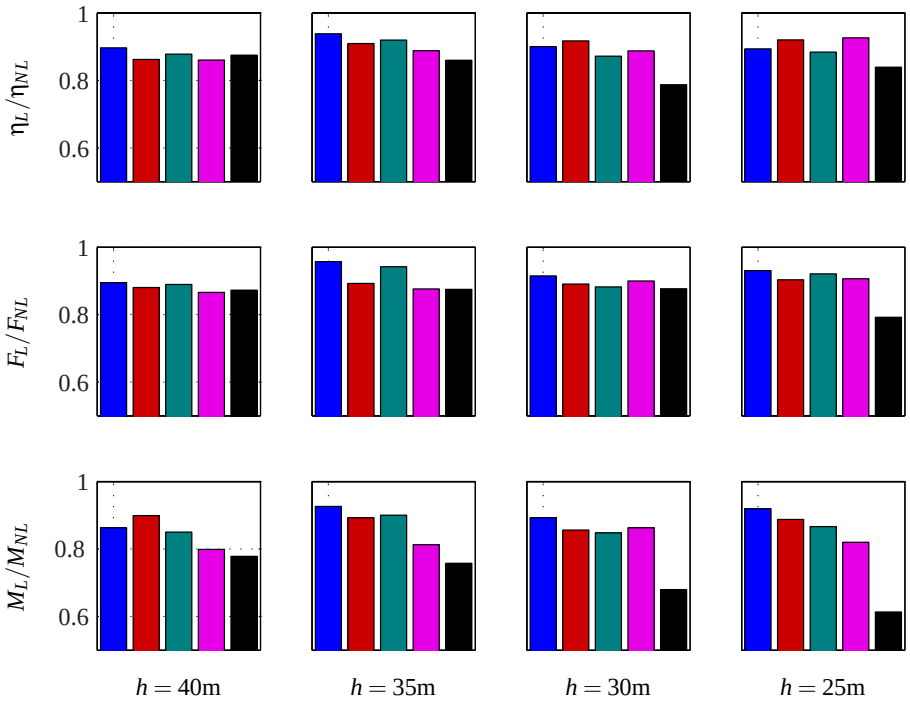


*Figure 42*: The difference between the linear and nonlinear peaks of the surface elevation, inline force and overturning moment at the probability of exceedance 0.01. ■ 1 ■ 2 ■ 3 ■ 4 ■ 5

The quantiles of the nonlinear surface elevation and force is 5-10 % larger than the linear quantiles, however it is difficult to see any clear trend in how the ratio changes as the water depth changes. The similarity between the ratio of the surface elevation and the inline force illustrates the linear relation between those two quantities associated with an inertia dominated structure where the dominant force contributon is due to the acceleration term in Morisons equation. For the overturning moment there is a more clear trend that the ratio between the linear and nonlinear quantiles increases as the wave height increases. This can be explained by the fact that the nonlinear load effects are strongest in the free surface region where the moment arm is also largest. For the largest sea state the ratio between the linear and nonlinear quantile of the crest elevation, force and overturning moment generally decreases as the water depth decreases. This is due to the increased nonlinearity for reduced depth.

### 4.4.3 Structural response

To understand the difference in the structural dynamics due to linear and nonlinear wave realizations the response of the tower and monopile in the aeroelastic calculations was considered. In the analysis 8 % of damping in logarithmic decrement was added to the first eigenfrequency of the tower and to the monopile to represent soil damping, hydrodynamic damping, structural damping and tower dampers.

The analysis was based on the overturning moment in the bottom of the tower and monopile.

Wavelet transformation was used to identify at which frequencies in the times series the energy content is large. Wavelet transformation is a method to localize special events in a signal both in time and frequency. In a Fourier transformation it is possible to investigate at what frequencies a signal contains energy. In a wavelet transformation it is further possible to investigate at what times the frequencies contain energy.

Figure 43 shows the wavelet transformation of the surface elevation and the moment in the bottom of the tower and monopile due to the linear and nonlinear wave realizations for wind and sea state *3*. The *y*-axis shows the frequency and the *x*-axis shows the time. In this wind and sea state the wind turbine operates and the arerodynamic forcing and damping is therefore significant. The wavelet transformations of both the linear and nonlinear surface elevation in figure 43a and 43b contain energy around the peak wave frequency of 0.13 Hz but contain also energy up to approximately 0.25 Hz. The wavelet transformation of the moments in the tower due to both the linear and nonlinear wave realization, figure 43c and 43d, are very similar. The response is therefore primarily due to the wind forcing and the effects from the waves must be dampened by the aerodynamic damping. In figure 43e and 43f the wavelet transformations of the moments in the monopile is seen. The linear and nonlinear wavelet transformations deviate a little more than those of the tower but it is clear that the wind forcing also affects the response in the monopile for example with low frequency oscillations below the peak wave frequency.

The figure shows that the effects from the waves are difficult to identify in the tower when the wind turbine operates, both because the wind forcing is dominating but also because the response due to the waves is dampened by the aerodynamic damping. It is therefore difficult to see the effects of the wave nonlinearity in such situations. The monopile is relatively stiff and exposed directly to the waves. The monopile therefore reacts mainly quasi-statically to the wave forces.

In situations where the wind turbine is not operating, the effects from the waves are easier to identify in the response of the tower and monopile. For wind and sea state *5* the wind speed is above the cut-out wind speed of the wind turbine. The blades are therefore pitched $87^\circ$. In figure 44-45 a time sequence of the overturning moment in the bottom of the tower and monopile due to wind and sea state *5* is presented for $h = 30\,\mathrm{m}$.

At $t = 1125\,\mathrm{s}$ and $t = 1300\,\mathrm{s}$ the moment in the tower due to the nonlinear wave realization is excited. Both excitations happen suddenly due to two large waves and the responses therefore look like impulsive responses. The linear surface elevation contains a large amount of energy at $t \sim 1330\,\mathrm{s}$ which excites the moment in the tower. However the response in the tower increases slowly and dampens slowly and not impulsive as is seen for the nonlinear wave realization. The moments in the monopile have a more quasi-static response compared to the tower but are also excited at the same times as the moments in the tower.

## 4.5 Accumulated effects of the wave nonlinearity through fatigue life analysis

Fatigue analysis is very important in the design of offshore wind turbines.

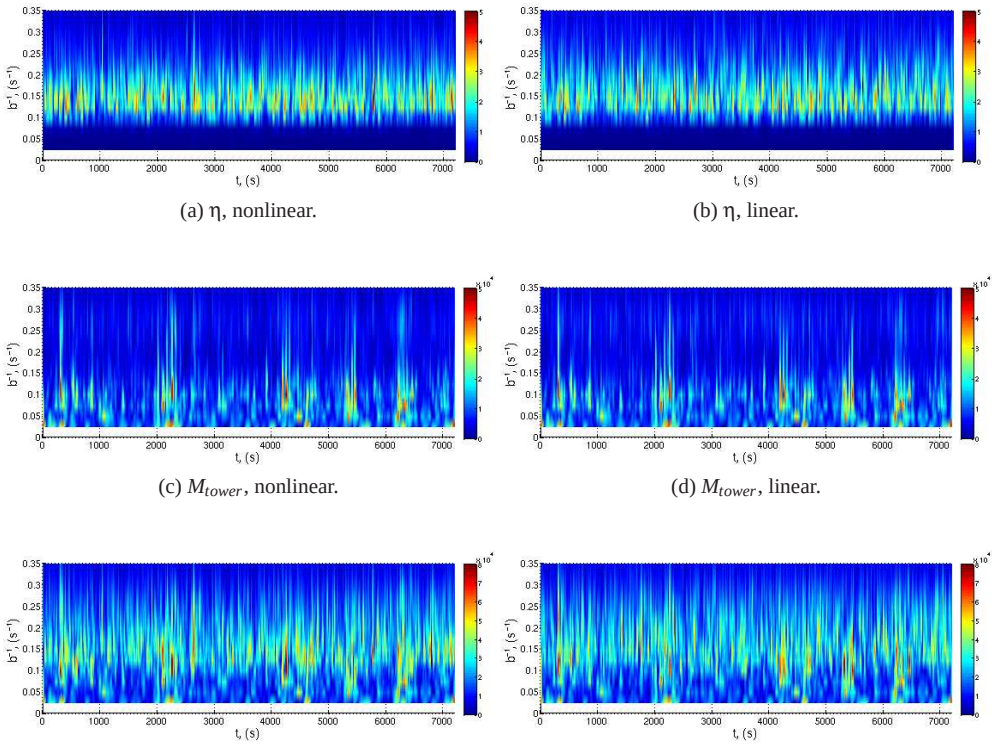

(a) η, nonlinear. (b) η, linear.

(c) $M_{tower}$, nonlinear. (d) $M_{tower}$, linear.

(e) $M_{monopile}$, nonlinear. (f) $M_{monopile}$, linear.

*Figure 43*: Wavelet transformation for wind and sea state *3*.

The fatigue analyses have been based both on equivalent loads and accumulated fatigue damage. The equivalent load range represents one load range value that for a certain number of cycles results in the same damage level as the investigated history of fatigue loads.

The accumulated fatigue analysis is a simple method to study the accumulated effects of the wave nonlinearity over the life time of the wind turbine. In these analyses the relative probability of occurrence of the 6 wind and sea states were used.

### 4.5.1 Accumulated fatigue damage

The fatigue calculations are based on the time series of the sectional moments in the bottom of the tower and monopile which are rain flow counted using the method defined in the IEA "Recommended Practices for Wind Turbine Testing and Evaluation; 3. Fatigue Loads", IEA (1990).

Given a load time series (e.g. for sectional overturning moment), the equivalent load range, $L_{eq}$, is defined by

$$L_{eq} = \left( \sum_i \frac{N_{s,i}(S_i)^m}{N_{eq}} \right)^{\frac{1}{m}} . \tag{14}$$

It represents one load range value that for a certain number of cycles $N_{eq}$ results in the same damage level as the original load time series. Here $S_i$ is the stress ranges of the cycles, $N_{s,i}$ is the number of occurence of each stress range and $m$ is the damage exponent of the material.

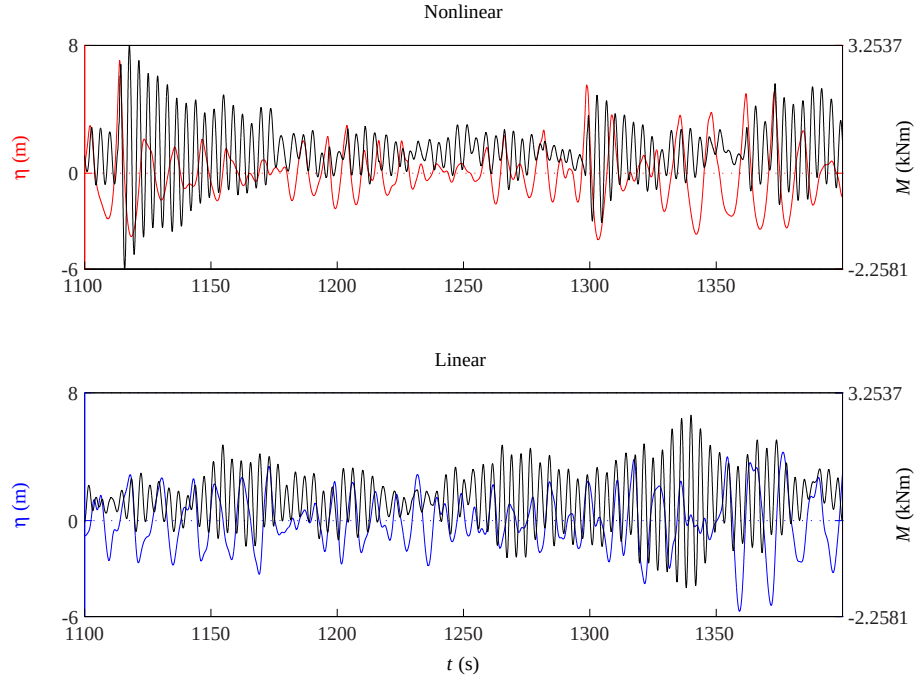


*Figure 44*: Nonlinear and linear surface elevation for the largest sea state and the corresponding moment in the bottom of the tower, $H_s = 6.76\,\text{m}$, $T_p = 11.41\,\text{s}$, $V = 28\,\text{m/s}$ and $I_t = 0.13$

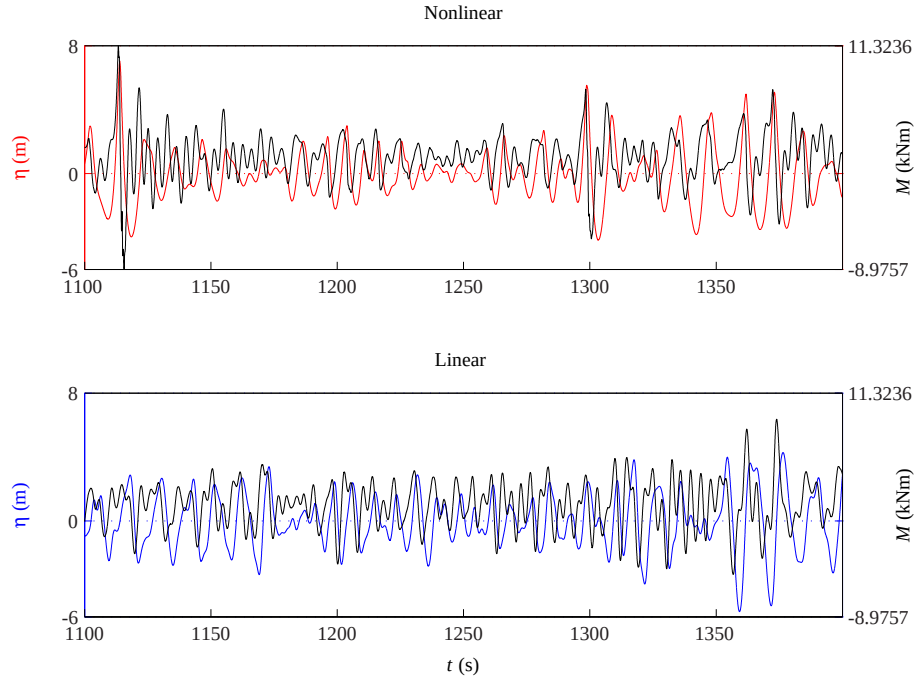


*Figure 45*: Nonlinear and linear surface elevation for the largest sea state and the corresponding moment in the bottom of the monopile, $H_s = 6.76\,\text{m}$, $T_p = 11.41\,\text{s}$, $V = 28\,\text{m/s}$ and $I_t = 0.13$

The accumulated equivalent load range for several realizations can be combined through

$$L_{eq,acc} = \left( \sum_j L_{eq,j}^m \frac{T_j}{T} \right)^{\frac{1}{m}}, \tag{15}$$

where the $j$'th load case occur the time $T_j$ and $T$ is the total time. This will be utilised to express

the effect of wave nonlinearity through the ratio of accumulated equivalent load range for linear and nonlinear waves $L_{eq,acc,Lin}/L_{eq,acc,NonLin}$.

The fatigue damage can be obtained from an SN-curve by

$$D = \sum_i \frac{N_{s,i}}{N^*} \left( \frac{S_i}{S^*} \right)^m \tag{16}$$

where $(S^*, N^*)$ define the SN curve. A damage of $D = 1$ corresponds to fatigue failure. By combination of (14)–(16), the ratio of fatigue damage of two sets of realizations can be calculated through

$$\frac{D_{acc,Lin}}{D_{acc,NonLin}} = \left( \frac{L_{eq,acc,Lin}}{L_{eq,acc,NonLin}} \right)^m . \tag{17}$$

This ratio defines another meassure for the effect of wave nonlinearity. It differs from the ratio of equivalent loads by the power of $m$.

In figure 46 the equivalent fatigue load ranges for linear and nonlinear waves is shown as function of the water depth for a damage exponent of $\mathsf{m} = 5$. They are obtained for a reference frequency of 1.0 Hz.

The equivalent loads decreases as the water depth decreases both in the tower and in the monopile, because the water column where the wave forces act decreases and also because the moment arm decreases as the length of the monopile decreases. Further, the diameter of the monopile also decreases with water depth, which also results in smaller wave forces. The decrease is smaller in the tower than in the monopile, because the tower is wind dominated.

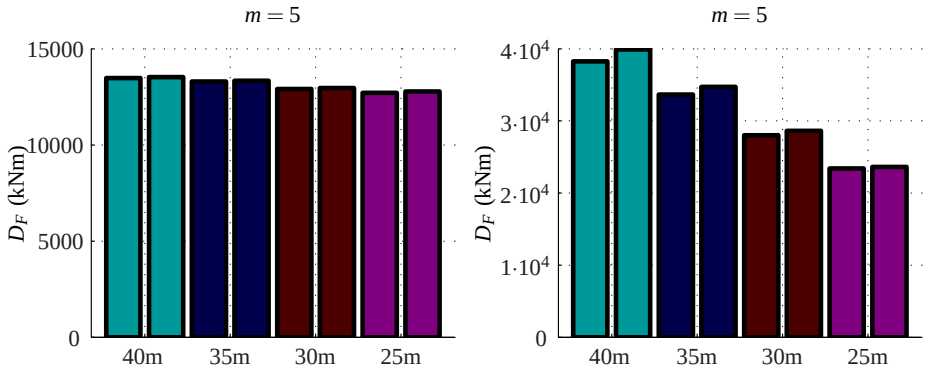


(a) Tower. (b) Monopile.

*Figure 46*: The total accumulated equivalent load ranges for both the linear (right) and nonlinear sea states (left) for all four water depths.

The ratio between the equivalent loads due to the linear and nonlinear sea states is shown in figure 47. A ratio smaller than 1 means that that the nonlinear equivalent fatigue load is largest while a ratio larger than 1 means that the linear equivalent fatigue load is largest.

In the tower the linear and nonlinear fatigue load is the same for $h = 40\,\mathrm{m}$ to $h = 30\,\mathrm{m}$. This is mainly due to the the dominance of the wind in the tower, but can also be due to the broad band forcing which was found to be largest for the linear wave realizations when the linear and nonlinear wave spectra were compared in figure 40.

For $h = 25\,\mathrm{m}$ the nonlinear fatigue load becomes larger than the linear fatigue load in the tower. This can be explained by the steep nonlinear wave excitation which increases as the water depth decreases.

In the monopile the nonlinear fatigue load is largest at all depths. However the difference decreases with the water depth. At $h = 40\,\text{m}$ the nonlinear fatigue load is 4 % larger while at $h = 25\,\text{m}$ the difference is only 1-2 %. This is mainly because the impact from the waves to the fatigue decreases with the water depth relatively to the contribution from the wind. Another mechanism which also supports this variation is that for the nonlinear wave realizations more and more spectral energy is moved to higher and lower frequencies as the water depth decreases, which means that the broad band forcing decreases. For the linear wave realizations the spectra do not change and the amount of broad band forcing is therefore more constant.

This result shows that the energy distribution in the wave spectrum can be very important for fatigue and that it in some situations can be more important than the actual size of the wave forcing, which was largest for the nonlinear wave realizations.

The largest effect of wave nonlinearity is thus seen for the monopile at a depth of 40 m, where the equivalent loads was 4% larger than for linear waves. The consequence for fatigue damage, however, is larger due to the power exponent of $m$ in the calculation of damage, see (17). The ratios for fatigue damage, is therefore shown in figure 48. Here the damage induced by nonlinear waves is about 18% larger for the monopile at 40 m depth. Due to the simple relation between equivalent load ratio and damage ratio of (17), the trends are the same as in figure 47 for equivalent loads.

It is important to note that diffraction effects are not considered in the present analysis. If the inertia coefficient in the calculations of the hydrodynamic forces was corrected for the diffraction effects, it is expected that the broad band forcing would decrease. For example, if the correction was included for a wave with frequency of 0.30 Hz on a water depth of 30 m the inertia coefficient would be reduced with $\sim 40$ % following the MacCamy-Fuchs-diagram shown in Sumer & Fredsoe (2006). For a wave of 0.25 Hz the inertia coefficient would be reduced with $\sim 12$ %. Further, if the correction is only applied on the free waves in the wave spectrum, the reduction would be the same for linear and nonlinear wave forces. This would cause the high-frequency waves to be less important in the fatigue damage and could imply that the larger waves would be more important in the fatigue damage, where the nonlinearity of the waves is stronger. The MacCamy-Fuchs correction was not applied in the present study, though, as it is only linearly consistent.

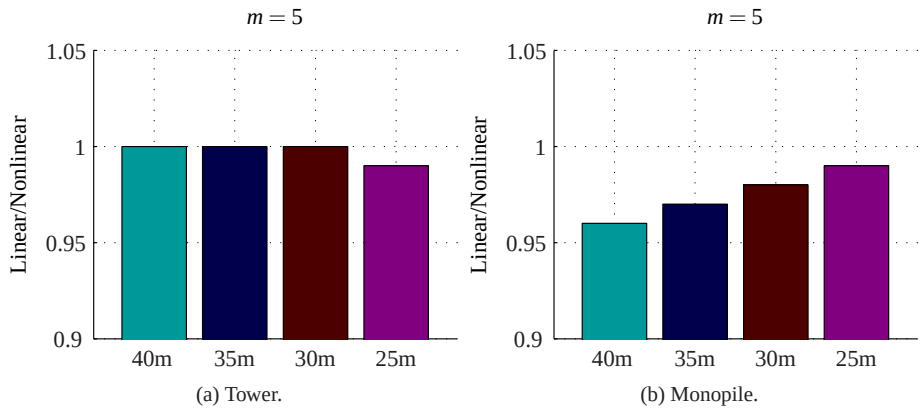

(a) Tower. (b) Monopile.

*Figure 47*: Ratio of accumulated equivalent loads for the linear and nonlinear sea states for all four water depths.

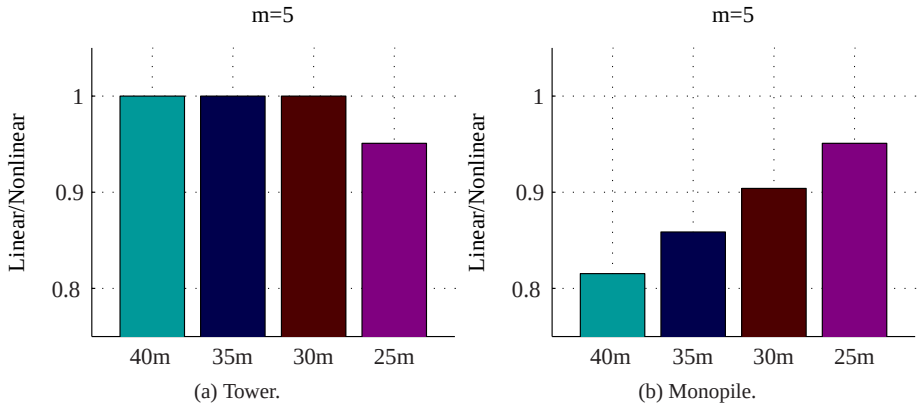

(a) Tower. (b) Monopile.

*Figure 48*: Ratio of accumulated fatigue damage for the linear and nonlinear sea states for all four water depths.

## 4.6 Aeroelastic response to CFD wave loads

The potential flow model, OceanWave3D, can not handle overturning waves. As described in section 4.3.1 OceanWave3D has a wave breaking filter, which takes out energy if a wave is close to wave breaking. However this does not model physical wave breaking. Also, all the analyses in section 4.4 and 4.5 were based on the Morison equation where the undisturbed wave kinematics are utilized. Effects as wave run up on the cylinder and detailed diffraction are therefore also ignored. One method to handle these effects are through CFD calculations, here with an OpenFOAM based solver, which directly computes the wave-structure interaction and the pressure acting on the cylinder. The wave forcing from OpenFOAM is considered to be more accurate than the wave forcing based on OceanWave3D and Morison's equation. It is therefore interesting to compare the structural dynamic response based on forces from OpenFoam and OceanWave3D and Morison's equation in relation to the design of offshore wind turbines.

The wave realizations were based on a model test carried out at DHI, see section 6, and was therefore calculated in model scale. The wave forces and wave kinematics from the calculations in OpenFOAM and OceanWave3D were afterwards scaled to full scale, before the forces and kinematics were included in the aeroelastic calculations in Flex5. The wave realization calculated in OpenFOAM was provided by "Task B" and is documented in Paulsen (2013).

In the experiment the cylinder had a diameter of $D = 0.164\,\text{m}$ and was placed in a water depth of $h_{cyl} = 0.55\,\text{m}$. The waves were generated at a water depth of $h_d = 0.82\,\text{m}$. At the downstream end of the domain, the water depth was $0.46\,\text{m}$. The ratio between model scale and full scale was 1:36.6. The nonlinear irregular wave realizations were based on a unidirectional JONSWAP spectrum with the target values $H_s = 0.23\,\text{m}$ and $T_p = 1.38\,\text{m}$ at the cylinder. The data are repeated in table 9 both in model scale and full scale.

| | $D$ (m) | $h_{cyl}$ (m) | $h_d$ (m) | $H_s$ (m) | $T_p$ (s) |
|---|---|---|---|---|---|
| Model scale | 0.164 | 0.5765 | 0.82 | 0.23 | 1.68 |
| Full scale | 6.00 | 21.10 | 30.01 | 8.3 | 10.2 |

*Table 9*: Experimental data in model and full scale.

The pressure on the cylinder calculated in OpenFOAM was at each time step converted into a single vertically distributed force by spatial integration of the pressure on the wetted area of the cylinder. The Flex5 load module was rewritten in order to read the distributed forces

from a text-file instead of the wave kinematics. The effects of the relative motion between the monopile and the water was accounted for through correction terms consistent with the Morison equation. This is detailed in Schløer (2013),

### 4.6.1 Wave kinematics

The duration of the wave realizations which were compared are 600 s. A time interval of the surface elevation from OpenFOAM and OceanWave3D is compared in figure 49. The two surface elevations compare quite well. For the largest waves the waves in OceanWave3D are more steep. This is because the waves in OpenFOAM experience some wave breaking during the calculations which round of the waves.

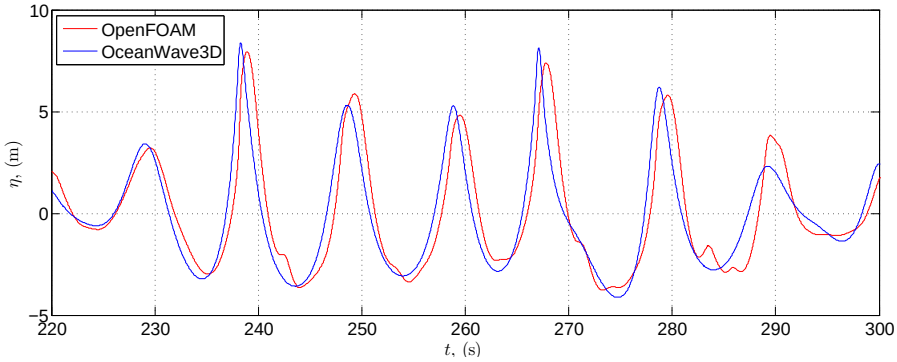


*Figure 49*: The surface elevation from OceanWave3D and OpenFOAM in a time interval with some large waves.

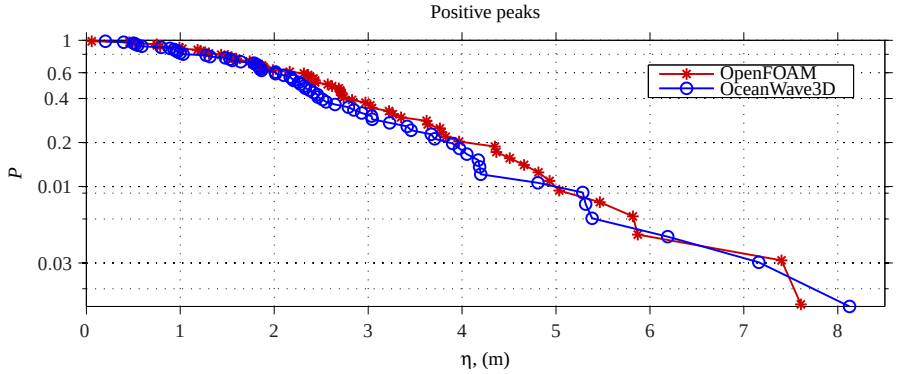


*Figure 50*: The probability of exceedance of the positive peaks in the surface elevation.

In figure 50 the probability of exceedance of the positive peaks of the surface elevations are compared. It is seen that the curves are similar but also that the surface elevation in OpenFOAM has larger positive peaks for all probabilities of exceedance except for the smallest probability of exceedance. So even though for the present example the crests of the surface elevation are more narrow in OceanWave3D they are generally not larger.

### 4.6.2 Dynamic analysis

Through static analysis where the hydrodynamic forces on a fixed monopile based on Morison's equation and from OpenFOAM is compared, the optimal values of the force coefficients were found to be $C_M = 1.65$ and $C_D = 1$ for the present wave realizations.

Generally it can be difficult to find force coefficients that represent both the smaller and largest

waves in the wave realization. The obtained force coefficients, though, were next used in the dynamic analysis in the calculation based on OceanWave3D and Morison's equation.

In the aeroelastic calculations a constant wind of 30 m/s was considered. The wind turbine is therefore parked and the blades pitched 87°. The aerodynamic forcing and damping are therefore small and it is possible to see the difference between the CFD-forces and Morison-forces in the response for the tower and monopile.

In figure 51 the probability of exceedance of the positive peaks of the overturning moments in the bottom of the tower and monopile are shown. In the monopile the CFD-force is largest for probability of exceedance larger than 0.03 while the three largest peaks are largest for the Morison forces. This can be due to the wave breaking which occur for the largest waves in OpenFOAM. This leads to less steep waves and thus smaller forces. In the tower the Morison force is largest for all probabilities of exceedance. The large deviation in the tower between the two types of forces are believed to be due to the steepness of the waves which is largest for the waves from OceanWave3D and result in more impulsive responses in the tower. This result indicates that even if the peaks of the hydrodynamic forces based on Morison's equation are correct the dynamic analysis can still result in different sectional forces due to dynamic excitation of the structure.

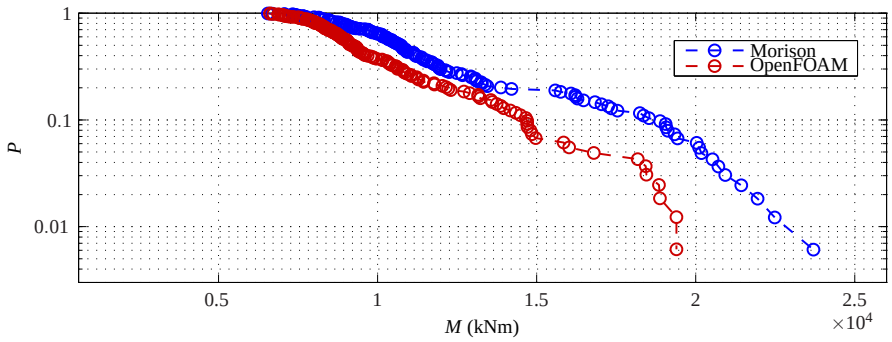


(a) Tower.

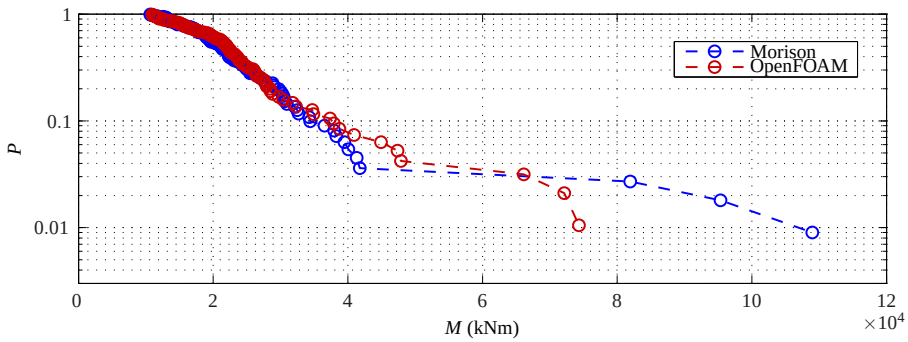


(b) Monopile.

*Figure 51*: Probability of exceedance of the overturning moment in the bottom of the tower and monopile.

## 4.7 Wind-wave misalignment and damping from waves and soil

In order to understand the importance of including wave nonlinearity in the analysis it is important to understand the damping which exist in an offshore wind turbine. Aerodynamic damping is the main damping factor. It exists primarily in the direction of the wind. When the wind tur-

bine is parked the aerodynamic damping is small and the effects from the waves more important in the structural response. Besides aerodynamic damping there exist other types of damping in an offshore wind turbine; soil damping, hydrodynamic damping, structural damping in the tower and the monopile and tower dampers.

The wind-wave-misalignment is further recognized to be an aspect which could be of great importance in the fatigue analysis, because of the small amount of aerodynamic damping in the direction of the waves. In such a situation it is also important to know the amount of damping which exist from the other types of damping.

In the present task the effect of misalignment on the fatigue damage was investigated for nonlinear waves and the hydrodynamic damping calculated. Also a new soil model was implemented into Flex5 to get a better description of the soil's interaction with the pile displacement and of the soil damping.

### 4.7.1 Wind-wave misalignment

The analysis was based on the same six wind and sea states as presented in section 4.4, but now the probability distribution for wind, waves and misalignment were included in the analysis based on data from the UPWIND-project[1]. The wind direction was for all wind and sea states in the fore-aft direction while seven wave directions were considered; 0° (fore-aft), 30°, 60°, 90° (side-to-side), 120°, 150° and 180°. The analysis were based on the overturning moments in the bottom of the tower and monopile in the fore-aft and side-to-side direction. A sketch of these two directions is shown in figure 52.

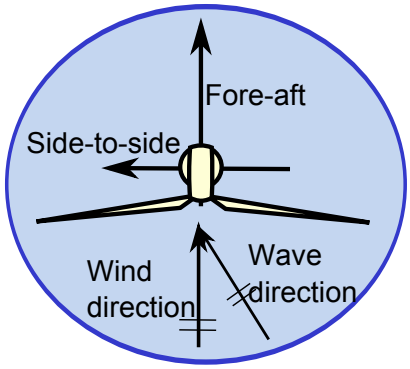


*Figure 52*: Sketch of a wind turbine seen from above. In the figure the definition of the fore-aft and side-to-side direction is given.

In figure 53 the linear and nonlinear accumulated equivalent fatigue loads are stated as function of the water depth, both in the fore-aft and side-to-side direction. The damage exponent is again $m = 5$ and the equivalent load ranges are computed for a reference frequency of 1.0 Hz.

In the fore-aft direction the fatigue load is only a little smaller than was obtained in section 4.5 where the waves and wind were aligned. This is because the dominating direction of the waves is still in the fore-aft direction and because the aerodynamic forcing results in the largest contribution to the fatigue damage. In the side-to-side direction the fatigue load is smaller than in the fore-aft direction, because the aerodynamic forcing is almost absent in this direction. It is further seen that the fatigue load decreases with the water depth in the side-to-side direction. The structural dynamics depends more on the wave forces in the side-to-side direction compared to the fore-aft direction, and the wave force contribution decreases with the water depth due to the smaller water column and moment arm.

[1] http://www.upwind.eu/

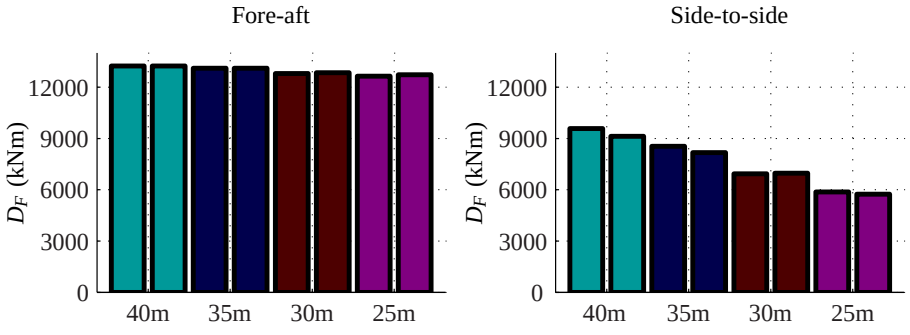


(a) Tower

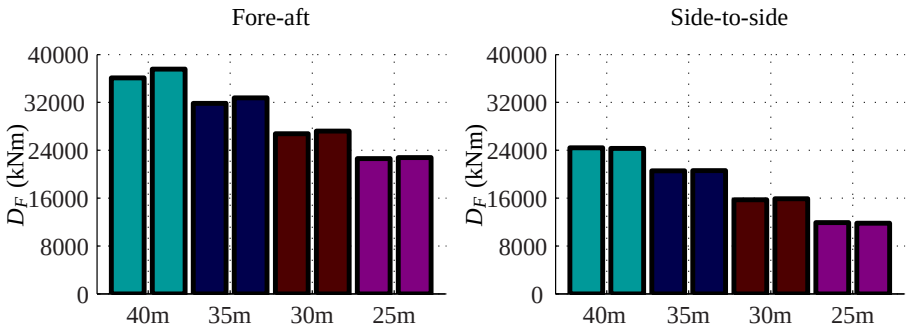


(b) Monopile

*Figure 53*: The total accumulated equivalent fatigue load range for all four water depths. For each water depth both the load range due to the linear wave realizations (left bar) and the nonlinear wave realizations (rigth bar) are given.

Figure 54 shows the ratio between linear and nonlinear equivalent fatigue loads both in the fore-aft and side-to-side direction for all four water depths. In the fore-aft direction the ratio of the fatigue load is practically identical to the situation with aligned wind and waves.

In the tower in the the side-to-side direction the obtained fatigue load with linear wave realizations is 5 % larger than for nonlinear waves at $h = 40\,\text{m}$ and $h = 35\,\text{m}$. This is because the effects of the broadband forcing becomes larger in the side-to-side direction due to the missing aerodynamic damping in this direction, and the broad band forcing is largest for the linear wave realizations. At $h = 30$ m, the linear and nonlinear equivalent loads are identical while for $h = 25$ m, the linear equivalent loads are 2% larger. The variation may be due to combined effects of increased energy transfer which reduces broad-band forcing for the nonlinear waves and increased steepness and nonlinearity which enhances the loads of the large waves.

In the monopile, in the side-to-side direction, the difference between the linear and nonlinear fatigue load is smaller than in the fore-aft direction. This is also explained through the broad band forcing which also affects the monopile. As for co-aligned wind and waves, this result shows that the energy distribution in the wave spectrum can be very important for fatigue and that it in some situations can be more important than the actual size of the forces from the larger waves, which were largest for the nonlinear wave realizations.

The associated ratios of fatigue damage, calculated by (17) are shown for reference in figure 55. As for the co-aligned case, the damage ratios are larger due to the power exponent of $m$. The largest effect occur for the monopile at 40 m depth, where the wave nonlinearity leads to an increase of about 18%.

A study with larger sea states presented in Schløer et al. (2012) where the wind velocity was smaller relative to the significant wave height showed that the nonlinearity of the waves can be

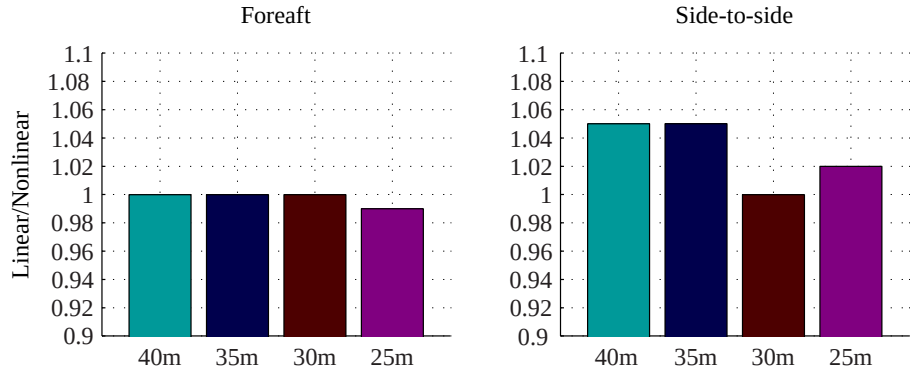


(a) Tower

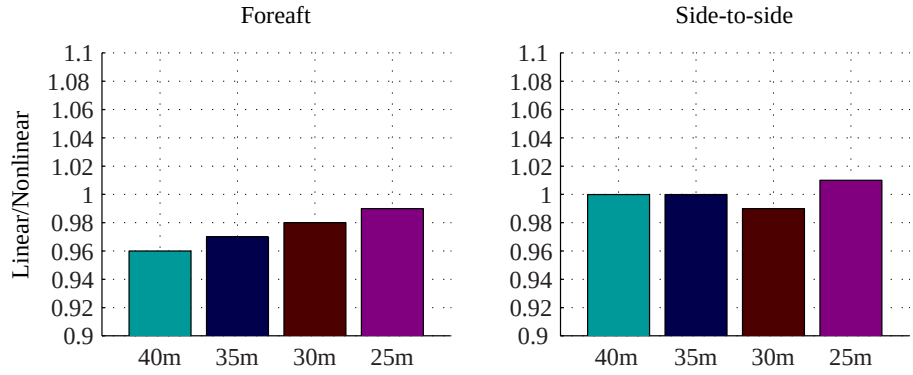


(b) Monopile

*Figure 54*: The ratio between the linear and nonlinear accumulated equivalent fatigue loads in case of misaligned wind and waves both in the fore-aft and side-to-side direction for $m = 5$.

important for fatigue. In the tower this was seen for situations where the aerodynamic damping was insignificant. In a study with misaligned wind and waves, the equivalent fatigue load in the side-to-side direction was 35 % larger with the nonlinear wave realizations. In the monopile the nonlinearity of the waves resulted in accumulated equivalent loads which were 5-8 % larger than the linear fatigue loads in the fore-aft and side-to-side direction. Hence, the effect of wave nonlinearity for fatigue depends on the metocean data as well as the choice of wind turbine and foundation.

### 4.7.2 Hydrodynamic radiation damping

The hydrodynamic wave radiation damping occur when the foundation oscillates and hereby generates outward propagating waves. The associated wave energy is extracted from the oscillations of the foundation, which is therefore dampened.

To calculate the radiation damping, the program WAMIT was used. WAMIT is a program to analyse the interaction between waves and offshore structures.

The shape functions used in WAMIT to describe the displacement of the monopile were based on Flex5's own shape functions for the monopile.

To calculate the damping ratio, the beam equation was considered, with inclusion of the hydrodynamic forcing terms

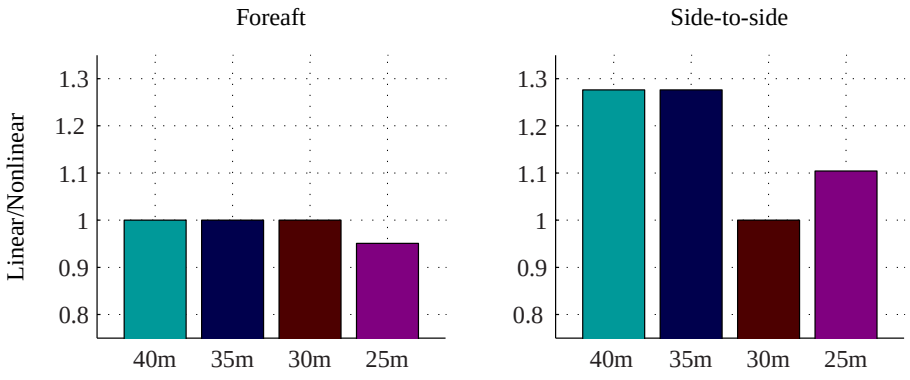


(a) Tower

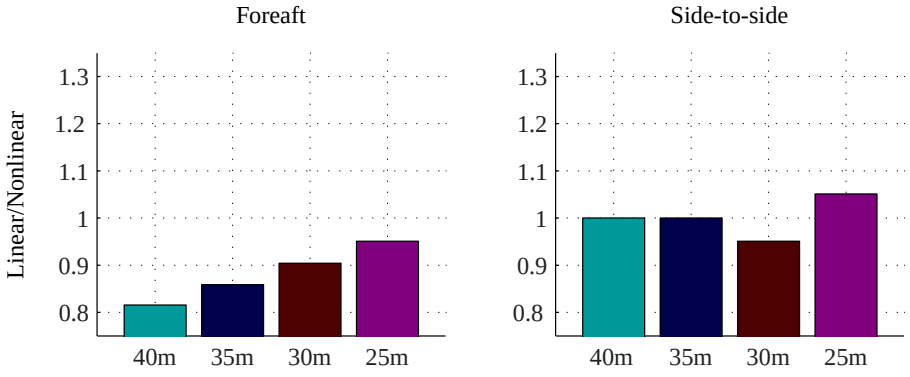


(b) Monopile

*Figure 55*: The ratio between the linear and nonlinear accumulated fatigue damage in case of misaligned wind and waves both in the fore-aft and side-to-side direction for $m = 5$.

$$\sum_{j=1}^{N} \left( (\rho\mathscr{A} + A_{ij})\ddot{u}_j + (B_{ij} + c_{ij})\dot{u}_j + ((EIu_{xx})_{xx} + C_{Rij})u_j \right) = F_j, \tag{18}$$

where $N$ is the number of degrees of freedom. The added mass ,A, and the damping, B, are hydrodynamic forces calculated in WAMIT and are functions of the angular frequency $\omega$. The hydrodynamic restoring force, $C_R$, is also calculated in WAMIT and is in the present analysis considered to be zero. The structural mass, $\rho\mathscr{A}$, and the structural stiffness, $(EIu_{xx})_{xx}$, are calculated in Flex5. The damping of the structure, c, are set to zero because it is the hydrodynamic damping which is investigated in the present analysis. The excitation force $F$ represents the Froude-Krylov force and diffraction forces, Faltinsen (1993).

The deflection $u_j$ can be expressed by a shape function and a generalised coordinate $u_j(t,z) = \varphi_j(z)\alpha_j(t)$. The two shape functions that Flex5 uses to describe the monopile deflection were used. The equation of motion, (18), can further be simplified by multiplying each term with $\varphi_i$ and integrate each term along the length of the beam, L, and reads then

$$\mathbf{GM}\underline{\ddot{\alpha}} + \mathbf{GK}\underline{\alpha} = -\mathbf{GA}\underline{\ddot{\alpha}} - \mathbf{GB}\underline{\dot{\alpha}}. \tag{19}$$

The stiffness matrix, **GK**, and mass matrix, **GM**, is calculated in Flex5 while the added mass matrix, **GA**, and the hydrodynamic damping matrix, **GB**, is calculated in WAMIT.

The matrices in equation 19 is given by

$$
\begin{aligned}
GM_{ij} &= \int_{-h}^{0} \rho \mathscr{A} \varphi_i \varphi_j dx, \\
GK_{ij} &= \int_{-h}^{0} EI \varphi_{i,xx} \varphi_{j,xx} dx, \\
GA_{ij} &= \int_{-h}^{0} A \varphi_i \varphi_j dx, \\
GB_{ij} &= \int_{-h}^{0} B \varphi_i \varphi_j dx.
\end{aligned}
\tag{20}
$$

In the present analysis it is the damping ratio of the structural first eigenmode of the whole structure which should be found. The equation of motion therefore has to be solved for the whole structure; monopile, wind turbine tower and wind turbine, which gives 24 degrees of freedom. The generalised coordinate is therefore a vector with 24 elements, and the full system of equations of motion is of size 24x24 with the same structure as equation (19). The forcing from the added mass and damping only exists in the water, i.e. for the two first shape functions. It is therefore only the first 2x2 elements which are nonzero in the added mass matrix and hydrodynamic damping matrix,

$$
GA_{24} = \begin{bmatrix} A_{1,1} & A_{1,2} & 0 & \dots & 0 \\ A_{2,1} & A_{2,2} & 0 & \dots & 0 \\ 0 & 0 & 0 & \dots & 0 \\ \vdots & \vdots & \vdots & \ddots & \vdots \\ 0 & 0 & 0 & \dots & 0 \end{bmatrix} \quad \text{and} \quad GB_{24} = \begin{bmatrix} B_{1,1} & B_{1,2} & 0 & \dots & 0 \\ B_{2,1} & B_{2,2} & 0 & \dots & 0 \\ 0 & 0 & 0 & \dots & 0 \\ \vdots & \vdots & \vdots & \ddots & \vdots \\ 0 & 0 & 0 & \dots & 0 \end{bmatrix}. \tag{21}
$$

If it is assumed that the hydrodynamic forcing on the right hand side of equations of motion is zero an eigenvalue problem occur with the solution $\underline{\alpha} = \underline{x}_0 e^{i\omega t}$. The equations of motion for e.g. the eigen vector associated with the first eigen frequency now read

$$
\mathbf{GM}_{24} \ddot{\alpha}_0 \underline{x}_0 + \mathbf{GK}_{24} \alpha_0 \underline{x}_0 = -\mathbf{GA}_{24} \ddot{\alpha}_0 \underline{x}_0 - \mathbf{GB}_{24} \dot{\alpha}_0 \underline{x}_0. \tag{22}
$$

Equation (22) is a system of force equations. By multiplying each term with the transposed of the eigenvector, $\underline{x}_0^T$, the system of equations is reduced to one equation of work

$$
\tilde{M} \ddot{\alpha}_0 + \tilde{K} \alpha_0 = -\tilde{A} \ddot{\alpha}_0 - \tilde{B} \dot{\alpha}_0, \tag{23}
$$

where

$$
\begin{aligned}
\tilde{M} &= \underline{x}_0^T \mathbf{GM}_{24} \underline{x}_0, \\
\tilde{K} &= \underline{x}_0^T \mathbf{GK}_{24} \underline{x}_0, \\
\tilde{A} &= \underline{x}_0^T \mathbf{GA}_{24} \underline{x}_0, \\
\tilde{B} &= \underline{x}_0^T \mathbf{GB}_{24} \underline{x}_0.
\end{aligned}
\tag{24}
$$

Next, these were evaluated for $\underline{x}_0$ of the first natural frequency. This makes it possible to calculate the damping ratio, $\zeta$, and logarithmic decrement, $\delta$

$$
\zeta = \frac{\tilde{B}}{2\sqrt{(\tilde{M} + \tilde{A})\tilde{K}}}, \tag{25}
$$

$$
\delta = \frac{2\pi\zeta}{\sqrt{1-\zeta^2}}. \tag{26}
$$

The mass, $\tilde{M}$, is calculated in Flex5 without including the added mass per length, $-\rho C_m \mathscr{A} \ddot{\alpha}$, where $C_m = 1$ is the added mass coefficient. This is done because the added mass from WAMIT is added to the mass, $\tilde{M}$, in equation (25). The eigen vector are on the other hand calculated in Flex5 where the added mass is included in the mass matrix, in order to get a shape which is identical to the one applied in the standard Flex5 calculations.

The hydrodynamic damping is calculated for four monopiles at four water depths with different diameters and thickness as stated in table 10. These configurations are identical the ones used in the fatigue analysis of the previous sections. The damping is found to be largest for the structural first eigenfrequency which is $\hat{f} = 0.27\,\text{Hz} \Leftrightarrow T = 3.7\,\text{s}$ for all the monopiles. In table 10 the damping ratio and logarithmic decrement damping is also stated for this frequency.

| | | | | |
|---|---|---|---|---|
| $h$ (m) | 40 | 35 | 30 | 25 |
| $D$ (m) | 6.5 | 6.5 | 6.3 | 6.1 |
| $t$ (mm) | 94 | 76 | 70 | 64 |
| $\zeta$ (%) | 0.07 | 0.06 | 0.04 | 0.04 |
| $\delta$ (%) | 0.42 | 0.38 | 0.27 | 0.25 |

*Table 10*: The damping ratio and logarithmic decrement for the four monopiles. Note that the numbers are given in percent, e.g. 0.07%=$7 \cdot 10^{-4}$.

The logarithmic decrement is largest for the largest water depth because the water column which dampens the structural displacement is larger and also the diameter of the pile is larger. If the damping of a wind turbine besides the aerodynamic damping gives a logarithmic decrement of 8%, the contribution from the radiation damping is small (0.42 %) but not small enough to be insignificant. However the damping was not found to be large enough to incorporate the radiation damping in Flex5 in this project.

### 4.7.3 Soil damping by a new soil model

Next to aerodynamic damping, soil damping gives the largest contribution to the overall damping of the wind turbine and the monopile. Unfortunately, this type of damping is very difficult to model. Today usually only monotonic *p-y* curves are used to describe the nonlinear soil stiffness in aerodynamic calculations, which describes the nonlinear elastic relations between the lateral displacement of the monopile, *y*, and the soil reaction, *p*, at a given vertical level. To model the soil damping a constant damping ratio is usually included in the aeroelastic model.

To get a better description of the soil's interaction with the pile displacement and of the soil damping, the soil model of Hededal & Klinkvort (2010) and Klinkvort (2012) was implemented in Flex5. The model offers a description of the cyclic pile-soil interaction and includes hysteretic damping from the soil and is in the following named the "Cyclic model".

#### The cyclic model

The soil model consists of two forces which are active in different phases during a cycle, $f_{face}$ and $f_{drag}$. In figure 56 the relation between the force in the soil, $f_s$, and the corresponding displacement of the pile, u, during two cycles are shown.

The force $f_{face}$ represent the loading phase, when the soil is loaded to a new extent. The pile pushes the soil and creates a gap behind the pile. The resistance starts to build up when the pile reaches the extremities in the gap in each direction, indicated with $\hat{\alpha}_{max}$ and $\hat{\alpha}_{min}$ in figure 56.

The build-up of the resistance is a linear elastic process, since the pile has been in that area before. The face force becomes active when the soil is loaded to a new extent. The maximum

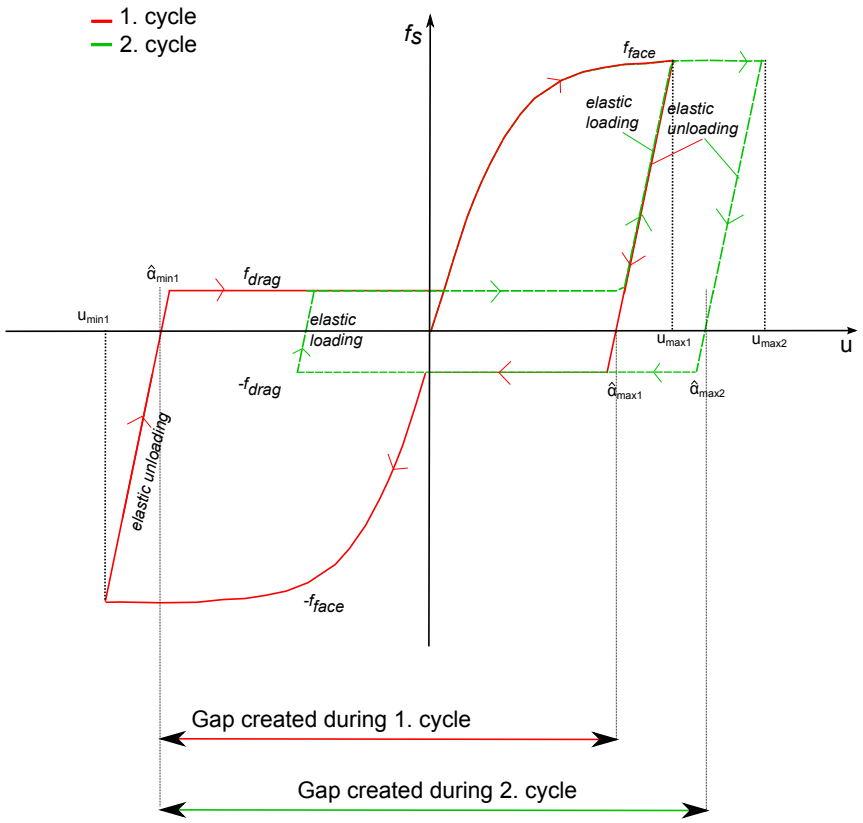


*Figure 56*: The spring element and the relation between the displacement and the force. Index "1" refer to the first cycle and index "2" to the second cycle.

loading in the two cycles in figure 56 is indicated with $u_{max}$ and $u_{min}$. The build-up of resistance and loading to a new extent can be described in one equation

$$f_s(u) = \begin{cases} (S_t(x)-1)\, f_{u,virgin}(u) + S_t(x)\,(-f_{u,virgin}(u_{min}) + k_s(u-u_{min}) \\ \qquad \text{for } u < \alpha_{min} + \frac{\Delta u}{|\Delta u|}\frac{f_{drag}}{k_s} \\ S_t(x)\, f_{u,virgin}(u) + (1-S_t(x))\,(f_{u,virgin}(u_{max}) + k_s(u-u_{max}) \\ \qquad \text{for } u > \alpha_{max} + \frac{\Delta u}{|\Delta u|}\frac{f_{drag}}{k_s} \end{cases} \tag{27}$$

where $\Delta u$ is the change in the displacement from previous to the present time step and the term $\frac{\Delta u}{|\Delta u|}$ therefore indicate whether the change in the displacement is positive or negative. The slope of the elastic loading is equal to the elastic soil stiffness $k_s$. The step function $S_t$ indicates whether the loading of the soil is linear elastic or determined from the virgin curve and is given by

$$S_t(x) = \frac{1}{1+e^{-2\beta x}}, \quad \text{where}$$
$$x = \begin{cases} u-u_{min} & \text{for } u < \alpha_{min} + \frac{\Delta u}{|\Delta u|}\frac{f_{drag}}{k_s} \\ u-u_{max} & \text{for } u > \alpha_{max} + \frac{\Delta u}{|\Delta u|}\frac{f_{drag}}{k_s}. \end{cases} \tag{28}$$

If $x \gg 0$ the step function is $S = 1$, if $x = 0$ the step function is $S = 0.5$ and for $x \ll 0$ the step function is $S = 0$. The larger the parameter $\beta$ is in equation (28) the more abrupt is the change of the step function from zero to one. According to Hededal & Klinkvort (2010) a typical value of $\beta$ is $1 \cdot 10^6$ and is therefore used here.

Hededal & Klinkvort (2010) used the API (2010) definition of the $p-y$ curves for sand to define the virgin curve, $f_{u,virgin}$. This is the same definition as given in DNV-OS-J101 (2010). The virgin curve describes the relation between the force and the displacement, the first time the soil is loaded to a new extent

$$f_{u,virgin} = A_s f_u \tanh\left(\frac{k_m z}{A_s f_u}\mathsf{u}\right). \tag{29}$$

Here $A_s = \max\left(0.9, 3-\frac{0.8z}{D}\right)$ is a strength reduction parameter, $f_u$ the ultimate bearing capacity, $k_m$ the soil modulus parameter, $z$ the depth below the sea bed and u the displacement.

When the pile moves in the gap created behind the pile, a drag force, $f_{drag}$, or friction along the sides of the pile exists. This process is plastic and the drag force is therefore constant. Klinkvort (2012) found from cyclic tests that the friction was in the range of 10 % of the maximum capacity of the soil. The drag force is therefore calculated as

$$f_s = \frac{A_s f_u}{10}\frac{\Delta\mathsf{u}}{|\Delta\mathsf{u}|}. \tag{30}$$

When the pile changes direction the unloading of the soil occurs linear-elastically. The slope of the elastic unloading is also equal to the elastic soil stiffness $\mathsf{k}_s$ and the soil force is calculated as

$$f_s = f_{s,old} + \Delta\mathsf{u}\mathsf{k}_s, \tag{31}$$

where $f_{s,old}$ is the soil force at previous time step.

A detailed description of the implementation of the model in Flex5 can be found in Schløer (2013). The implementation involved incorporation of a slaved shape function to represent the monopile deflection below mudline.

### 4.7.4 Dynamic analysis

To investigate the effects of the cyclic model in the aeroelastic calculations, the model was compared to a nonlinear elastic spring model, which in the following is named the "elastic model". In the elastic model the soil force is calculated using equation (29) as described in DNV-OS-J101 (2010), and therefore follows the virgin curve of figure 56. To compare the elastic model with the cyclic model a constant logarithmic damping in the monopile which represents the soil damping as good as possible was included in the elastic model. To find the amount of damping which should be added to the monopile a decay test where the start displacement is representative for a aeroelastic calculation was considered. It was necessary to add 40 % logarithmic decrement damping to the monopile in the elastic model to get the same amount of damping with the cyclic model. This resulted in a logarithmic decrement of 12 % of the first structural eigenfrequency. The reason that 40 % had to be added to the elastic model is that it is added as viscous damping. Viscous damping depends on the displacement, and the displacement of the pile is very small in the soil.

In figure 57 the dynamic response is shown for a wave realization with a significant wave height of $H_s = 6.75$ m and a peak wave period of $T_p = 11.41$ s. The wind speed is 28 m/s and above the cut-out wind speed. The blades are therefore pitched 87°. In the figure the deflection of the top of the tower and monopile and the overturning moment in the bottom of the tower and monopile is seen for a time sequence where two large waves at $t \sim 1725$s and $t \sim 1738$s occur and cause impulsive responses. Both in the tower and in the monopile the structural first eigenfrequency is excited with both models. In general both the deflection and the moment due to

the two models are very similar. However, in the monopile a high frequency oscillation of 1.3 Hz is observed in the cyclic model and are due to structural excitation by the intermittent onset of the elastic loading/unloading curve. This high frequency oscillation was only observed with the cyclic model and was also observed for wind and sea states where the wind turbine operates.

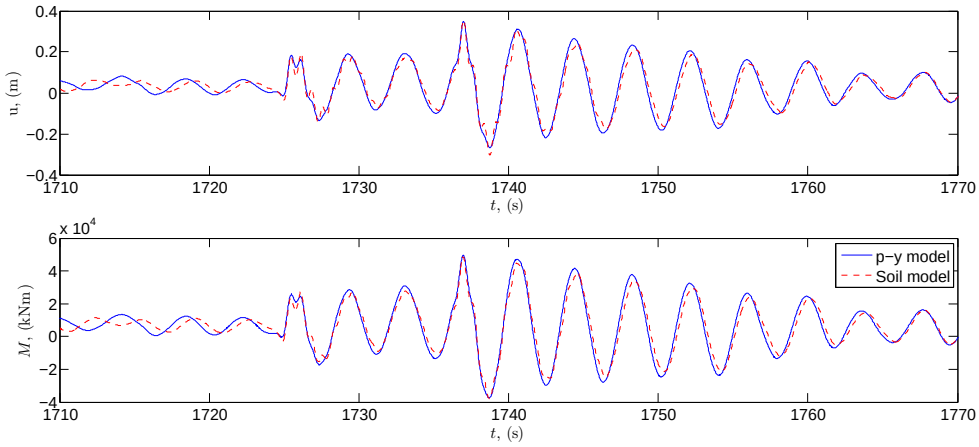


(a) Tower.

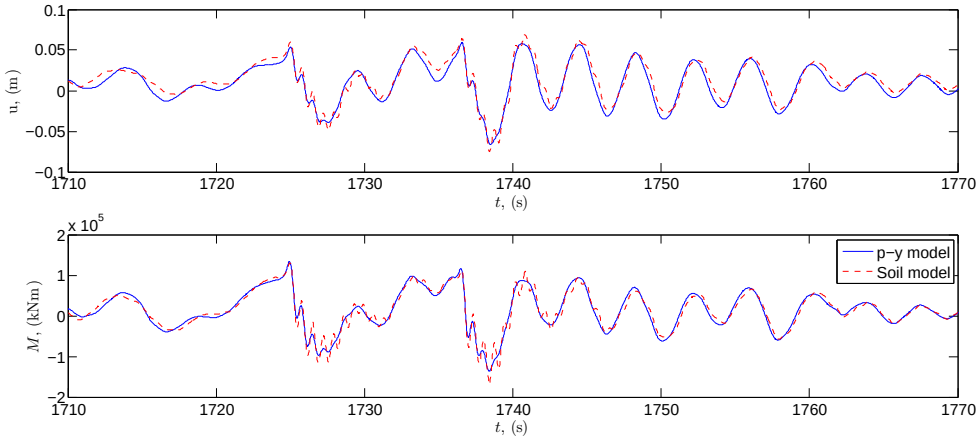


(b) Monopile.

*Figure 57*: The deflection in the top of the tower and in the top of the monopile and the overturning moment in the bottom of the tower and in the bottom of the monopile. Wind and sea state *5*.

The equivalent loads based on the overturning moments in the bottom of the tower and monopile due to three wind and sea states stated in table 11 were calculated with both models with a damage exponent of $m = 5$.

| Wind and sea state | $V$ (m/s) | $H_s$ (m) | $T_p$ (s) | $I_t$ (-) |
|---|---|---|---|---|
| 2 | 9 | 1.41 | 6.17 | 0.19 |
| 4 | 20 | 4.40 | 9.16 | 0.14 |
| 5 | 28 | 6.75 | 11.41 | 0.13 |

*Table 11*: Wind and sea state *2*, *4* and *5*.

In figure 58 the ratio between the equivalent loads due to the elastic model and the cyclic model is shown. If the ratio is smaller than 1, the cyclic model results in the largest equivalent loads. In the monopile the equivalent loads due to the soil-model are approximately 5 % larger than those due to the elastic model. This is due to the high frequency oscillation observed with the cyclic model. The difference is largest for case *5*.

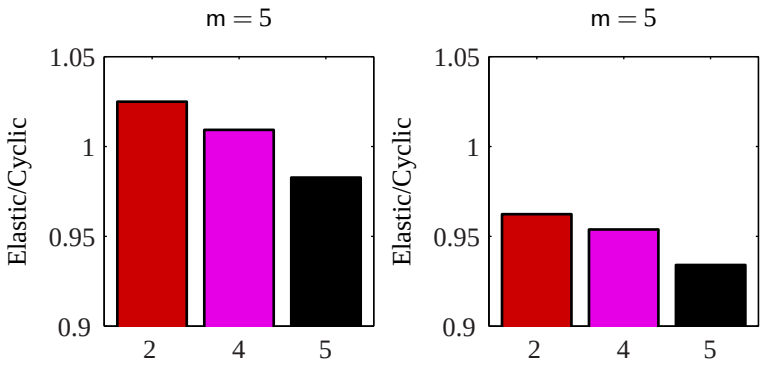

(a) Tower. (b) Monopile.

*Figure 58*: Difference between the equivalent loads for wind and sea state *2*, *4* and *5* with the elastic model and the cyclic model.

In the tower the difference between the two models are smaller. For wind and sea state *2* and *4* the equivalents loads are 1-2 % smaller in the cyclic model while the equivalent loads for wind and sea state *5* are 2 % larger in the cyclic model. The high-frequency oscillations which in the monopile lead to larger equivalent loads with the cyclic model is not as pronounced in the tower, which can explain that the difference between the equivalent loads are smaller in the tower. Further, the constant damping in the elastic model is based on a representative deflection from wind and sea state *5*. This damping-value is might be a little too small when the two other sea states is considered. This may explain why the equivalent tower loads with the elastic model are largest for wind and sea state *2* and *4*.

## 4.8 Summary

Fully nonlinear wave loads have been coupled with the FLEX5 aeroelastic model and the structural response and fatigue loads due to linear and nonlinear irregular wave realizations have been analysed for a monopile-based wind turbine.

The static analysis of the wave forces showed that the nonlinear wave realizations resulted in larger inline forces and overturning moments and that the difference between the linear and nonlinear forces and moments increased with increasing significant wave height. For the largest sea state a clear trend showed that the difference between the linear and nonlinear wave forces increased with decreasing water depth, due to the increased nonlinearity at reduced depth. For the 1% quantile, the sectional force at mudline from nonlinear waves was about 10% larger at 40 m depth than for linear waves. This deviation was typically larger for moments at the mudline. At 25m depth, the nonlinear 1% quantile moment was nearly 40% larger than the linear. More extreme differences occured at smaller probabilities of exceedance. Here, however, the results are likely to be sensitive to the wave breaking filter applied, which may have lead to too large waves.

The dynamic response in both the tower and monopile was investigated for co-directional wind and waves. When the wind turbine was operating, the aerodynamic forces were dominating

and much stronger than the forces from the waves, and it was difficult to see a difference between the response due to the linear and nonlinear wave forcing in the tower. In situations where both the aerodynamic forces and damping were insignificant, excitation of the structural first eigenfrequency due to high frequency wave loads was seen. The monopile reacted quasi-statically to the wave loads and induced excitation of the structural first eigenfrequency with a significant oscillation of the tower.

The effect of wave nonlinearity for fatigue was quantified by calculation of the ratio of accumulated equivalent loads. The effect was found to increase with water depth. For $h = 25$ m the wave nonlinearity lead to an increase in equivalent load at the bottom of the monopile of 1%, while at 40 m, the effect was about 4%. Expressed in terms of fatigue damage, the wave nonlinearity lead to an increase of about 18% for the monopile at 40 m. This shows that wave nonlinearity can be important for the fatigue and points at the necessity of further investigations. This is outlined under further work. For the tower, the effect of nonlinearity was small and only occurred for the depth of 40 m.

The effects of wave nonlinearity were also investigated in a misaligned wind and wave climate for the same six wind and sea states. For the fore-aft direction, the results were practically identical to the results for co-aligned wind and waves. For the side-to-side direction, the effect of the broad band forcing increased due to lack of aerodynamic damping which amplified the effects from the waves. The linear accumulated fatigue load in the tower was larger than the nonlinear accumulated fatigue load for the two largest water depths in the side-to-side direction. This result shows that the energy distribution in the wave spectrum can be very important for fatigue and that it in some situations can be more important than the actually size of the wave forcing, which was largest for the nonlinear wave realizations.

The hydrodynamic damping was calculated in WAMIT and was found to be between 0.2 % and 0.5 % in logarithmic decrement. This damping is therefore small compared to other damping effects, however not small enough to be neglected. The damping increases with increasing water depth.

A cyclic soil model was implemented in Flex5 to investigate how the soil affects the response of the monopile and tower. The cyclic soil model was compared to an elastic soil model with standard $p-y$ curves and a constant damping factor. The comparison showed that the overall damping from the soil can be represented by a constant damping term. However, it is necessary to change the damping according to the conditions that are investigated as the damping ratio for the cyclic soil model is amplitude-dependent. Further it was seen that the cyclic model results in larger excitations of the structural eigenfrequency of 1.3 Hz and that these excitations leads to larger equivalent loads. For the present cyclic model this means, that even if the constant damping is chosen correctly it may still be non-conservative to use the elastic model as the detailed and sometimes rapidly varying soil force is not included in that model

## 4.9 Suggestions for further work

The results of this task lead to many new and follow up questions which should be investigated in further work. The most prevailing questions are mentioned below.

- An improvement of the wave-breaking description in the wave model would clear up the uncertainties in the analyses, when the largest waves are considered.
- The analysis of effect of nonlinearity should be extended to include ULS wave loads for realistic design load cases and with inclusion of the dynamic response. This is very important as ULS loads are often design-driving. Further the static analysis of nonlinear wave loads showed that the difference between linear and nonlinear extreme wave loads can be very large

- An incorporation of diffraction effects on the added mass coefficient would improve the analysis. The MacCamy-Fuchs theory is valid for linear waves only and was not included in the present analysis because it was not possible to distinguish between the free and bound waves in the nonlinear wave realizations. However, it is expected that the effects from the broad band forcing will decrease if diffraction is taken into account because it leads to smaller inertia coefficients for the waves in the high frequency part of the wave spectra.
- A more thorough fatigue study should be conducted where more load cases are considered in the analysis to investigate the effects of the nonlinearity more deeply.
- An investigation of prototype scale measured data to detect true ringing/excitation effects from waves would be highly valuable. Ideally, the measured response could be compared directly to the numerical computations with the present models
- It would also be interesting to improve the soil model, such that the description of the full extent of the monopile is included in the calculations. Further, the model of Klinkvort **(**2012**)** should be implemented. This model includes the back filling of the soil in the gap, which most likely will cause more dynamic responses due to soil.
- The analysis has further considered direct application of CFD wave loads and inclusion of wave directionality, both with a main focus on quantifying the load effects relatively to the unidirectional wave loads based on the undisturbed wave kinematics. It could be interesting to make more dynamic analysis with the forces from the CFD-solver to quantify the apparent load reduction associated with the more detailed CFD-description of the waves. A larger analysis of the importance of the multi-directional seas, both linear and nonlinear, should also be conducted, where more sea states are considered. Both these analyses can supplement the present study and contribute to the understanding of the importance of including the wave nonlinearity in the design of offshore wind turbines.

# 5 Task C(2): Influence of nonlinear wave loads on jackets

**Torben Juul Larsen, Taeseong Kim and Anders Melchior Hansen (DTU Wind Energy)**
with contributions from Signe Schløer

## 5.1 Introduction

In task C(2), a wind turbine mounted on a jacket was investigated with respect to the influence of nonlinear wave load contributions. The study was carried out for a stand still situation where the turbine is stopped and the blades are pitched 90°. The investigated standstill situation is with waves in a direction directly towards the wind turbine direction. Since the blades are pitched, the aerodynamic contribution was considered very low and aerodynamic loads on the tower were also neglected. This load condition is considered highly relevant for offshore turbines and is known to be problematic for monopile configurations since the total level of structural, aerodynamic and hydrodynamic damping generally is very low at stand still.

Investigations were also made for operational conditions with co-aligned wind and waves to assess the fatigue effects during situations with stronger aero-dynamic damping. An investigation for operational, mis-aligned wind-wave conditions has been carried out as well.

Even though the structural part of the HAWC2 code is capable of modelling a complex grid structure as a jacket, the many degrees of freedom (DOF) significantly slowed down the code. Several steps was done in order to ensure as fast, yet accurate, simulations as possible. This included pre-generation of wave kinematics, improvements of the solver including a consistent formulation of the added mass from water. Finally, a super element method to reduce the number of DOFs (Degrees of Freedom) was developed. This enables considerable speed-up of the dynamic aero-elastic calculations with the jacket structure.

### 5.1.1 Main achievements

The main achievements of the work are

- Incorporation of fully nonlinear wave loads in the aero-elastic code HAWC2
- Assesment of effect of nonlinear wave forcing on a jacket mounted offshore wind turbine in stand-still conditions
- Investigation of fatigue effects from nonlinear wave forcing during operation in co-aligned and mis-aligned wind and waves
- Implementation of pre-generated wave kinematics in HAWC2
- Development of a consistent incorporation of added mass into the HAWC2 solver
- Development of a super-element formulation for the jacket substructure in HAWC2

The work has been published in a conference paper (Larsen et al. 2011*b*) and two conference posters (Larsen et al. 2011*a*, Hansen et al. 2013). An overview of the results are provided in the following.

## 5.2 The HAWC2 model

The structural part of the code is a multibody formulation based on the floating frame of reference method as described in Larsen & Hansen (2007), Kim et al. (2013). In the particular formulation of the code, the turbine structure is subdivided into a number of bodies where each body has its own coordinate system. Within each body the structure consists of an assembly of linear Timoshenko beam elements. The nonlinear effects of the body motion (rotations and deformations) are accounted for in the coupling constraints in between the individual bodies, ensuring small deflections within the linear beam elements. This means that effects of large rotations and deflections are included using a proper subdivision of a blade to a number of bodies. The aerodynamic part of the code is based on the blade element momentum theory (BEM), however extended from the classic steady state description to handle dynamic inflow, dynamic stall, skew inflow and effects from operating in sheared inflow. The dynamic stall model Hansen et al. (2004) consists of a modified Beddoes-Leishmann model Leishman & Beddoes (1986) that includes the effects from shed vorticity from the trailing edge Theodorsen (1935) as well as the effects of stall separation lag caused by an instationary trailing edge separation point. Variations in the induction over the rotor, caused by operation in sheared inflow are described in Madsen et al. (2011). The inflow turbulence is generated using the Mann model Mann (1998), which is a non-isotropic full 3D correlated turbulent flow field corresponding to the Navier-Stokes solution of a turbulent flow. Tower shadow effects are included using a potential flow method. The code verification has been performed through the Offshore Code Comparison Collaboration (OC3) and Offshore Code Comparison Continuation (OC4) under the IEA Wind Task where HAWC2 results are validated against other numerical tools such as BLADED, ADAMS, FAST, FLEX, etc. Popko et al. (2012), Vorpahl et al. (2013). The full system natural frequencies, dynamic loads and displacements are compared in OC3 and OC4. From the comparisons, it has been shown that the full system natural frequencies, the dynamic loads and the system responses obtained by HAWC2 agree well with other aeroelastic codes. A full scale validation of simulated and measured wind turbine load levels have recently been presented in Larsen et al. (2012) showing a very good agreement. The simulation time is typically between real time and two times slower than real time depending on the turbine and situation analyzed. The wave load are implemented using Morison method Morison et al. (1950), however with the inertia terms split up in an added mass contribution and a Froud-Krylov part. Bouyancy is handled by integration of external pressure contributions.

## 5.3 Jacket and turbine model

In order to investigate the influence of nonlinear wave loads on a relevant and replicable design, the fictious 5MW wind turbine Jonkman (2009) used in the benchmark projects IEA Annex 23 OC3 and IEA Annex 30 OC4 has been used for the modeling of the wind turbine. The jacket design is also from IEA Annex 30 OC4 Vorpahl et al. (2011), which is based on a design previously used in the European research project UPWIND. The turbine and jacket are sketched in Figure 59 and Figure 61 (right). The jacket design consist of 4 corner piles interconnected by 3 sets of braces in X-configuration. The piles are flooded, whereas the braces are closed and thereby contributes significantly with buoyancy. The top of the jacket includes a transition piece to the tower bottom 20m above still water level. This consist of a large volume of reinforced concrete with a total mass of 660t. This configuration seem to be a heavier construction than several other jacket designs, however it was chosen for the IEA Annex 30 project and therefore also used in this study. The fictitious turbine has a rotor diameter of 126m and a hub height of 90m. The top weight consisting of nacelle and rotor is 350t. The still water level is 50m. A general validation of the turbine and jacket model can be found in Popko et al. (2012) and Vorpahl et al. (2013)

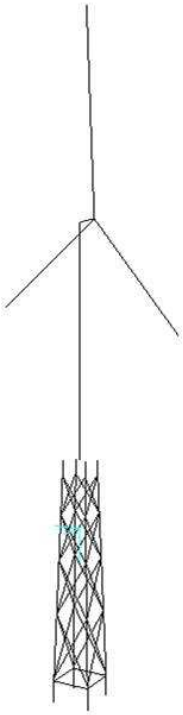

*Figure 59*: Illustration of the jacket and turbine model in HAWC2 used for the study.

## 5.4 Wave loads applied

The significant wave height and peak period and depth are shown in Table 12 and in Figure 60, where the model validity of classical wave theories and wave breaking criteria are also shown. The wave data was selected to be representative for waves in the North sea and are all outside the valid range for linear wave theory. It should be noted that the wave conditions are not identical to those of the monopile study of section 4.

Since the focus in this paper is both the influence of extreme loads and fatigue loads every stochastic simulation case consist of three half-hour simulations, each with different seed input. The nonlinear wave solution is however computed for several hours, so instead of choosing different seeds, different half-hour time windows were used. The max,min,mean values as well as equivalent fatigue loads were calculated as the average value of the three simulations to decrease the statistical uncertainty.

*Table 12*: Wave data for the 5 selected wave cases.

| Case no. | $H_s$ | $T_p$ | kh |
|---|---|---|---|
| 1 | 2.27 | 6.84 | 5.2 |
| 2 | 3.11 | 7.92 | 3.5 |
| 3 | 5.11 | 10.46 | 2.2 |
| 4 | 7.15 | 12.32 | 1.6 |
| 5 | 9.46 | 14.16 | 1.3 |

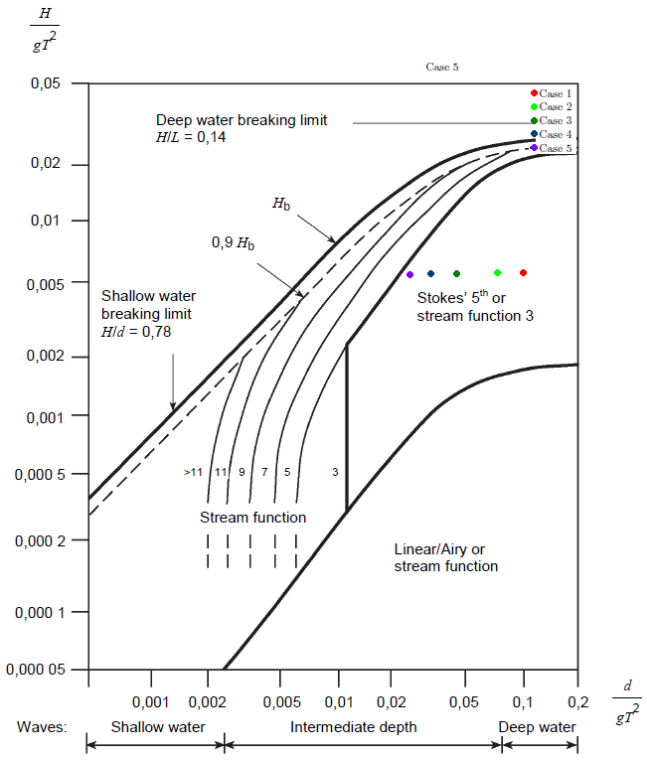


*Figure 60*: Illustration of the wave properties of the five selected wave cases.

## 5.5 Standstill situation, blades pitched 90°

A set of sensors has been compared for the different load cases. First of all the wave elevation was compared in Figure 61 (left). In this figure it is seen that all the stochastic models give identical through levels, whereas the nonlinear irregular wave model shows significantly higher crest level.

In Figure 63, 64 and 65 the results of the different waves impact on the structural loads are seen for selected sensors. At the top left is seen the longitudinal tower bottom bending moment just above the transition piece, the axial force in the front right leg just below the top X-brace connection in the K-joint, the axial force in the lower X-brace on the front side and the axial force in the upper part of the right pile on the back side. The locations of the sensors is also shown in Figure 61 (right).

The load increase from the nonlinear waves is pronounced and seen to increase the load level for all the simulated wave cases. For the small significant wave height the increase in load level is likely to be caused by ”springing” where ”ringing” is seen for the large significant wave heights. It is however difficult to really identify whether it is ”springing” or ”ringing” that causes the high response for the nonlinear waves, which is illustrated in Figure 62, however it is clear that the structural response occurs when the wave is very steep. The increased load effect is seen for all sensors on the structure but is especially pronounced for the tower bottom bending load and the leg load in the upper part of the substructure. For the cases with small significant wave heights, the increased high frequency content in the nonlinear waves seem to cause a general small increase in loads, which fits very well with the springing affected loads. The mechanism is however different for the large significant waves where ringing occur. Here the single large waves in the irregular wave train is of a magnitude large enough to excite the structure and cause large transients after the wave passing. The excitation is mainly on the first structural frequency at 0.32Hz and due to the low amount of damping, the vibration levels become large. Since the turbine is at standstill and the blades are pitched 90°, the aerodynamic damping on the structure is minimal, and there is only contribution from damping originating from the structure, hydrodynamics and soil. In order to see the influence of damping levels, results was obtained for damping levels between 2 and 10% expressed a a log. decrement, see figures 63 to 65, which represent the expected range of efficient damping for a turbine mounted on a monopile. For all cases a significant increase in loads are seen for the nonlinear wave loads. The load increase could be to a an increased level of a factor of 2-3 compared to the approach using linear wave theory. This really indicate the importance of these nonlinear wave situations for sites where steep nonlinear waves occurs, as in the inner Danish waters.

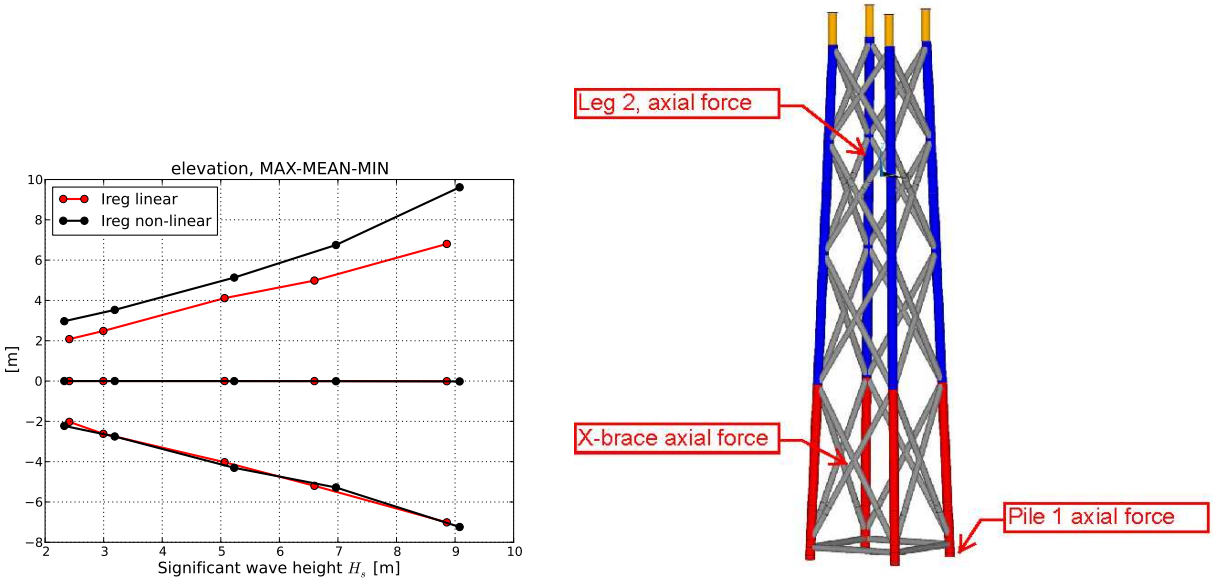


*Figure 61*: Left: An overview of the max and minimum wave elevation levels for the selected significant wave heights. Of obvious reasons the irregular wave have higher variation in the wave elevation than for a regular stream function wave. The nonlinear waves have same level of wave through whereas a significant increased wave crest level is seen. Right: Illustration of the selected load sensors, courtesy Vorpahl et al. (2011). Leg 2 is front right towards the incoming waves, where pile 1 is on the back side.

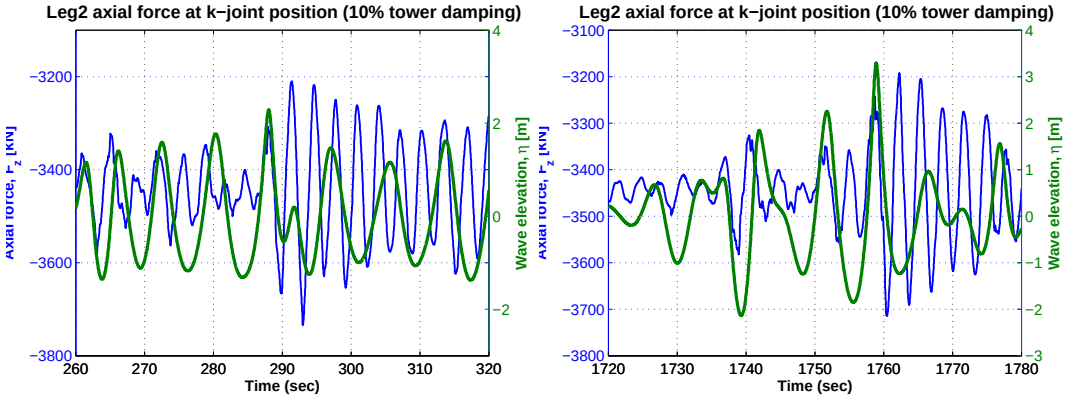


*Figure 62*: Different types of wave excitation on the structure.

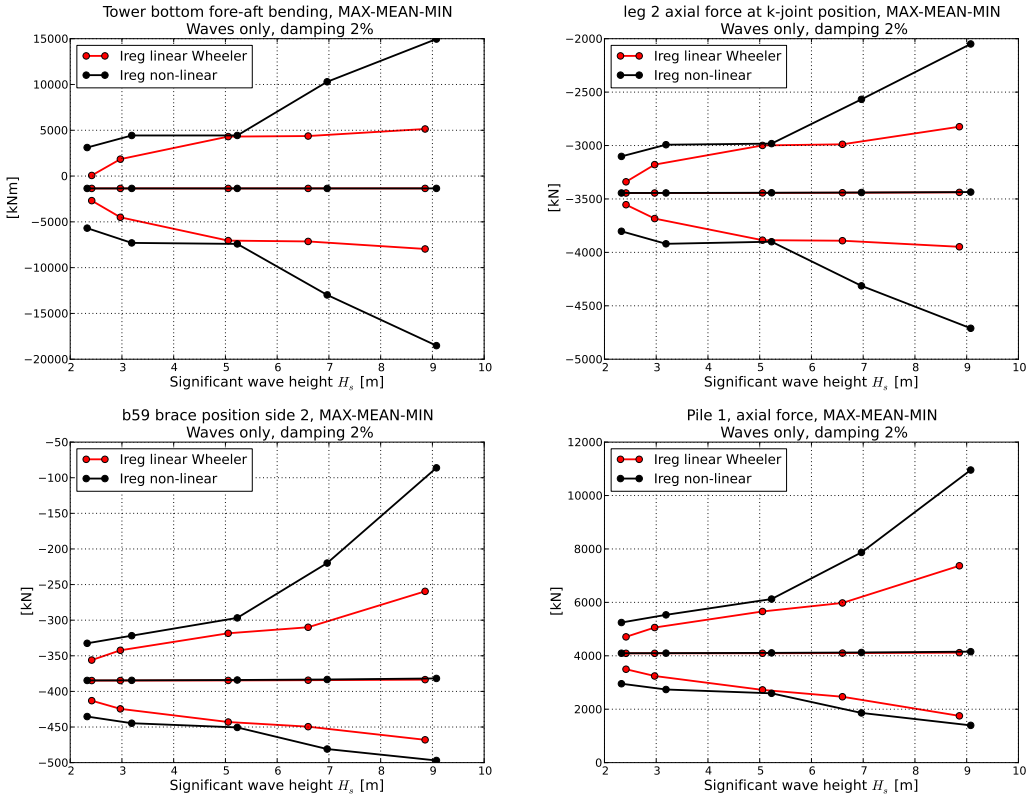


*Figure 63*: Results using a structural damping level of 2% log. decr. The simulated loads shown for tower bottom fore-after bending, axial forces in leg 2 below the K-joint, axial force in the lower X-brace and the axial force in pile 1. A clear increase in loads due to the full nonlinear loads is seen. Max-Mean-Min loads are shown.

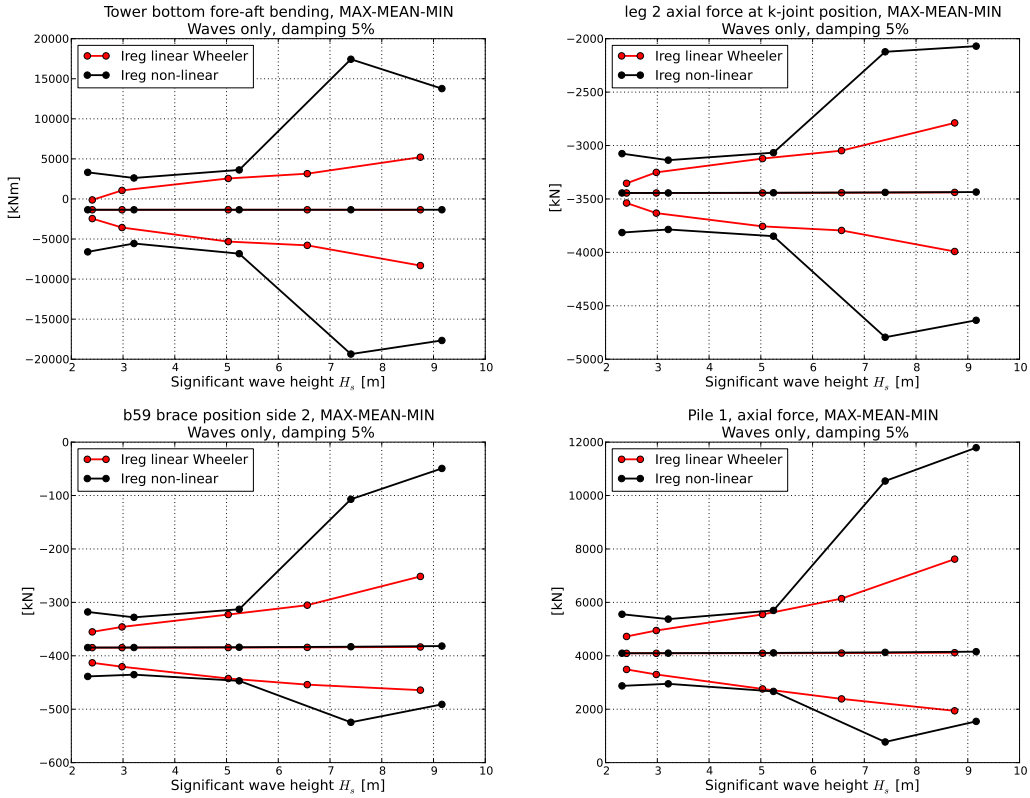


*Figure 64*: Results using a structural damping level of 5% log. decr. The simulated loads shown for tower bottom fore-after bending, axial forces in leg 2 below the K-joint, axial force in the lower X-brace and the axial force in pile 1. A clear increase in loads due to the full nonlinear loads is seen. Max-Mean-Min loads are shown.

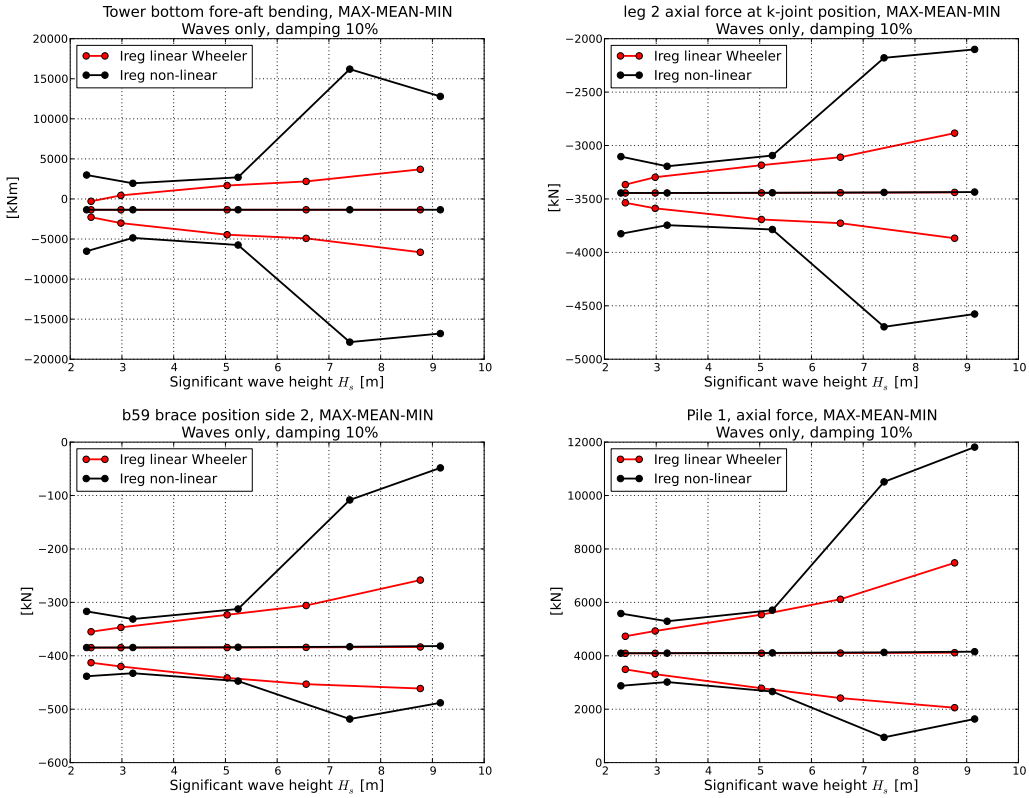


*Figure 65*: Results using a structural damping level of 10% log. decr. The simulated loads shown for tower bottom fore-after bending, axial forces in leg 2 below the K-joint, axial force in the lower X-brace and the axial force in pile 1. A clear increase in loads due to the full nonlinear loads is seen. Max-Mean-Min loads are shown.

## 5.6 Operation, wave from front

During operation the aerodynamic damping for the tower fore-after direction is significantly increased compared to the standstill situation. As there is also significant aerodynamic load contributions to the substructure, the overall impact of the wave loads and hereby also the wave kinematics model is expected to be less pronounced during operation than at standstill. A set of simulations during operation has been carried out to quantify the impact of the nonlinear wave kinematics for these situations. A wind speed ranging from 6.7m/s to 23.5m/s has been associated with the five wave cases shown in Table 12. The results are shown for the axial force in pile 1 and leg2 as 1Hz equivalent fatigue loads in Figure 66. The difference between linear and nonlinear wave modeling is smaller than for the standstill situation, however a difference of 10-20% are seen for all cases.

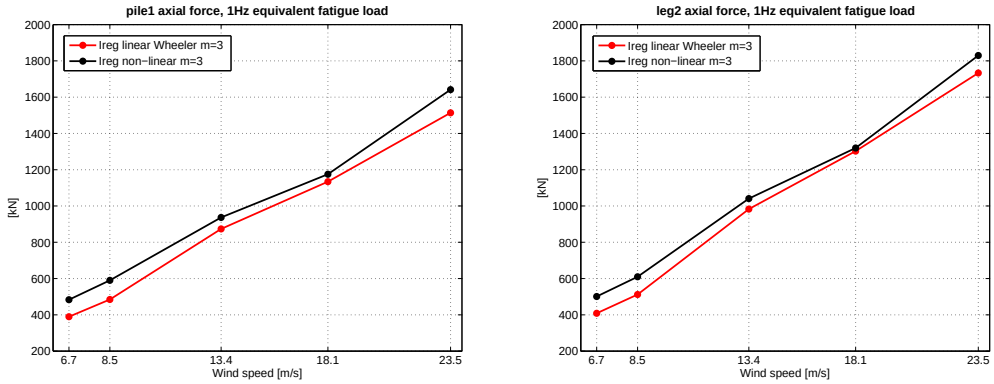


*Figure 66*: Comparison of 1Hz equivalent fatigue loads during operation. Wind and wave relation is given in table 12. A general difference in load level of 10-20% can be seen for all wind speeds

## 5.7 Operation, Sensitivity of wind-wave misalignment

As the aerodynamic damping of the tower modes are significantly higher for the fore-after direction than for the side-side mode there could be a different response if the wave direction is different than the wind direction. This has been investigated by changing the wave direction between 0° and -90° as illustrated in Figure 67. Results are shown in Figure 68 where it can be seen that the difference in general is in the order of 10-20% as for the no-misalignment cases, but the absolute fatigue load level of the different piles is sensitive to the load direction of waves.

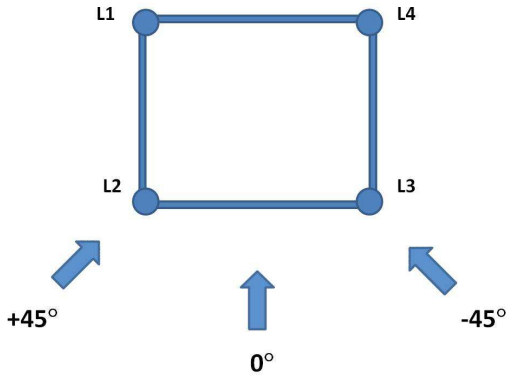


*Figure 67*: Illustration of the pile and leg numbering related to wind and wave direction.

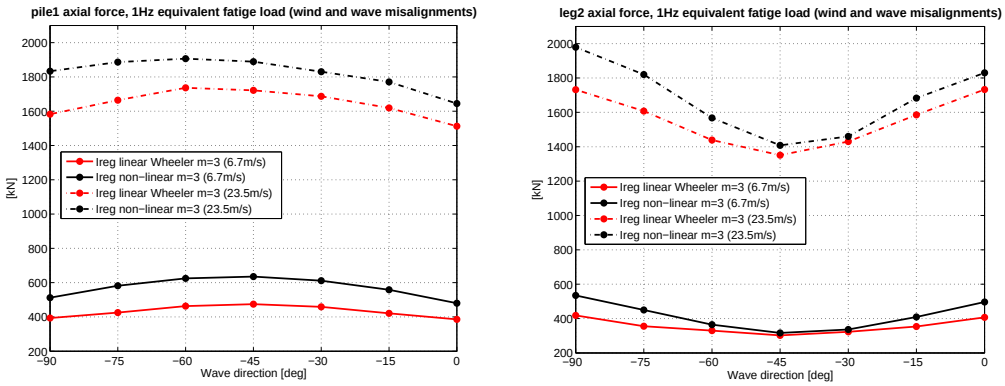


*Figure 68*: Comparison of 1Hz equivalent fatigue loads during operation and with wind-wave misalignment. Wind and wave relation is given in table 12. A general difference in load level of 15-20% can be seen for all wind speeds

## 5.8 Improvements of HAWC2

In order to improve the simulation speed attention was put on several parts:

1. Pre-generation the wave kinematics field for standard linear wavetrains.
2. Improvements of the solver including a consistent formulation of the added mass from the water.
3. Reduction of DOF's by applying a super element technique for the substructure.

### 5.8.1 Pre-generation of linear wave kinematics

In the basic generation of wave kinematics for wavetrains using simple linear Airy wave theory it involves a super position of solutions for single-frequency waves. A simple example is eg. the surface description of the wave elevation $\eta$

$$\eta_i(t,x,y) = A_i \sin(\omega_i t - k_i x \cos\theta_i - k_i y \sin\theta_i + \varphi_i) \tag{32}$$

including the notations for time $t$, frequency $\omega$, wave number $k$, wave head angle $\theta$ and location given by the coordinates in the main wave direction $x$ and lateral $y$. The final irregular wave surface is given by the summation of the contributions of the individual frequencies, denoted by index $i$.

$$\eta(t,x,y) = \sum_{i=1}^{N} \eta_i(t,x,y) \tag{33}$$

Typically the number of wave components used is as minimum equal to the number of seconds simulated, which for a typical 1 hour simulation is then higher than 3600. Another example, included here to illustrate the computational requirements, is the wave kinematics velocity which for a single frequency is a hyperbolic cosine expression

$$u_i(t,x,y,z) = \omega_i \frac{\cosh[k_i(z+z_0)]}{\sinh[k_i z_0]} A_i \sin(\omega_i t - k_i x \cos\theta_i - k_i y \sin\theta_i + \varphi_i)\cos(\theta_i) \tag{34}$$

which is superpositioned similarly to the wave elevation

$$u(t,x,y,z) = \sum_{i=1}^{N} u_i(t,x,y,z) \tag{35}$$

The most accurate numerical solution is obtained when the kinematics is calculated in the calculation point where the final hydrodynamic force is calculated. This is typically between 5 and 10 locations over a structural beam element which for a jacket structure adds up to several thousand locations. In the default wave kinematics module for HAWC2, the kinematics was evaluated at all locations in all time step, since it was originally applied for floating structures where the actual location of calculation point could vary significantly in time, or for monopile constructions with limited simulation points. For a jacket construction, this approach however was noticeably slowing down the simulation time.

In order to speed up the generation of wave kinematics, the approach was to pre-generate a field of wave kinematic solution a bit similar to how atmospheric turbulence is normally pre-generated in a cartesian grid structure. The solution for the many frequency components is evaluated in the grid points, and the solution could be interpolated using a simple linear scheme for any point in between. Since the velocity profile over the depth $u(z)$ is a rather continuous profile it seem to be sufficient with 7-10 evaluation points over the water depth which is way less than the requirement in resolution for the hydrodynamic calculation points. In order to handle the varying height of the water profile, a wheeler based relation between physical coordinates and relative coordinates was also used.

$$\hat{z} = \frac{z+z_0}{1+\frac{\eta(t)}{z_0}} \tag{36}$$

If the wave field is calculated either for a monopile construction or in case only 2D wave fields are used it is not necessary to evaluate more calculation points than for one lateral position $y$ which further reduces the number of evaluation points.

To some extent there must also exist a relation between the elevation as function of time and location in the wave direction $x$. For atmospheric turbulence this is known as the Taylors hypothesis Taylor (1937), and is based on the assumption that the large low frequent structures of turbulence does not change significantly over a limited distance. If this is also a reasonable assumption for hydrodynamic wave loading it is possible to also eliminate the physical dimension $x$ in the grid structure and only evaluate in the dimension for time $t$. A justification of this is that a 3 dimensional structure as a jacket only covers a very limited spatial distance compared to the individual wave lengths included for typical wave spectra. In order to ensure the right timing of when the wave meet the first part of the jacket construction until it leaves the last part it is important to have a sufficient relation between time and space for a wavetrain. The problem is that the wave velocity depends on the individual wave frequency, which means that long or short waves does not move with the same speed and wave modulation is highly present. The wave traveling velocity of the individual waves are denoted *phase velocity*, whereas the velocity of energy of a group of wave components is denoted *group velocity* (37). As the group velocity is also frequency dependent it was decided to used the wave number associated with the frequency of the peak period $T_p$ from the input spectre. In this project, it was found that the phase velocity based on the wave number for the frequency with most energy content results in a fine agreement between an fully updated and a grid based solution for wave trains generated by a jonswap spectrum. This is illustrated in figure 69, where a good agreement in the timing of load peaks is seen. The absolute magnitude differs slightly, which is directly caused by the modulation of waves. If this should be improved, the approach of a simple grid structure could be replaced by an approach where the wave kinematic evaluation points depend on the topology of the structure instead. The group velocity used is from the relation

$$c_G = \frac{1}{2}\sqrt{\frac{g}{k}}\left[\frac{kh + \tan(kh) - kh\tanh^2(kh)}{\sqrt{\tanh(kh)}}\right] \tag{37}$$

and the phase velocity is

$$c_{ph} = \sqrt{\frac{g}{k}\tanh(kh)} \tag{38}$$

where g is the gravity acceleration, h is the water depth and k the wave number.

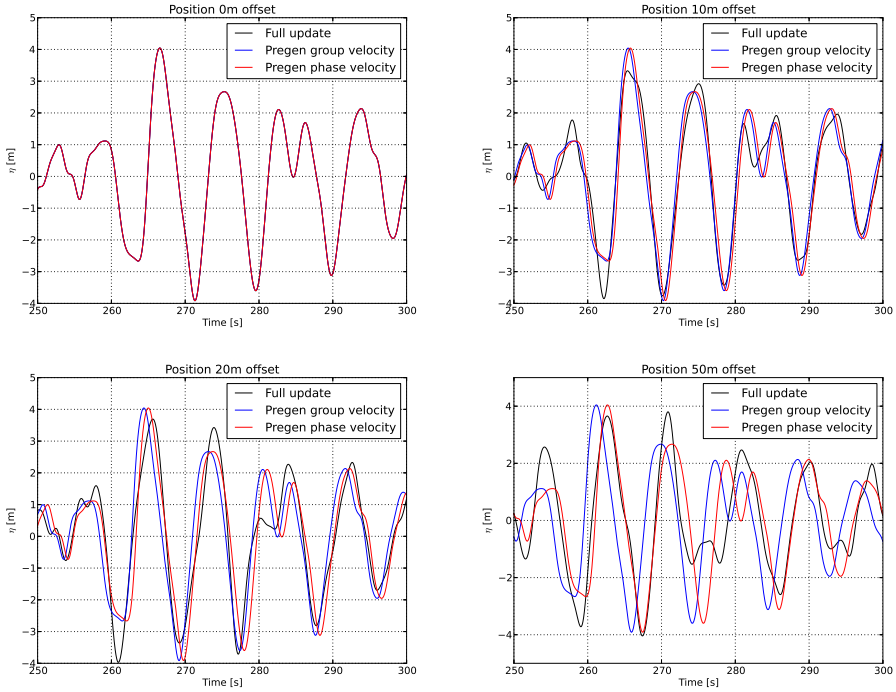


*Figure 69*: Comparison of fully updated solution and the faster grid based solution using either wave phase or group velocity for offset distances of 0, 10, 20 and 50m. A perfect match is seen for an offset distance of 0 m (as expected). For increasing distances the match is no longer perfect, but the timing of the peaks does match, indicating a good approach using the suggested method. For small offset distances up to 20m, the difference in timing between using phase or group velocity is very small and it is hard to see which approach is preferable. For larger offset distances the phase velocity approach show best agreement in the timing.

### 5.8.2 Consistent handling of added mass in the HAWC2 solver

As default any external force applied to the structure in HAWC2 is included on the right-hand side of the equations as illustrated in (39). This is normally a very fine approach for aerodynamic forces, since these mainly depend on the structural velocity and therefore induce a kind of damping (positive or negative) which is normally well handled by the Newmark solution scheme in combination with a Newton-Raphson iteration approach for each time step.

$$\mathbf{M}\ddot{\mathbf{x}} + \mathbf{C}\dot{\mathbf{x}} + \mathbf{K}\mathbf{x} = \mathbf{F}(t) \tag{39}$$

In case of hydrodynamic forces being applied to the structure, a significant added mass is however introduced. This immediately cause a significant increase in number of iterations within each time step and in some cases a lack of convergence also occurred. First attempt to include the effect of added mass was to apply a numeric way to establish and added mass matrix based on small variations of the structural degrees of freedom and evaluate the feedback forces from the hydrodynamics. It did improve on the numerical convergence and reduced the number of iterations within each time step, but still up to 10-20 iterations occured, which for a already time consuming simulation of a jacket resulted in very slow performance and also caused iteration failures from time to time. It was therefore decided to do it the right way, which is similarly to how the effects of inertia of the general structure is handled. In this way it was possible to avoid any extra iterations caused by added mass of the water and eliminated the convergence failures previously seen.
In the multibody formulation of HAWC2 the floating frame of reference method is used, which means that any point on the structure is described by a set of large rotations/movements of the body it is attached to, and local deformations of the body it self. This is expressed

$$\mathbf{u} = \mathbf{R} + \mathbf{A}(\mathbf{r}_c + \mathbf{N}_c\mathbf{q}) \tag{40}$$

where $\mathbf{R}$ is the location of the origo of the body, $\mathbf{A}$ is a transformation matrix expressing the orientation of the body, $\mathbf{r}_c$ is a vector from the body origo to the initial non-displaced location of the observed point, $\mathbf{N}$ is the shape functions of the element to which the point is connected and $\mathbf{q}$ is the states of the element nodes.
In order to evaluate the added mass, the associated acceleration of a point on the structure is found by a double integration of (40) with respect to time.

$$\ddot{\mathbf{u}} = \ddot{\mathbf{R}} - \mathbf{A}[\{\mathbf{r}_c\}\times\mathbf{I}]\dot{\tilde{\boldsymbol{\omega}}} + \mathbf{A}\mathbf{N}_c\ddot{\mathbf{q}} \tag{41}$$

The added mass is evaluated, where the contribution in local section coordinates is assembled to a 3x3 matrix $\mathbf{C_M}$. Since the acceleration found in 41 is in global coordinates some coordinate transformation involving $\mathbf{A}$ is needed.

$$\mathbf{Q} = -\mathbf{A}\mathbf{T_{AS}}\mathbf{C_M}\mathbf{T_{AS}}^T\mathbf{A}^T\ddot{\mathbf{u}} \tag{42}$$

Finally, the added mass matrix for the body is found by integrating the hydrodynamic force components, post-multiplied by the transpose of the virtual displacement vector, over the entire body, so

$$\mathbf{M_A} = \int_L \begin{bmatrix} \mathbf{A}\mathbf{C_M^S}\mathbf{A}^T & \mathbf{A}\mathbf{C_M^S}[\{\mathbf{r_c}\}\times\mathbf{I}] & \mathbf{A}\mathbf{C_M^S}\mathbf{N_c} \\ & -[\{\mathbf{r_c}\}\times\mathbf{I}]\mathbf{C_M^S}[\{\mathbf{r_c}\}\times\mathbf{I}] & [\{\mathbf{r_c}\}\times\mathbf{I}]\mathbf{C_M^S}\mathbf{N_c} \\ \textit{sym} & & \mathbf{N_c}^T\mathbf{C_M^S}\mathbf{N_c} \end{bmatrix} dz \tag{43}$$

where $\mathbf{C_M^S} = \mathbf{T_{AS}}\mathbf{C_M}\mathbf{T_{AS}}^T$. Since $\mathbf{A}$ is part of the added mass matrix and $\mathbf{A}$ is time dependent, the added mass matrix also becomes time dependent, however, $\mathbf{A}$ is the *only* time dependent part of the matrix. This means that the added mass matrix have to be updated each time step, but only by pre- and post multiplication by $\mathbf{A}$ - the remainder of the matrix is integrated only once.

### 5.8.3 Superelement formulation

With jacket constructions and other complex structures involving many degrees of freedom (DOF), it is important to ensure reasonable simulation performance with respect to CPU time consumption. In the normal general structural formulation HAWC2 a body typically consist of a number of beam element interconnected by nodes each having six DOF. For a full jacket foundation, this is so far modeled as a connection of bodies using constraint equations in a multibody approach as described below. Such a jacket typically consist of 4 bodies with minimum 10 elements (each corner pile) and 32 bodies with a minimum of 2 elements for the X-braces. On top of this, a number of bodies are used to represent the pile connection to the soil as well as the transfer piece for the tower connection. In total a minimum number of 700DOF's is not unusual for this foundation type.

It is clear that the simulation time used for a simulation is highly sensitive to the number of DOF's and any method for speeding up the simulation is welcome if the solution accuracy is not significantly affected.

The full HAWC2 EOMs are as described in Kim et al. (2013):

$$\mathbf{M}\ddot{\mathbf{q}} + \mathbf{C}\dot{\mathbf{q}} + \mathbf{K}\mathbf{q} + \nabla\mathbf{g}^T\lambda - \mathbf{F} = \mathbf{0} \tag{44}$$

$$\mathbf{g} = \mathbf{0} \tag{45}$$

where $\mathbf{M}$,$\mathbf{C}$ and $\mathbf{K}$ are the mass, damping and stiffness matrices of the unconstrained system. $\mathbf{g}$ is the algebraic constraint equations and $\nabla\mathbf{g}^T\lambda$ express the fictitious forces required to fulfill the constraint equation $\mathbf{g} = \mathbf{0}$. The linearized EOM valid for the small deflections $\delta\mathbf{q}$

$$\mathbf{M}_\mathbf{l}\ddot{\delta\mathbf{q}} + \mathbf{C}_\mathbf{l}\dot{\delta\mathbf{q}} + \mathbf{K}_\mathbf{l}\delta\mathbf{q} + \nabla\mathbf{g}^T\delta\lambda - \delta\mathbf{F} = \mathbf{0} \tag{46}$$

$$\nabla\mathbf{g}\,\delta\mathbf{q} = \mathbf{0} \tag{47}$$

Since a constraint equation involves multiple states, eg. a constraint that enforce motion of one node on a body to be identical to the motion of another node, there are constraint equation, which are linearly dependent on other constraint equations. The first step in the reduction is therefore to solve the linearised constraint equations in (47) for a subset, $\delta\mathbf{q}_1$, of all the states, $\delta\mathbf{q}$. The number of states in $\delta\mathbf{q}_1$ corresponds to the number of constraint equations and can subsequently be expressed as a function of the complementary subset, $\delta\mathbf{q}_2$, like this:

$$\nabla\mathbf{g}\,\delta\mathbf{q} = \begin{bmatrix} \mathbf{G_1} & \mathbf{G_2} \end{bmatrix} \begin{bmatrix} \delta\mathbf{q}_1 \\ \delta\mathbf{q}_2 \end{bmatrix} = \mathbf{0} \tag{48}$$

$$\tag{49}$$

A reduction can be performed by solving the constraint part (It is assumed that the state vector is ordered so that G1 below is invertible):

$$\nabla\mathbf{g}\,\delta\mathbf{q} = \begin{bmatrix} \mathbf{G_1} & \mathbf{G_2} \end{bmatrix} \begin{bmatrix} \delta\mathbf{q}_1 \\ \delta\mathbf{q}_2 \end{bmatrix} = \mathbf{0} \tag{50}$$

$$\Downarrow$$

$$\delta\mathbf{q}_1 = -\mathbf{G_1}^{-1}\mathbf{G_2}\,\delta\mathbf{q}_2 \tag{51}$$

Hence,

$$\delta\mathbf{q} = \begin{bmatrix} \delta\mathbf{q}_1 \\ \delta\mathbf{q}_2 \end{bmatrix} = \begin{bmatrix} -\mathbf{G_1}^{-1}\mathbf{G_2} \\ \mathbf{I} \end{bmatrix} \delta\mathbf{q}_2 \equiv \mathbf{T_G}\delta\mathbf{q}_2 \tag{52}$$

By inserting 52 in 46 and pre-multiplication by the transpose of $\mathbf{T_G}$, a reduced set of ordinary 2nd order EOMs is achieved:

$$\left(\mathbf{T_G}^T\mathbf{M_l}\mathbf{T_G}\right)\delta\ddot{\mathbf{q}}_2+\left(\mathbf{T_G}^T\mathbf{C_l}\mathbf{T_G}\right)\delta\dot{\mathbf{q}}_2+\left(\mathbf{T_G}^T\mathbf{K_l}\mathbf{T_G}\right)\delta\mathbf{q}_2-\mathbf{T_G}^T\delta\mathbf{F}=\mathbf{0} \tag{53}$$

This reduced the original number of equations in (44) roughly by a factor of 2.

In the continued search for faster simulation it has been investigated how the EOM's can be reduced for the multibody system of DOF's by reduction using mode shape selection. The shapes that should be chosen will depend on the structure; It is in principle possible to select between static shapes obtained as static solutions to unit forces applied to the structure in selected nodes or dynamic mode shapes obtained from the eigenvalue problem in (53) ($\delta\mathbf{F}=\mathbf{0}$). The reduced state vector, $\delta\mathbf{q}_2$, is assumed to be composed of a linear combination of the chosen shapes:

$$\delta\mathbf{q}_2=\mathbf{T}_\phi\alpha \tag{54}$$

where the columns of $\mathbf{T}_\phi$ are composed of the selected reduction shapes and $\alpha$ is a vector that contains the new generalized state variables. In order to be able to interface the super element to other structures we need some "physical" DOFs to couple to. If we assume that these "physical" interface DOFs are located at the top of the reduced state vector $\delta\mathbf{q}_{21}$ and the other internal states are located in $\delta\mathbf{q}_{22}$, we can substitute those by the same number of generalized states in $\alpha$:

$$\delta\mathbf{q}_2=\begin{bmatrix}\delta\mathbf{q}_{21}\\ \delta\mathbf{q}_{22}\end{bmatrix}=\begin{bmatrix}\mathbf{T}_{\phi 11} & \mathbf{T}_{\phi 12}\\ \mathbf{T}_{\phi 21} & \mathbf{T}_{\phi 22}\end{bmatrix}\begin{bmatrix}\alpha_1\\ \alpha_2\end{bmatrix} \tag{55}$$

The upper part of the system in (55) is used to find $\alpha_1$ and inserting it back, the final transformation matrix and combined interface and physical DOFs are obtained as:

$$\delta\mathbf{q}_2 = \begin{bmatrix}\mathbf{I} & \mathbf{0}\\ \mathbf{T}_{\phi 21}\mathbf{T}_{\phi 11}^{-1} & \mathbf{T}_{\phi 22}-\mathbf{T}_{\phi 21}\mathbf{T}_{\phi 11}^{-1}\mathbf{T}_{\phi 12}\end{bmatrix}\begin{bmatrix}\delta\mathbf{q}_{21}\\ \alpha_2\end{bmatrix} \tag{56}$$

$$\equiv \mathbf{T}_\alpha\begin{bmatrix}\delta\mathbf{q}_{21}\\ \alpha_2\end{bmatrix}\equiv\mathbf{T}_\alpha\mathbf{q_r} \tag{57}$$

where $\mathbf{q_r}$ is the final reduced set of DOFs, where the upper part $\delta\mathbf{q}_{21}$ is the coupling nodes in physical coordinates and the lower part $\alpha_2$ is the generalized coordinates.

The total transformation is now given by:

$$\delta\mathbf{q}=\mathbf{T_G}\mathbf{T}_\alpha\mathbf{q_r}\equiv\mathbf{T}\mathbf{q_r} \tag{58}$$

and by inserting 58 in 46 and pre-multiplication by the transpose of $\mathbf{T}$ which equals $\mathbf{T_G}\mathbf{T}_\alpha$, the final reduced set of ordinary 2nd order EOMs is achieved:

$$\left(\mathbf{T}^T\mathbf{M_l}\mathbf{T}\right)\ddot{\mathbf{q}}_\mathbf{r}+\left(\mathbf{T}^T\mathbf{C_l}\mathbf{T}\right)\dot{\mathbf{q}}_\mathbf{r}+\left(\mathbf{T}^T\mathbf{K_l}\mathbf{T}\right)\mathbf{q_r}-\mathbf{T}^T\delta\mathbf{F}=\mathbf{0} \tag{59}$$

The part that can improve the simulation time significantly is that it is possible to limit the number of states in $\mathbf{q}_r$ to perhaps the lowest 20 modes instead of operating with the original 700DOF+.

In order to demonstrate the performance of the super element approach an example is shown below. This was originally presented at EWEA offshore conference in 2013 (Hansen et al.

(2013)) Here a full HAWC2 model of a jacket was condensed to a super element based on 6 static deflection shapes from pertubations of the interface node between the jacket and turbine. The super element results was compared to a full HAWC2 solution as well as a sequential solution. In the sequential solution, the turbine was modeled without the jacket, but with a soft element ensuring a correct 1st eigenfrequency of the tower. The cross sectional forces and moment in the interface node was then in a separate postprocessing applied to a static jacket model. Wave loads are also added to the jacket in postprocessing phase for the sequential approach. In figure 70 a comparison of cross sectional loads are seen in the interface node, where a very good match is seen between the three solutions. A comparison is also shown for the axial force in one of the piles in figure 71 where the agreement also fine, but a different load level is however seen at 1.2Hz corresponding to the 2nd tower bending mode. This difference may be due to the limited number of reduced shapes not including the higher order modes. It was however tried to use dynamic mode shapes for the jacket alone, but that did not improve the results compared to the static derived deflection shapes. It may also very well be, that the correct eigenmodes to be used is the jacket modes, but extracted as part of global mode shapes for the entire turbine. This still requires some effort before being finally solved.

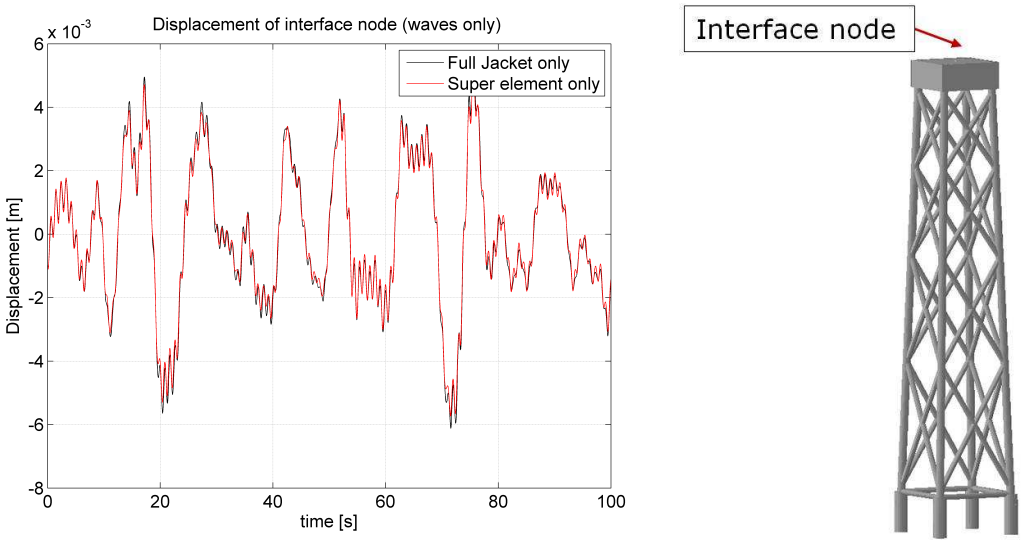


*Figure 70*: Comparison of loads at interface node between tower and jacket. A very fine agreement is seen between the original full DOF solution and the super element approach.

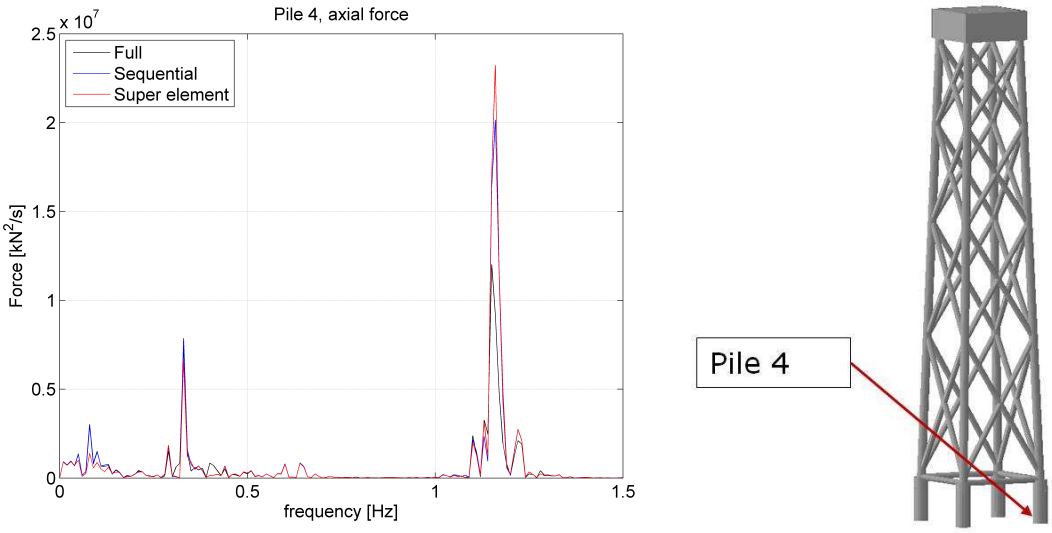


*Figure 71*: Comparison of a loadspectrum at one of the support piles. A good agreement is seen between the original full DOF solution and the super element approach, however the response deviates for the higher order modes for the sequential and super element approach. .

## 5.9 Suggestions for further work

The present investigations and developments provides insight into wave load effects on jacket structures. Further, the developments in HAWC2 enables detailed, studies of the aero-elastic behaviour with improved efficiency. Suggestions for further work to advance these fields are

- Validation of the jacket wave load models against laboratory data
- Validation of the jacket response against full-scale data
- Extended response investigations with a wider set of wave conditions
- Further development of the super-element method, including the selection of deflection shapes

# 6 Task D: Physical model tests

**Henrik Bredmose (DTU Wind Energy)**
with contributions from Flemming Schlütter, Anders Wedel Nielsen, Hans Fabricius Hansen and Jacob Tornfeldt Sørensen

## 6.1 Introduction

Physical model tests were carried out at DHI to 1) provide validation data for the numerical models developed and 2) to enable direct quantification of wave load distributions and the effect of various wave parameters. The tests were made with vertical circular cylinders in two scales: 1) at scale 1:36.6 with a rigid cylinder and 2) at scale 1:80 with a rigid and a flexible cylinder. The flexible cylinder was designed such that its first two natural frequencies matched those of the NREL 5MW monopile reference wind turbine Jonkman et al. (2009). This allowed for a direct study of wave-driven excitation of structural vibration, also known as springing, ringing or impulsive excitation, depending on the wave type that causes it.

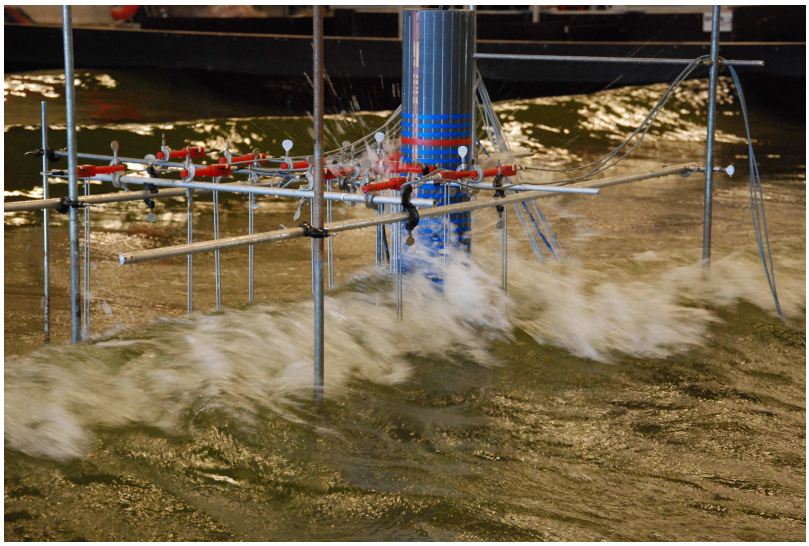

*Figure 72*: Breaking wave impact at scale 1:36.6.

### 6.1.1 Main achievements

The main achievements of the experimental work are

- Establishment of an all-round data set for wave forces on monopile cylinders, that covers a wide range of regular and irregular 2D and 3D wave conditions
- Measurements of the structural response for a flexible cylinder, including ringing-type responses
- Successful numerical reproduction of the measurements with a CFD solver and a combined fluid-structure approach based on a potential flow wave model and a finite element solver

The experiments, the setup and the measurement equipment has been reported in the technical report of Schlütter (2013). The experiments, their analysis and comparison to numerical models

have further been reported in journal papers of Paulsen, Bredmose & Bingham (2013), Choi et al. (2013), four conference proceedings papers (Hansen et al. 2012, Nielsen et al. 2012, Bredmose et al. 2013, Paulsen, Bredmose, Bingham & Schløer 2013), the PhD theses of Paulsen (2013) and Schløer (2013), the MSc project of Slabiak & Sahlberg-Nielsen (2013) and the BSc project of Nielsen & Dam (2012).

### 6.1.2 Limitations

The data set is subject to two limitations which must be taken into account in its analysis:

- **Slope.** The slope of 1:25 is not realistic as natural slopes are usually much smaller, e.g. 1:1000. This is likely to change the wave conditions towards more plunging-type breaking, especially at the smaller depths. While this does not prevent validation of the numerical models, the analysis of the data for design purposes may be affected by the steep slope. A less steep slope requires more space in the laboratory. Alternatively, the scale can be reduced or the depth at the wave maker can be reduced. While the first option is not feasible in the wave basin, the two others are undesirable, as they induce reduced measurement accuracy and increases the limitations of first-order wave theory for the wave generation.
- **Vibrations.** Although the rigid structures were built to be stiff, the measurement system for forces involves some flexibility which in turn introduces a natural frequency in the system. For the rigid structure at scale 1:36.6, this frequency was approximately 9 Hz while at 1:80, the stiff cylinder had a couple of natural frequencies, the lowest at approximately 7 Hz. Although this is far from the fundamental wave frequency range, steep waves were able to excite it. This introduces dynamic loads in the measured force signal which can affect the measured peak force value and the subsequent force variation. The effect can be thought of as un-intended ringing of the structure and can to some extent be eliminated by filtering in the frequency domain. This, however, may also remove parts of the 'true' force signal and thus leaves an uncertainty on the peak forces in some of the test series.

## 6.2 Test setup and parameter space

A detailed description of the experiments and setup is provided by Schlütter (2013). A resumé is given in the following. The tests were carried out in DHI's shallow water basin with a fixed bathymetry. This is shown in figure 73 and consisted of a slope of 1:25 that started 1 m from the wave maker and stretched 9 m horizontally to a flat plateau. The cylinder was placed 7.75 m from the wave maker at the slope, or in some tests at the plateau.

The instrumentation consisted of 21 wave gauges, a 3-component force transducer mounted at the bottom of the cylinder, a Vectrino velocity-meter placed in front of the cylinder. The 1:36.6 scale cylinder had a diameter of 16.4 cm and was equipped with 5 pressure transducers, flush with the cylinder wall. The 1:80 scale flexible cylinder was constructed from a 7.5 cm standard PVC pipe with a wall thickness of 1.8 mm. A photo of both structures is shown in figure 74.

The main dimensions of the flexible structure are listed in table 13. Two point masses of approximately 1.8 kg were mounted on it to ensure the right natural frequencies. The pipe was instrumented with five accelerometers, mounted inside the structure. Further, the displacement of the pipe in the inline and transverse direction were measured at the same level as the uppermost accelerometer.

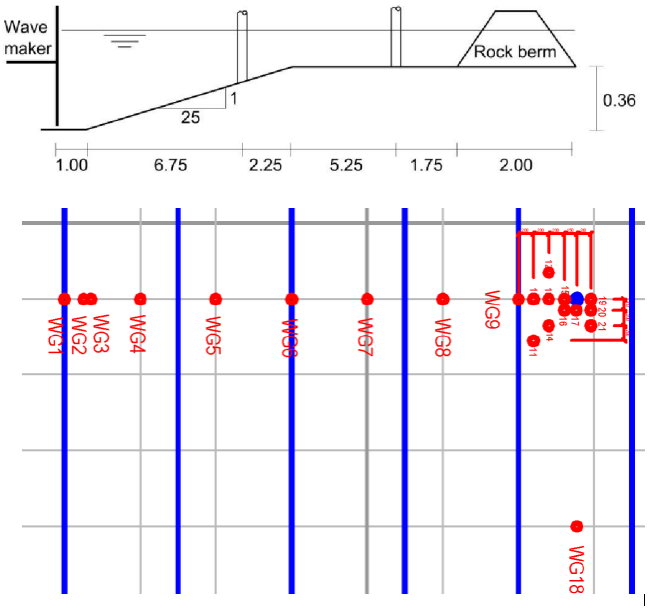


*Figure 73*: Top: Layout of the wave basin. Bottom: Placement of the wave gauges. Wave gauge 9–21 were relocated with the model when it was moved to the position at the plateau.

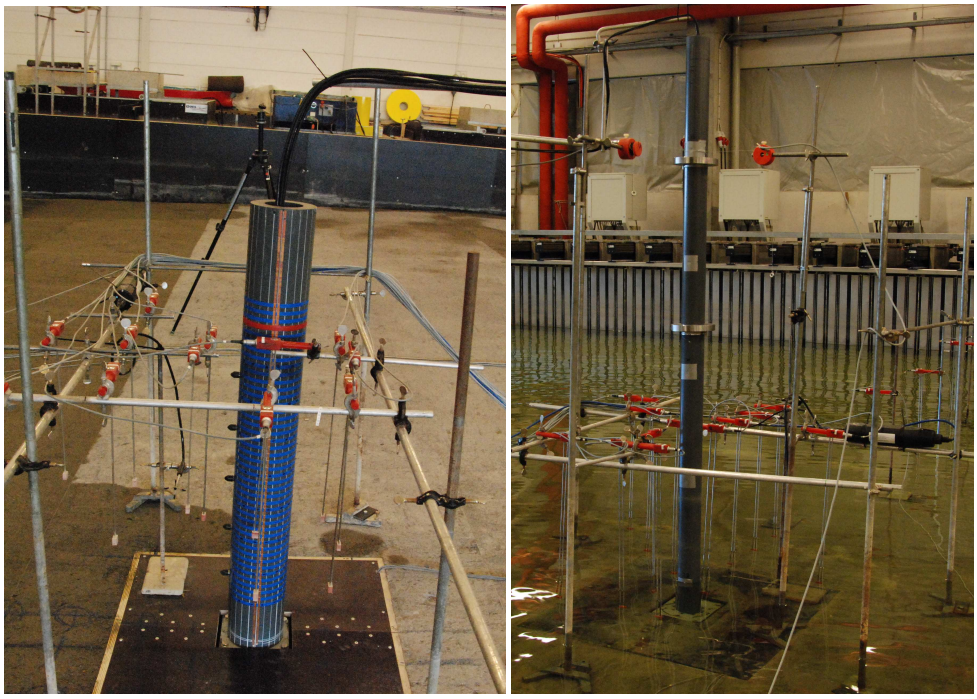

*Figure 74*: Left: The 1:36.6 scale rigid cylinder. The pressure sensor caps can be seen protruding from the cylinder. Right: The 1:80 scale flexible cylinder.

### 6.2.1 Test matrix

The test matrix covered 2D regular waves and 2D/3D irregular waves. For the rigid cylinder at scale 1:36.6, tests were made for two depths at the slope and one depth at the plateau. Further, tests with secondary structures and reference tests with measurement of the waves without the structure were carried out. The 1:80 tests comprised 3 depths at the slope. All tests were

| | Lab scale (1:80) | Prototype scale |
|---|---|---|
| $D_{\text{outer}}$ | 7.5 cm | 6.0 m |
| Wall thickness | 1.8 mm | 0.144 m |
| EI (estimated) | 1026 $\text{Nm}^2$ | $4.20 \cdot 10^{10}$ $\text{Nm}^2$ |
| $\zeta$ (estimated) | 0.017 | 0.017 |
| Density | 0.64 kg/m | $4.20 \cdot 10^3$kg/m |
| height | 200 cm | 160 m |
| $m_1$ | 1.786 kg | $937 \cdot 10^3$kg |
| $m_2$ | 1.784 kg | $936 \cdot 10^3$kg |
| $h_1$ | 160.75 cm | 128.6 m |
| $h_2$ | 108.75 cm | 87.0 m |
| $f_1$ | 2.5 Hz | 0.28 Hz |
| $f_2$ | 18 Hz | 2.0 Hz |
| $f_3$ | 50 Hz | 5.6 Hz |

*Table 13*: Data for flexible pipe. Prototype values are indicated just for reference.

carried out with both the flexible structure and a rigid structure to enable direct comparison of the results. The full test matrix is shown in table 14 and 15.

| No | File | Wave type | Water Depth at Wave maker | WL Lab | Spectrum | Target Wave height Hm0,t | Period / Peak Period Tp | Duration | Wave direction | Wave spreading | Placement | Model |
|---|---|---|---|---|---|---|---|---|---|---|---|---|
| - | name | | (m) | (cm) | | (m) | (s) | (hr) | (deg) | (-) | | |
| 1 | T00050609.dfs0 | Regular | 30 | 82 | - | 5.5 | 14 | 1 | 90 | 1 | slope | 36.6-stiff |
| 2 | T00060609.dfs0 | Regular | 30 | 82 | - | 8 | 14 | 1 | 90 | 1 | slope | 36.6-stiff |
| 3 | T00070609.dfs0 | Regular | 30 | 82 | - | 11 | 14 | 1 | 90 | 1 | slope | 36.6-stiff |
| 4 | T00080609.dfs0 | Regular | 30 | 82 | - | 11 | 10.2 | 1 | 90 | 1 | slope | 36.6-stiff |
| 5 | T00090609.dfs0 | 2D | 30 | 82 | JONSWAP | 4.3 | 10.2 | 3 | 90 | 1 | slope | 36.6-stiff |
| 6 | T00100609.dfs0 | 2D | 30 | 82 | JONSWAP | 6 | 10.7 | 3 | 90 | 1 | slope | 36.6-stiff |
| 7 | T00110609.dfs0 | 2D | 30 | 82 | JONSWAP | 8.3 | 10.2 | 3 | 90 | 1 | slope | 36.6-stiff |
| 8 | T00120609.dfs0 | 2D | 30 | 82 | JONSWAP | 8.3 | 12.6 | 24 | 90 | 1 | slope | 36.6-stiff |
| 9 | T00130609.dfs0 | 3D | 30 | 82 | JONSWAP | 4.3 | 10.2 | 3 | 90 | 12.5 | slope | 36.6-stiff |
| 10 | T00140609.dfs0 | 3D | 30 | 82 | JONSWAP | 6 | 10.7 | 3 | 90 | 12.5 | slope | 36.6-stiff |
| 11 | T00150609.dfs0 | 3D | 30 | 82 | JONSWAP | 7 | 11.6 | 3 | 90 | 12.5 | slope | 36.6-stiff |
| 12 | T00160609.dfs0 | 3D | 30 | 82 | JONSWAP | 8.3 | 12.6 | 3 | 90 | 12.5 | slope | 36.6-stiff |
| 13 | T00170609.dfs0 | Regular | 27.07 | 74 | - | 5.5 | 14 | 1 | 90 | 1 | slope | 36.6-stiff |
| 14 | T00180609.dfs0 | Regular | 27.07 | 74 | - | 11 | 14 | 1 | 90 | 1 | slope | 36.6-stiff |
| 15 | T00190609.dfs0 | 2D | 27.07 | 74 | JONSWAP | 4.3 | 10.2 | 3 | 90 | 1 | slope | 36.6-stiff |
| 16 | T00200609.dfs0 | 2D | 27.07 | 74 | JONSWAP | 6 | 10.7 | 3 | 90 | 1 | slope | 36.6-stiff |
| 17 | T00210609.dfs0 | 2D | 27.07 | 74 | JONSWAP | 8.3 | 10.2 | 3 | 90 | 1 | slope | 36.6-stiff |
| 18 | T00220609.dfs0 | 3D | 27.07 | 74 | JONSWAP | 4.3 | 10.2 | 3 | 90 | 12.5 | slope | 36.6-stiff |
| 19 | T00230609.dfs0 | 3D | 27.07 | 74 | JONSWAP | 6 | 10.7 | 3 | 90 | 12.5 | slope | 36.6-stiff |
| 20 | T00240609.dfs0 | 3D | 27.07 | 74 | JONSWAP | 8.3 | 12.6 | 3 | 90 | 12.5 | slope | 36.6-stiff |
| 21 | T00250609.dfs0 | Regular | 30 | 82 | - | 5.5 | 14 | 1 | 90 | 1 | slope | 36.6-stiff |
| 22 | T00260609.dfs0 | Regular | 30 | 82 | - | 8 | 14 | 1 | 90 | 1 | slope | 36.6-stiff |
| 23 | T00270609.dfs0 | Regular | 30 | 82 | - | 11 | 14 | 1 | 90 | 1 | slope | 36.6-stiff |
| 24 | T00280609.dfs0 | 2D | 30 | 82 | JONSWAP | 4.3 | 10.2 | 3 | 90 | 1 | slope | 36.6-stiff |
| 25 | T00290609.dfs0 | 2D | 30 | 82 | JONSWAP | 8.3 | 10.2 | 3 | 90 | 1 | slope | 36.6-stiff |
| 26 | T00300609.dfs0 | 3D | 30 | 82 | JONSWAP | 4.3 | 10.2 | 3 | 90 | 12.5 | slope | 36.6-stiff |
| 27 | T00310609.dfs0 | 3D | 30 | 82 | JONSWAP | 8.3 | 12.6 | 3 | 90 | 12.5 | slope | 36.6-stiff |
| 28 | T00320609.dfs0 | Regular | 27.07 | 74 | - | 11 | 14 | 1 | 90 | 1 | slope | 36.6-stiff |
| 29 | T00330609.dfs0 | 2D | 27.07 | 74 | JONSWAP | 6 | 10.7 | 3 | 90 | 1 | slope | 36.6-stiff |
| 30 | T00340609.dfs0 | 2D | 27.07 | 74 | JONSWAP | 8.3 | 10.2 | 3 | 90 | 1 | slope | 36.6-stiff |
| 31 | T00350609.dfs0 | 3D | 27.07 | 74 | JONSWAP | 8.3 | 12.6 | 3 | 90 | 12.5 | slope | 36.6-stiff |
| 32 | T00371den Model.dfs0 | Regular | 30 | 82 | - | 5.5 | 14 | 1 | 90 | 1 | slope/no struc | 36.6 |
| 33 | T00381den Model.dfs0 | Regular | 30 | 82 | - | 11 | 14 | 1 | 90 | 1 | slope/no struc | 36.6 |
| 34 | T00391den Model.dfs0 | 2D | 30 | 82 | JONSWAP | 4.3 | 10.2 | 3 | 90 | 1 | slope/no struc | 36.6 |
| 35 | T00401den Model.dfs0 | 2D | 30 | 82 | JONSWAP | 8.3 | 10.2 | 3 | 90 | 1 | slope/no struc | 36.6 |
| 36 | T00411den Model.dfs0 | 3D | 30 | 82 | JONSWAP | 4.3 | 10.2 | 3 | 90 | 12.5 | slope/no struc | 36.6 |
| 37 | T00421den Model.dfs0 | 3D | 30 | 82 | JONSWAP | 8.3 | 12.6 | 3 | 90 | 12.5 | slope/no struc | 36.6 |
| 38 | T00431den Model.dfs0 | Regular | 27.07 | 74 | - | 11 | 14 | 1 | 90 | 1 | slope/no struc | 36.6 |
| 39 | T00441den Model.dfs0 | 2D | 27.07 | 74 | JONSWAP | 8.3 | 10.2 | 3 | 90 | 1 | slope/no struc | 36.6 |
| 40 | T00451den Model.dfs0 | 3D | 27.07 | 74 | JONSWAP | 8.3 | 12.6 | 3 | 90 | 12.5 | slope/no struc | 36.6 |
| 41 | T00461den Model på Plateu.dfs0 | Regular | 30 | 82 | - | 5.5 | 14 | 1 | 90 | 1 | plateau/no struc | 36.6 |
| 42 | T00471den Model på Plateu.dfs0 | Regular | 30 | 82 | - | 11 | 14 | 1 | 90 | 1 | plateau/no struc | 36.6 |
| 43 | T00481den Model på Plateu.dfs0 | 2D | 30 | 82 | JONSWAP | 4.3 | 10.2 | 3 | 90 | 1 | plateau/no struc | 36.6 |
| 44 | T00491den Model på Plateu.dfs0 | 2D | 30 | 82 | JONSWAP | 8.3 | 10.2 | 3 | 90 | 1 | plateau/no struc | 36.6 |
| 45 | T00501den Model på Plateu.dfs0 | 3D | 30 | 82 | JONSWAP | 4.3 | 10.2 | 3 | 90 | 12.5 | plateau/no struc | 36.6 |
| 46 | T00511den Model på Plateu.dfs0 | 3D | 30 | 82 | JONSWAP | 8.3 | 12.6 | 3 | 90 | 12.5 | plateau/no struc | 36.6 |
| 47 | T00521den Model på Plateu.dfs0 | none | 0 | Oscilation tests to document the force gauge response and dampening | | | | | | - | - | 36.6-stiff |
| 48 | T00531Med Model på Plateu.dfs0 | Regular | 30 | 82 | - | 5.5 | 14 | 1 | 90 | 1 | plateau | 36.6-stiff |
| 49 | T00541Med Model på Plateu.dfs0 | Regular | 30 | 82 | - | 8 | 14 | 1 | 90 | 1 | plateau | 36.6-stiff |
| 50 | T00551Med Model på Plateu.dfs0 | Regular | 30 | 82 | - | 11 | 14 | 1 | 90 | 1 | plateau | 36.6-stiff |
| 51 | T00571Med Model på Plateu.dfs0 | Regular | 30 | 82 | - | 11 | 10.2 | 1 | 90 | 1 | plateau | 36.6-stiff |
| 52 | T00581Med Model på Plateu.dfs0 | 2D | 30 | 82 | JONSWAP | 4.3 | 10.2 | 3 | 90 | 1 | plateau | 36.6-stiff |
| 53 | T00591Med Model på Plateu.dfs0 | 2D | 30 | 82 | JONSWAP | 6 | 10.7 | 3 | 90 | 1 | plateau | 36.6-stiff |
| 54 | T00601Med Model på Plateu.dfs0 | 2D | 30 | 82 | JONSWAP | 8.3 | 10.2 | 3 | 90 | 1 | plateau | 36.6-stiff |
| 55 | T00611Med Model på Plateu.dfs0 | 2D | 30 | 82 | JONSWAP | 8.3 | 12.6 | 24 | 90 | 1 | plateau | 36.6-stiff |
| 56 | T00621Med Model på Plateu.dfs0 | 3D | 30 | 82 | JONSWAP | 4.3 | 10.2 | 3 | 90 | 12.5 | plateau | 36.6-stiff |
| 57 | T00631Med Model på Plateu.dfs0 | 3D | 30 | 82 | JONSWAP | 6 | 10.7 | 3 | 90 | 12.5 | plateau | 36.6-stiff |
| 58 | T00641Med Model på Plateu.dfs0 | 3D | 30 | 82 | JONSWAP | 7 | 11.6 | 3 | 90 | 12.5 | plateau | 36.6-stiff |
| 59 | T00651Med Model på Plateu.dfs0 | 3D | 30 | 82 | JONSWAP | 8.3 | 12.6 | 3 | 90 | 12.5 | plateau | 36.6-stiff |

*Table 14*: TestMatrix 1/2.

| No | File | Wave type | Water Depth at Wave maker | W/L Lab | Spectrum | Target Wave height Hm0,i | Period / Peak Period Tp | Duration | Wave direction | Wave spreading | Placement | Model |
|---|---|---|---|---|---|---|---|---|---|---|---|---|
| - | name | | (m) | (cm) | | (m) | (s) | (hr) | (deg) | (-) | | |
| 60 | T0066Flexible Model.dfs0 | Regular | 62.4 | 78 | - | 5.5 | 14 | 1 | 90 | 1 | slope | 80 flex |
| 61 | T0067Flexible Model.dfs0 | Regular | 62.4 | 78 | - | 8 | 14 | 1 | 90 | 1 | slope | 80 flex |
| 62 | T0068Flexible Model.dfs0 | 2D | 62.4 | 78 | JONSWAP | 11 | 14 | 1 | 90 | 1 | slope | 80 flex |
| 63 | T0069Flexible Model.dfs0 | 2D | 62.4 | 78 | JONSWAP | 11 | 10.2 | 1 | 90 | 1 | slope | 80 flex |
| 64 | T0070Flexible Model.dfs0 | 3D | 62.4 | 78 | JONSWAP | 4.3 | 10.2 | 3 | 90 | 1 | slope | 80 flex |
| 65 | T0071Flexible Model.dfs0 | 3D | 62.4 | 78 | JONSWAP | 6 | 10.7 | 3 | 90 | 1 | slope | 80 flex |
| 66 | T0072Flexible Model.dfs0 | Regular | 52.4 | 65.5 | - | 8 | 14 | 1 | 90 | 1 | slope | 80 flex |
| 67 | T0073Flexible Model.dfs0 | Regular | 52.4 | 65.5 | - | 11 | 14 | 1 | 90 | 1 | slope | 80 flex |
| 68 | T0074Flexible Model.dfs0 | 2D | 52.4 | 65.5 | JONSWAP | 8.3 | 12.6 | 3 | 90 | 1 | slope | 80 flex |
| 69 | T0075Flexible Model.dfs0 | 2D | 52.4 | 65.5 | JONSWAP | 11 | 14 | 3 | 90 | 1 | slope | 80 flex |
| 70 | T0076Flexible Model.dfs0 | 3D | 52.4 | 65.5 | JONSWAP | 8.3 | 12.6 | 3 | 90 | 12.5 | slope | 80 flex |
| 71 | T0077Flexible Model.dfs0 | 3D | 52.4 | 65.5 | JONSWAP | 11 | 14 | 3 | 90 | 12.5 | slope | 80 flex |
| 72 | T0078Flexible Model.dfs0 | Regular | 42.4 | 53 | - | 8 | 14 | 1 | 90 | 1 | slope | 80 flex |
| 73 | T0079Flexible Model.dfs0 | Regular | 42.4 | 53 | - | 11 | 14 | 1 | 90 | 1 | slope | 80 flex |
| 74 | T0080Flexible Model.dfs0 | 2D | 42.4 | 53 | JONSWAP | 8.3 | 12.6 | 3 | 90 | 1 | slope | 80 flex |
| 75 | T0081Flexible Model.dfs0 | 2D | 42.4 | 53 | JONSWAP | 11 | 14 | 3 | 90 | 1 | slope | 80 flex |
| 76 | T0082Flexible Model.dfs0 | 3D | 42.4 | 53 | JONSWAP | 8.3 | 12.6 | 3 | 90 | 12.5 | slope | 80 flex |
| 77 | T0083Flexible Model.dfs0 | 3D | 42.4 | 53 | JONSWAP | 11 | 14 | 3 | 90 | 12.5 | slope | 80 flex |
| 78 | T0084Stiff Model Scale 80.dfs0 | Regular | 62.4 | 78 | - | 8 | 14 | 1 | 90 | 1 | slope | 80 stiff |
| 79 | T0085Stiff Model Scale 80.dfs0 | Regular | 62.4 | 78 | - | 11 | 14 | 1 | 90 | 1 | slope | 80 stiff |
| 80 | T0086Stiff Model Scale 80.dfs0 | 2D | 62.4 | 78 | JONSWAP | 8.3 | 12.6 | 3 | 90 | 1 | slope | 80 stiff |
| 81 | T0087Stiff Model Scale 80.dfs0 | 2D | 62.4 | 78 | JONSWAP | 11 | 14 | 3 | 90 | 1 | slope | 80 stiff |
| 82 | T0088Stiff Model Scale 80.dfs0 | 3D | 62.4 | 78 | JONSWAP | 8.3 | 12.6 | 3 | 90 | 12.5 | slope | 80 stiff |
| 83 | T0089Stiff Model Scale 80.dfs0 | 3D | 62.4 | 78 | JONSWAP | 11 | 14 | 3 | 90 | 12.5 | slope | 80 stiff |
| 84 | T0090Stiff Model Scale 80.dfs0 | Regular | 52.4 | 65.5 | - | 8 | 14 | 1 | 90 | 1 | slope | 80 stiff |
| 85 | T0091Stiff Model Scale 80.dfs0 | Regular | 52.4 | 65.5 | - | 11 | 14 | 1 | 90 | 1 | slope | 80 stiff |
| 86 | T0092Stiff Model Scale 80.dfs0 | 2D | 52.4 | 65.5 | JONSWAP | 8.3 | 12.6 | 3 | 90 | 1 | slope | 80 stiff |
| 87 | T0093Stiff Model Scale 80.dfs0 | 2D | 52.4 | 65.5 | JONSWAP | 11 | 14 | 3 | 90 | 1 | slope | 80 stiff |
| 88 | T0094Stiff Model Scale 80.dfs0 | 3D | 52.4 | 65.5 | JONSWAP | 8.3 | 12.6 | 3 | 90 | 12.5 | slope | 80 stiff |
| 89 | T0095Stiff Model Scale 80.dfs0 | 3D | 52.4 | 65.5 | JONSWAP | 11 | 14 | 3 | 90 | 12.5 | slope | 80 stiff |
| 90 | T0096Stiff Model Scale 80.dfs0 | Regular | 42.4 | 53 | - | 8 | 14 | 1 | 90 | 1 | slope | 80 stiff |
| 91 | T0097Stiff Model Scale 80.dfs0 | Regular | 42.4 | 53 | - | 11 | 14 | 1 | 90 | 1 | slope | 80 stiff |
| 92 | T0098Stiff Model Scale 80.dfs0 | 2D | 42.4 | 53 | JONSWAP | 8.3 | 12.6 | 3 | 90 | 1 | slope | 80 stiff |
| 93 | T0099Stiff Model Scale 80.dfs0 | 2D | 42.4 | 53 | JONSWAP | 11 | 14 | 3 | 90 | 1 | slope | 80 stiff |
| 94 | T0100Stiff Model Scale 80.dfs0 | 3D | 42.4 | 53 | JONSWAP | 8.3 | 12.6 | 3 | 90 | 12.5 | slope | 80 stiff |
| 95 | T0101Stiff Model Scale 80.dfs0 | 3D | 42.4 | 53 | JONSWAP | 11 | 14 | 3 | 90 | 12.5 | slope | 80 stiff |
| 96 | T0102Stiff Model Scale 80.dfs0 | 3D | 42.4 | 53 | JONSWAP | 11 | 14 | 3 | 90 | 12.5 | slope | 80 stiff |
| 97 | T0103Stiff Model Scale 80.dfs0 | 3D | 42.4 | 53 | JONSWAP | 11 | 14 | 3 | 90 | 12.5 | slope | 80 stiff |
| 98 | T0104Stiff Model Scale 80.dfs0 | 3D | 42.4 | 53 | JONSWAP | 11 | 14 | 3 | 90 | 12.5 | slope | 80 stiff |
| 99 | T0105Stiff Model Scale 80.dfs0 | 2D | 42.4 | 53 | JONSWAP | 15.7 | 14 | 3 | 90 | 1 | slope | 80 stiff |
| 100 | T00166Flexible Model.dfs0 | none | 0 | 0 | Oscilation tests to document the response and dampening of the flexible model | | | | | - | slope | 80 flex |
| 101 | T00167Flexible Model.dfs0 | none | 0 | 0 | Oscilation tests to document the response and dampening of the flexible model | | | | | - | slope | 80 flex |
| 102 | T00168Flexible Model.dfs0 | none | 0 | 0 | Oscilation tests to document the response and dampening of the flexible model | | | | | - | slope | 80 flex |
| 103 | T00169Flexible Model.dfs0 | none | 0 | 0 | Oscilation tests to document the response and dampening of the flexible model | | | | | - | slope | 80 flex |
| 104 | T00173Flexible Model.dfs0 | none | 0 | 0 | Oscilation tests to document the response and dampening of the flexible model | | | | | - | slope | 80 flex |
| 105 | T00174Flexible Model.dfs0 | none | 0 | 0 | Oscilation tests to document the response and dampening of the flexible model | | | | | - | slope | 80 flex |
| 106 | T00175Flexible Model.dfs0 | none | 0 | 0 | Oscilation tests to document the response and dampening of the flexible model | | | | | - | slope | 80 flex |

*Table 15*: TestMatrix 2/2.

## 6.3 Examples of results

Sample results for regular wave tests are shown in figure 75 in laboratory scale. The left panels show a weakly nonlinear wave measured with the flexible structure at scale 1:80. The right panels show a strongly nonlinear wave at scale 1:36.6. Both waves have a period of 14 s and a wave height of 11 m, but occur at depths of 40.8 m and 17.2 m respectively (full scale parameters). This gives rise to a large difference in their behaviour. While the 17.2 m wave surface elevation signal (upper panel) has asymmetric, spiky crests and long flat troughs, the 40.8 m wave is almost sinusoidally shaped. Similar observations are made for the force signals (lower panels). The weakly nonlinear force signal is almost sinusoidal while the strongly nonlinear force signal show clear asymmetry along with excitation of the structures natural frequency. A low-pass filtered force signal (cut-off frequency of 5 Hz, lab scale) is shown as well and reveals a secondary load cycle after the main force peak. A similar filter was applied to the weakly nonlinear force signal (cut-off frequency of 6.5 Hz, lab scale) resulting in a slight smoothing around the maximum of the force curve.

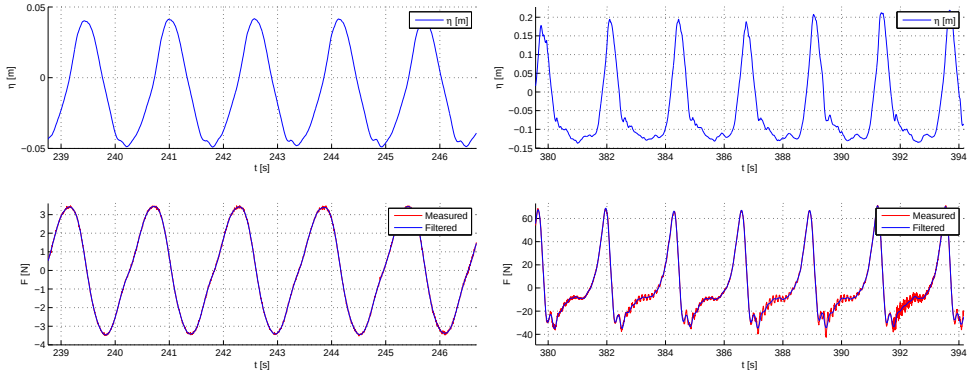


*Figure 75*: Sample results for regular waves in terms of free surface elevation and inline force. Lab scale. Left: Weakly nonlinear wave for the 1:80 flexible structure (test 59, $H = 8$ m, $T = 14$ s, $h = 40.8$ m). Right: Strongly nonlinear waves at scale 1:36.6 (test 14, $H = 11$ m, $T = 14$ s, $h = 17.2$ m).

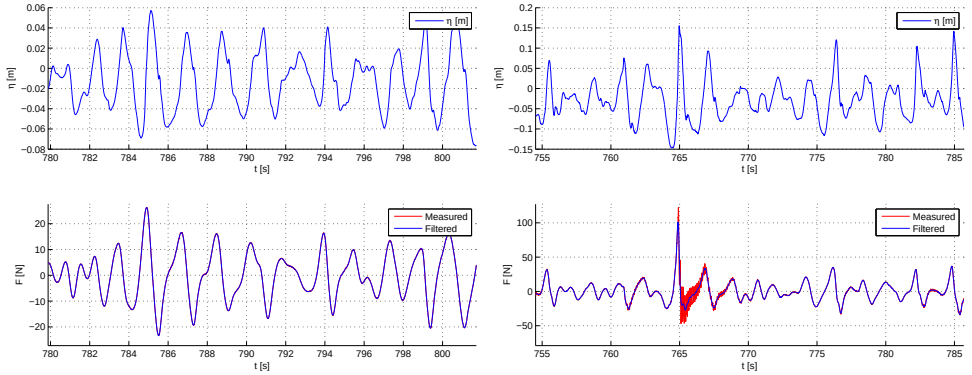


*Figure 76*: Sample results for irregular 3D waves at scale 1:36.6 and a full-scale depth of 17.2 m. Left: test 18 with $H_s = 4.3$ m, $T_p = 10.2$ s. Right: test 20 with $H_s = 8.3$ m, $T_p = 12.6$ s.

Two examples of irregular wave measurements are shown in figure 76, still in lab units. Both are for 3D waves at the slope at scale 1:36.6. The full scale parameters wave parameters are $H_s = 4.3$ m, $T_p = 10.2$ s for the left panel (test 18) and $H_s = 8.3$ m, $T_p = 12.6$ s for the right panels (test 20). The latter test is thus more nonlinear than the first which is also evident from

the larger values of crest wave height and the much stronger peak forces. Again, for the largest wave in the example, the wave impact excites the structures natural frequency at 9 Hz. Most of the vibrations are eliminated by low-pass filtering the force signal (cut-off at 5.0 Hz, blue curve), which however is seen affect the peak force. The filtered signal exhibits a secondary load cycle.

## 6.4 A probabilistic model for inline force

The measured peak forces for tests 5–8 have been analysed by Hansen et al. (2012) and a probabilistic model was fitted to the data. This is summarized in the following. The four tests are for 2D irregular waves for the cylinder placed on the slope at a full scale depth of 20.2 m. A zero down-crossing analysis was applied to the free surface elevation signal and the maximum force was recorded for each wave. Figure 77(left) shows a probability plot of wave height for test 5 and 8, the ones with the smallest and largest waves, respectively. For both tests, the distribution of Forristall (1978) provides a good fit to the data. It should be noted though, that for test 6 a better fit was obtained with the Rayleigh distribution, see Hansen et al. (2012). The scatter plot in the left figure panel shows an almost proportional relation between wave height and peak peak force exists for the smallest waves, while considerable scatter occur for the larger waves.

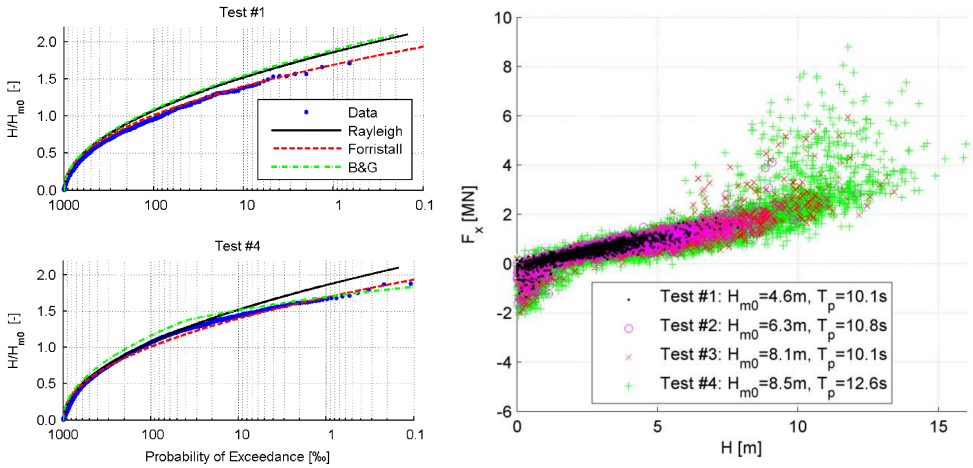


*Figure 77*: Left: Probability plot of wave height for tests 5 and 8. Right: Scatter plot of inline force against wave height, tests 5–8. From Hansen et al. (2012).

An interesting observation was made by mapping the peak forces according to the deep water steepness $H/L_0$ and the dimensionless depth $h/L_0$ (or $d/L_0$). Here, $L_0 = gT^2/(2\pi)$ is the deep water wave length for the wave period of the down crossing analysis and $g$ is the acceleration of gravity. Such a plot is presented in figure 78(left) along with contour lines of the breaking parameter $A$ for the breaking criterion of Goda (2010) and the Ursell number $Ur = HL_0^2/h^3$. The Goda breaking criterion reads

$$\frac{H_b}{L_0} = A\left\{1 - \exp\left(-1.5\pi\frac{h}{L_0}(1+\tan^{4/3}\theta)\right)\right\}. \tag{60}$$

where $\theta$ is the bed slope and $H_b$ is the breaking wave height. Wave breaking for irregular waves occur for $0.12 < A < 0.18$ which are contoured in the plot. The plot shows that the largest peak forces occur within the breaking region defined by the breaking criterion and is also associated with a certain range of the Ursell number.

This led to the development of a probabilistic model for the peak forces, where the mean value and its standard deviation was parameterized in terms of $A$ and $Ur$. The obtained fit is

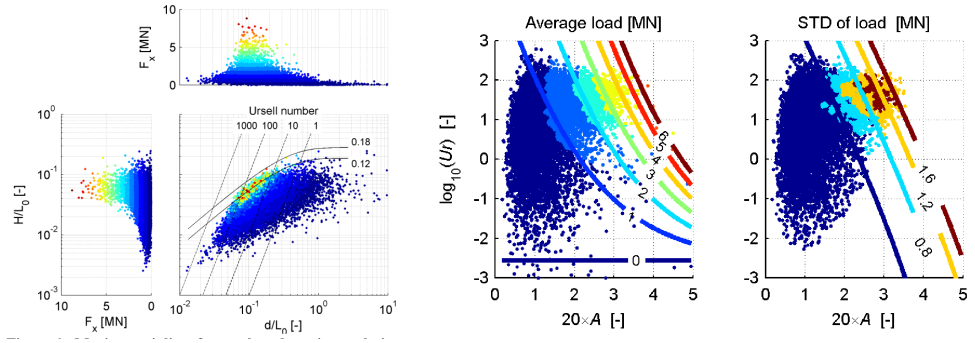


*Figure 78*: Left: Peak inline force versus dimensionless depth $d/L_0$ and wave steepness $H/L_0$. Ursell number and breaking index $A$ are marked as contour lines. Right: Mean and standard deviation of peak inline force as function of Ursell number and breaking index. From Hansen et al. (2012).

shown in figure 78(right) and involves determination of six constants for the mean and standard deviation, respectively. The model can be used for direct simulation of short term probability distributions of wave forces, based on realizations of free surface elevation from wave spectra. This is achieved by performing a zero down crossing analysis on the simulated wave time series. Next for each individual wave, the inline force is determined as the fitted mean value plus a stochastic contribution picked randomly from a normal distribution with the model-predicted standard deviation. Output of this model was compared directly to the measurements in the paper.

The long term distribution of inline force can also be established with basis in the fitted model. This involves convolution of the long-term distribution of most probable wave heights with the short-term variability of the maximum wave height conditional on its most probable value. The method is a variant of the one of Tromans & Vanderschuren (1995). Details and an example of application is given in Hansen et al. (2012).

## 6.5 The effect of directional spreading on the inline force

The effect of 3D directional spreading of the waves has great practical interest. For smaller waves it is well established that directional spreading reduces the loads, simply due to the reduction of load in the main direction by projection of the individual waves. Directional wave propagation, however, may result in a changed wave height distribution, especially for the largest waves that are affected by wave breaking. While for unidirectional waves, focusing of large waves can only occur by simple overtaking of individual waves with different phase speeds, directional focusing can happen by simple path crossing of two wave groups. This allows for generation of higher transient waves before wave breaking reduces the height and thus leads to a possibility for larger extreme forces than in the unidirectional case. This effect was observed in the CFD investigation of unidirectional and bi-directional focused waves of section 3.5 for the largest wave steepness of $k_pA = 0.33$.

The effect of directional spreading on the inline force has been analysed by Nielsen et al. (2012) with basis in 57 of the conducted tests. The applied test results thus include both scales and the placement of the cylinder at the slope as well as the plateau. Figure 79(left) shows a plot of the two usual parameters to measure the spreading, $n$ and $\phi$. While $n$ is the power of the $\cos^n\theta$ directional spectrum, $\phi = \sigma_{uu}/\sigma_V$ is the ratio of the standard deviations of the projected horizontal particle velocity in the main wave direction and the standard deviation of the velocity signal if all components were in the main wave direction (Forristall & Ewans 1998). The spreading factor $\phi$ lies in the interval $[\sqrt{2}/2;1]$ where corresponding to omni-directional and

unidirectional waves, respectively. The figure shows that even the nominal 2D wave fields show some directional spreading and confirms (with some scatter) the monotonic relation between $n$ and $\phi$. Next, for each test, the peak inline force was compared to an estimate based on linear wave theory applied to the measured surface elevation signal and the Morison equation with case-specific force coefficients $(C_M, C_D)$. The associated probability plot is shown in the right panel of the figure. Breaking waves (according to Godas breaking criterion with $A > 0.12$) are indicated by crosses. The Morison-based force is plotted for the same waves and shows conceivable scatter. This can be eliminated by re-ordering of the points or by application of an averaging filter across the points. The red curve was obtained this way. The effect of directionality on the extreme wave forces were quantified by expressing the difference between the 5% largest observed forces and the Morison force estimate by a slamming force with a slamming coefficient. For each test, an average slamming coefficient could be determined and the correlation to the spreading factor $\phi$ be plotted. The correlation however, showed appreciable scatter and did not provide a clear answer as to the potential reduction of the extreme forces for the breaking waves.

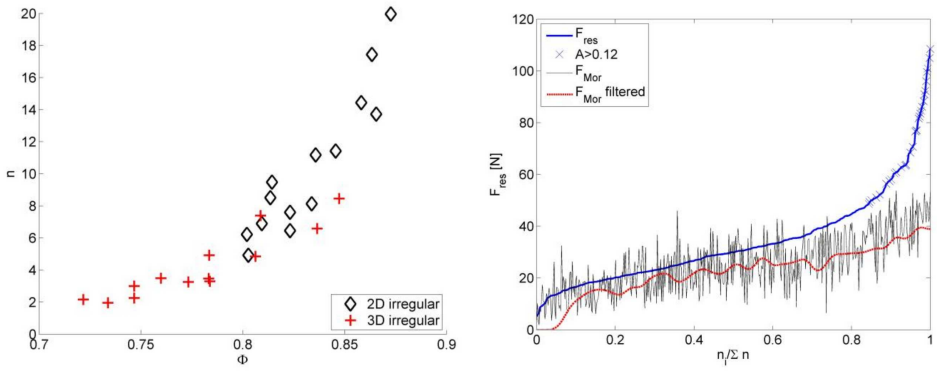


*Figure 79*: Left: Spreading index $n$ and spreading factor $\phi$ for the analysed tests measured at the wave maker. Right: Probability plot of peak forces from a single test and comparison to the estimated forces from the Morison equation. From Nielsen et al. (2012).

A data-driven analysis of the 2D 1:80 irregular tests was made by Slabiak & Sahlberg-Nielsen (2013). Figure 80 shows a comparison between 2D and 3D tests for the three depths of 20.8 m, 30.8 m and 40.8 m. It can be seen that for almost all the tests, the directional spreading reduces the inline forces. For the largest wave height at the depth of 40.8 m, however, the extreme wave impacts are larger in 3D than in 2D. This may be due to the effect of rapid focusing for directionally spread waves.

More analysis of the data set with respect to the effect of directionality is ongoing.

## 6.6 Excitation of the flexible structure by steep and breaking waves

The flexible structure at scale 1:80 was designed to study structural excitation by steep and breaking waves. Bredmose et al. (2013) presented an analysis of 2D irregular wave forces (tests 62–63,68–69,74–75) and the resulting structural response at the pile. The paper further presents the design approach for the flexible structure and two examples of numerical reproduction of the experiments with a fully nonlinear potential flow wave model and a finite element structural model.

Figure 81 provide two scatter plots of the peak accelerations, mapped against the deep water wave steepness $H/L_0$ and dimensionless depth $h/L_0$, similarly to the plot by Hansen et al. (2012). The values have been obtained from a zero down crossing analysis of the surface

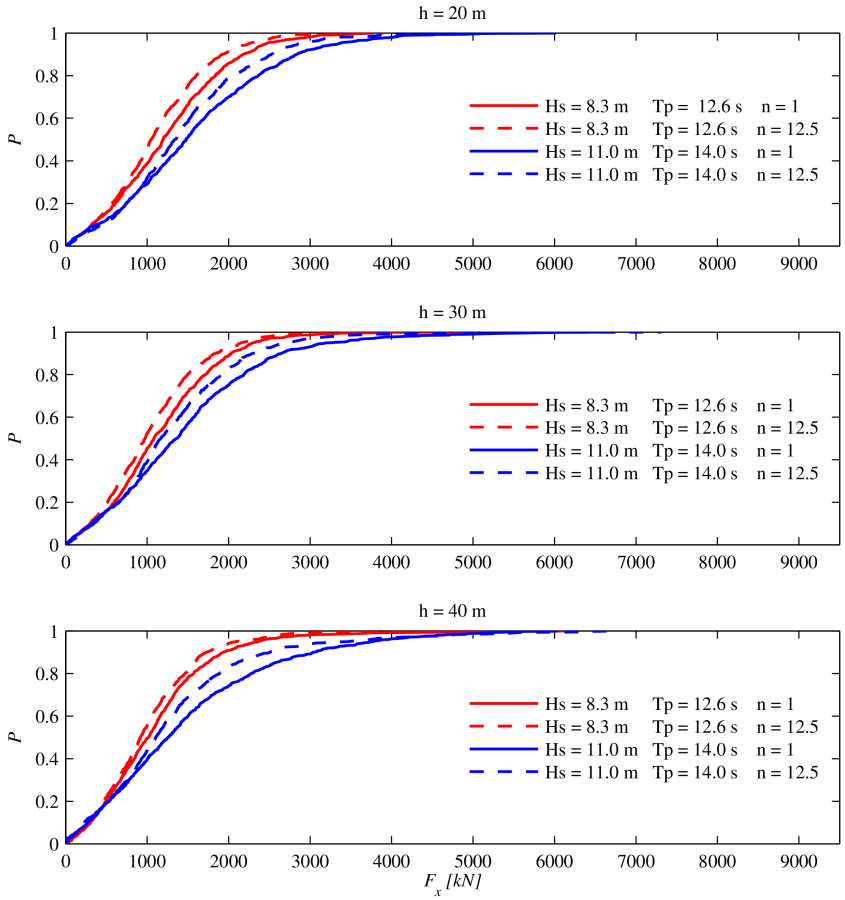


*Figure 80*: Probability curves at scale 1:80 for inline force. Effect of directional spreading. From Slabiak & Sahlberg-Nielsen (2013).

elevation signal combined with the measured accelerations in the upper transducer. The left panel is for a full scale depth of 40.8 m and significant wave height of 8.3 m (test 62) while the left panel is for a depth of 20.8 m and a significant wave height of 11.0 m (test 75). The two plots illustrate that for most waves, the accelerations are larger at the depth of 40.8 m than at 20.8 m. This must be due to the larger relative extent of the water column and the increased 'moment arm' for the wave forces close to the free surface. The largest accelerations occur in the breaking zone, as marked by the Goda (2010) criterion with $A = (0.12, 0.18)$ in the figure. Further, the most extreme accelerations in the six tests occur at the smallest depth of 20.8 m and for breaking waves. This can be linked to the increased nonlinearity at this depth, which causes wave breaking for the largest waves.

The sectional force between the structure and the basin bottom was measured by a force transducer was analysed as part of the zero-crossing analysis. This is shown in the probability plots of figure 82. Apart from one extreme event at the depth of 20.8 m, the forces for $H_s = 11$ m are larger than the forces for $H = 8.3$ m. Further, for both wave heights, the forces down to a certain exceedance probability level (5% and 20%, respectively) are largest for the largest depth, while for smaller exceedance probabilities the smallest depth shows the largest forces. This can be explained by the larger moment arm at the large depth for the main wave population and the more extreme breaking at shallow water for the largest waves.

Two examples of measured events and their numerical reproduction are given in figures 83 and 84 for tests 62 and 75, respectively. The numerical reproduction technique consists of 1) linear reconstruction of the incident wave field from wave gauges close to the wave maker; 2) direct

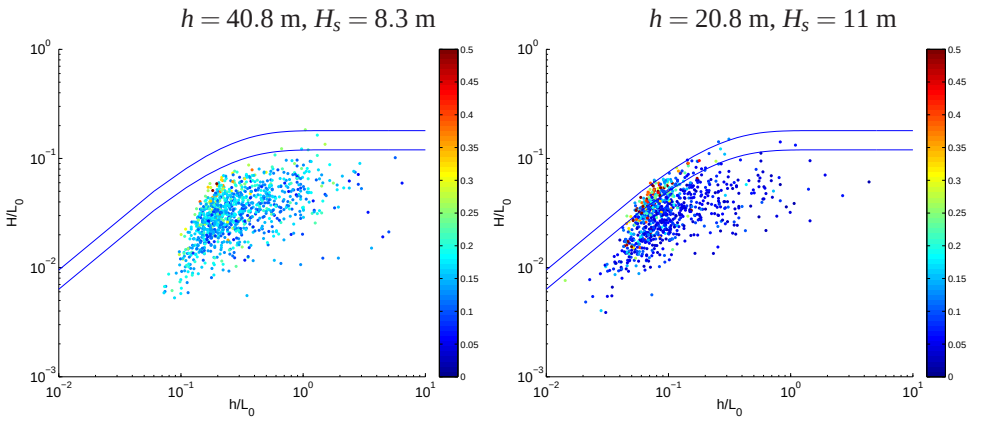


*Figure 81*: Scatter plot of maximum acceleration for the flexible structure, mapped according to individual wave parameters. The colour scale shows the acceleration in $m/s^2$. Left: test 62. Right: test 75.

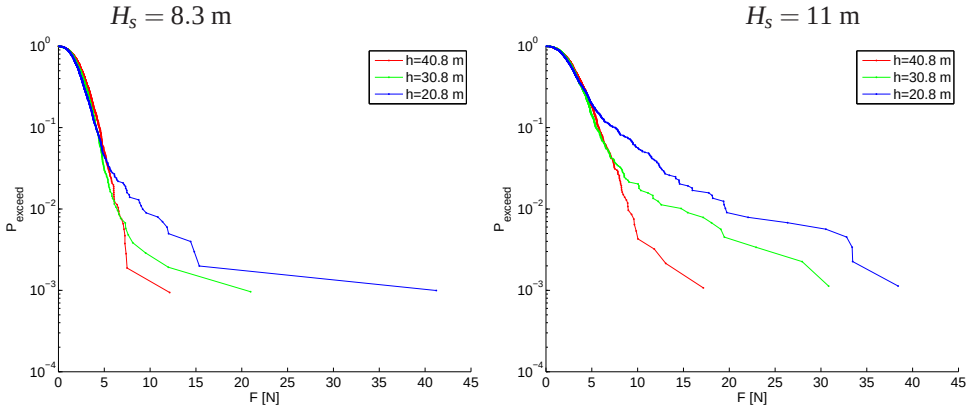


*Figure 82*: Empirical exceedance probability curve for sectional force.

computation of the wave motion with the fully nonlinear potential flow wave model of Engsig-Karup et al. (2009); 3) calculation of wave forcing at the position of the structure with the force model of Rainey (1995) and 4) response calculation in a time domain finite element model. The approach is detailed in the paper of Bredmose et al. (2013). The force model is an extension of the Morison equation, derived for fully nonlinear wave forcing of slender structures.

Test 62 is for a significant wave height of 8.3 m at a depth of 40.8 m (full scale values). The chosen event is the one associated with the largest force in the test. Generally, a good reproduction of the free surface elevation, bottom sectional force, structural acceleration and displacement is seen. The large wave at $t = 754$ s is seen to induce significant structural response at the natural frequency. This is reproduced well by the numerical model. For the somewhat weaker event at $t = 736$ s, however, the numerical response is seen to be over-predicted.

Similar plots test 75 at 20.8 m and with a significant wave height of 11.0 m are shown in figure 83. At this depth the waves are strongly nonlinear and wave breaking occur with larger probability. The waves are more peaky and the accelerations and forces are more extreme. In the episode shown, the structure is excited at both its first and second natural frequencies. This can be seen in the force and acceleration signals. For the event at $t = 786$ s, the numerical model is able to reproduce the structural excitation well, while for the steep wave groups at $t = (706, 712)$ s, the model underestimates the response. This illustrates the need for a force model that includes wave breaking, as the present force model of Rainey (1995) is intended for

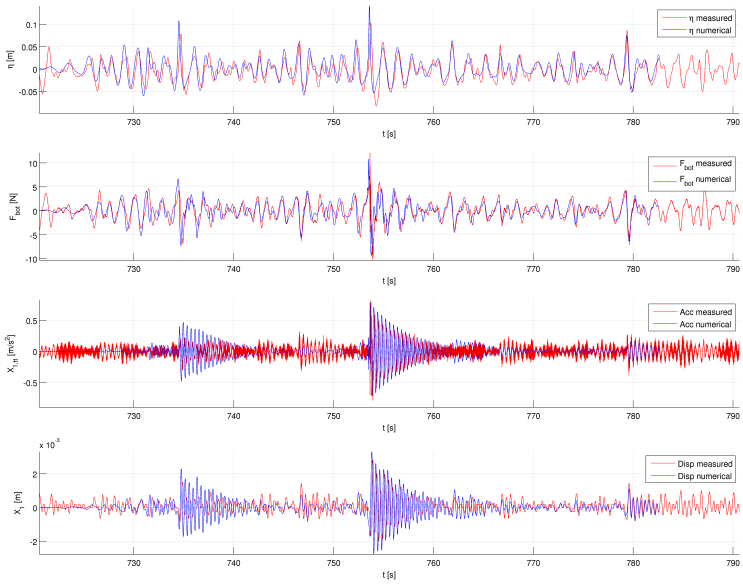


*Figure 83*: Comparison of measured and computed free surface elevation and structural response for the case at $h = 40.8$ m.

non-breaking waves.

As has been discussed in relation to task C, the structural response to breaking wave loads at shallow and intermediate depth can take the shape of impulsive excitation rather than the transient resonant response associated with classical ringing. The episodes of figure 84 are examples of this. Also, for figure 83, the event at $t = 754$ s is an example of impulsive excitation while the event at $t = 736$ s appear to be of ringing-type as it is seen to achieve its maximum amplitude in its second oscillation rather than at first.

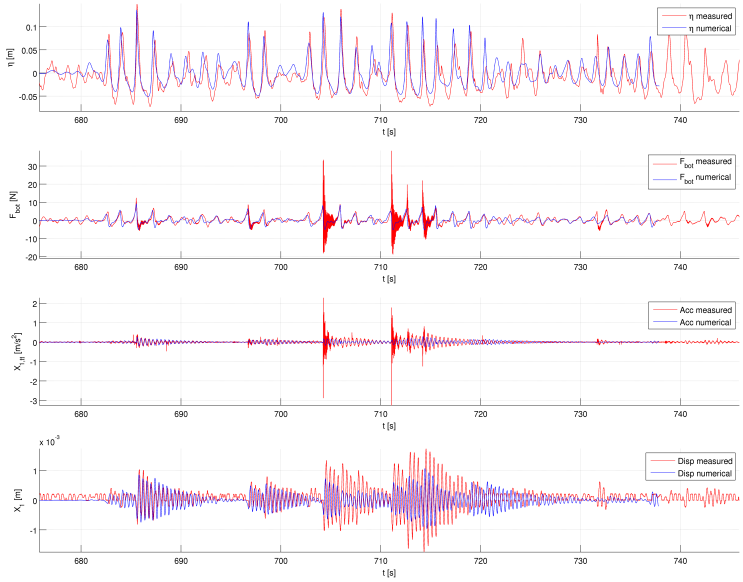


*Figure 84*: Comparison of measured and computed free surface elevation and structural response for the case at $h = 20.8$ m.

## 6.7 Further comparison between model test and experiment

The paper of Bredmose et al. (2013) has shown two examples of numerical reproduction for the flexible tests. Further comparisons are provided for the rigid structure in terms of CFD calculations in section 3 and the journal paper of Paulsen, Bredmose & Bingham (2013), the PhD thesis of Paulsen (2013) and the MSc project of Slabiak & Sahlberg-Nielsen (2013).

## 6.8 Summary

An all-round data set for wave loads on vertical cylinders has been established. The tests have been carried out at scale 1:36.6 with a rigid structure and at scale 1:80 with flexible and rigid structures. The flexible tests are novel as they allow a direct study of structural excitation and ringing from steep and breaking waves.

The measured data have been analysed with respect to peak inline forces and its dependence to individual wave parameters. The effect on the inline force from wave directionality has been analysed as well.

Successful numerical reproduction has been achieved for the flexible structure with a combined potential flow / finite element model as well as for the rigid structure with potential flow modelling and CFD.

The limitations of the data set associated with the large slope of 1:25 and structural excitation by steep waves of the rigid structures have been discussed. Further work in terms of detailed quantification of the slope effect, wave kinematics, 3D effects, current effects, detailed pressure measurements and the development of an improved force model have been suggested.

## 6.9 Suggestions for further work

The current data set provides a good basis for numerical model validation and analysis of wave loads data. More investigations, however, are needed for further validation of detailed force models and improved analysis. The following further steps are therefore recommended, all aiming at a reduction of the uncertainty on wave loads on offshore wind turbines:

- **Quantification of slope effect.** The occurrence of a too large laboratory slope is a common problem for model tests of wind turbine substructures. A quantification of this effect and establishment of a correction factor can be achieved by detailed experiments in a long wave flume combined with a numerical assessment of the wave kinematics.
- **Reduced vibrations.** Since the present experiments, techniques that reduces the problem of undesired structural vibrations have been developed at DHI. Further detailed experiments with eliminated vibrations are recommended.
- **Further quantification of 3D load effects.** The present experiments indicate that directional spreading generally reduces the wave loads. For the extreme wave loads, however, examples of increased loads for directionally spread waves have also been observed. This leaves a need for further detailed and accurate experiments to determine extreme forces from 3D waves. A combined experimental-numerical approach is recommended. The coupled potential flow CFD solver of task B will be ideal for this purpose.
- **Measurement of detailed kinematics by PIV.** For design purposes, the most feasible approach for steep and breaking wave loads is the combination of an accurate model for the undisturbed kinematics and a force model. The force model, however, requires validation against experiments. Therefore detailed measurements of steep and breaking wave kinematics are recommended. The PIV (Particle Image Velocimetry) method is well suited for this.

- **Detailed pressure measurements on structure.** The inline force is an integral measure of the distributed pressure on the structure. The spatial force distribution is determining for the extent of structural vibration and is provided by the numerical models. This must be validated against detailed measurements. The present data set involves measurement of pressures at five positions of the structure. Recent methods, however, allows more detailed and resolved measurements.

# References


API (2010), *Recommended Practice for Planning, Designing and Constructing Fixed Offshore PlatformsWorking Stress Design (API RP 2A-WSD)*, American petroleum institute.

Bredmose, H. & Jacobsen, N. G. (2010), Breaking wave impacts on offshore wind turbine foundations: focused wave groups and cfd, *in* 'International Conference on Ocean, Offshore and Arctic Engineering', Shanghai.

Bredmose, H. & Jacobsen, N. G. (2011), Vertical wave impacts on offshore wind turbine inspection platforms, *in* 'Proc. 30th Int. Conf. Ocean Offshore Arctic Engng.', ASME, Rotterdam, The Netherlands.

Bredmose, H., Agnon, Y., Madsen, P. & Schäffer, H. (2005), 'Wave transformation models with exact second-order transfer', *European Journal of Mechanics - B/Fluids* **24**(6), 659 – 682.

Bredmose, H., Hunt-Raby, A., Jayaratne, R. & Bullock, G. N. (2010), 'The ideal flip-through impact: experimental and numerical investigation', *Journal of Engineering Mathematics* **67**(1-2), 115–136.

Bredmose, H., Schløer, S. & Paulsen, B. (2012), Higher-harmonic response of a slender cantilever beam to fully nonlinear regular wave forcing, *in* 'Proceedings of the ASME 2012 31th International Conference on Ocean, Offshore and Arctic Engineering'.

Bredmose, H., Skourup, J., Hansen, E., Christensen, E., Pedersen, L. & Mitzlaff, A. (2006), 'Numerical reproduction of extreme wave loads on a gravity wind turbine foundation', *Volume 1: Offshore Technology; Offshore Wind Energy; Ocean Research Technology; LNG Specialty Symposium* pp. 279–287.

Bredmose, H., Slabiak, P., Sahlberg-Nielsen, L. & Schlütter, F. (2013), Dynamic excitation of monopiles by steep and breaking waves. Experimental and numerical study, *in* 'Proceedings of the ASME 2013 32st International Conference on Ocean, Offshore and Arctic Engineering'.

Cassidy, M., Eatock Taylor, R. & Houlsby, G. (2001), 'Analysis of jack-up units using a constrained NewWave methodology', *Applied Ocean Research* **23**(4), 221–234.

Chaplin, J. R., Rainey, R. T. & Yemm, R. (1997), 'Ringing of a vertical cylinder in waves', *Journal of Fluid Mechanics* **350**, 119–147.

Choi, S.-J., Lee, K.-H., Hong, K., Shin, S. H. & Gudmestad, O. T. (2013), 'Nonlinear wave forces on an offshore wind turbine foundation in shallow waters', *Int. J. Ocean System Engng.* **3**(2), 68–76.

Christensen, E. D. & Hansen, E. A. (2005), Extreme wave run-up on offshore wind turbine foundations, *in* 'Proc. MARINE 2005 — Computational Methods in Marine Engineering, Oslo, Norway'.

Christensen, E. D., Yde, L., Gravesen, H., Hansen, E. A., Tarp-Johansen, N. J. & Damsgaard, M. L. (2007), Wave loads on offshore wind turbine foundations in shallow water. engineering models versus refined flow modelling, *in* 'Proceedings of the European Offshore Wind Conference, Berlin, Germany', EWEA.

Christensen, E., Lohmann, I., Hansen, H., Haerens, P., Mercelis, P. & Demuynck, A. (2011), Irregular wave loads on a gravity based foundation in shallow water, *in* 'Proc. 30th Int. Conf. Offshore Mech. Arctic Engng., Rotterdam, The Netherlands', ASME.

de Ridder, E., Aalberts, P., van den Berg, J., Buchner, B. & Peeringa, J. (2011), The dynamic response of an offshore wind turbine with realistic flexibility to breaking wave impact, *in* 'Proceedings of the 30th International Conference on Ocean, Offshore and Arctic Engineering'.

DHI (2012), *Mike 21 Toolbox - Mike by DHI 2012*, chapter 14. Generation of random waves, pp. 153–170.

DNV-OS-J101 (2010), *Design of Offshore Wind Turbines*, Det Norske Veritas.

Engsig-Karup, A., Bingham, H. & Lindberg, O. (2009), 'An efficient flexible-order model for 3D nonlinear water waves', *Journal of Computational Physics* **228**(6), 2100–2118.

Faltinsen, O. (1993), *Sea Loads on Ships and Offshore Structures*, Campridge University Press.

Faltinsen, O. M., Newman, J. N. & Vinje, T. (1995), 'Nonlinear wave loads on a slender vertical cylinder', *Journal of Fluid Mechanics* **289**, 179–198.

Fenton, J. D. (1988), 'The numerical solution of steady water wave problems', *Computers & Geosciences* **14**(3), 357–368.

Fenton, J. D. (1990), Nonlinear wave theories, *in* L. Mehaute & D. Hanes, eds, 'Ocean Engineering', Vol. 9, Wiley, New York, pp. 1–18.

Fitzgerald, C., Grice, J., Taylor, P., Taylor, R. & Zang, J. (2012), Phase manipulation and the harmonic components of ringing froces on a surface piercing column, *in* 'International workshop for water waves and floating bodies, IWWWFB.', Copenhagen.

Forristall, G. & Ewans, K. (1998), 'Worldwide measurements of directional wave spreading', *Journal of Atmospheric And Oceanic Technology* **15**, 440–469.

Forristall, G. Z. (1978), 'On the statistical distribution of wave heights in a storm', *J. Geograp. Res.* pp. 2352–2358.

Goda, Y. (2010), 'Reanalysis of regular and random breaking wave statistics', *Coastal Engineering Journal* **52**(1), 71–106.

Grue, J. (2002), 'On four highly nonlinear phenomena in wave theory and marine hydrodynamics', *Applied Ocean Research* **24**(5), 261–274.

Grue, J. & Huseby, M. (2002), 'Higher-harmonic wave forces and ringing of vertical cylinders', *Applied Ocean Research* **24**(4), 203–214.

Hansen, A. M., Larsen, T. & Yde, L. (2013), Influence of foundation model complexity on the design loads for offshore WTG on jacket foundation, EWEA. Poster presented at European Wind Energy Conference & Exhibition, Vienna.

Hansen, H., Lohmann, I., rensen, J. S. & Schlütter, F. (2012), A model for long-term distribution of wave induced loads in steep and breaking shallow water waves, *in* 'Proc. of the ASME 31th 2012 Int. Conf. on Ocean, Offshore and Arctic Engng', ASME. Rio de Janeiro, Brazil.

Hansen, M. H., Gaunaa, M. & Madsen, H. (2004), A Beddoes-Leishman type dynamic stall model in state-space and indicial formulations, Technical Report Risø-R-1354(EN), Risoe National Laboratory.

Hededal, O. & Klinkvort, R. (2010), 'A new elasto-plastic spring element for cyclic loading of piles using the p-y-curve concept', *Numerical Methods in Geotechnical Engineering - Benz & Nordal (eds)*.

IEA (1990), *Expert Group Study on Recommended practices for Wind Turbine Testing and Evaluation. Part 3. Fatigue loads.*, 2 edn, International Energy Agency Programme for Research and Development on Wind Energy Conversion Systems.

Jacobsen, N., Fuhrman, D. & Fredsøe, J. (2012), 'A wave generation toolbox for the open-source CFD library : OpenFoam', *International Journal for Numerical Methods in Fluids* **70**, 1073–1088.

Jensen, B. (2012), Technical Note on: Extreme Wave Loads and Run-up on Circular Cylinders, Technical report, DHI, Hørsholm, DK-2970.

Jonkman, J. & Musial, W. (2010), Offshore code comparison collaboration (OC3) for IEA task 23 offshore wind technology and deployment, Technical report, National Renewable Energy Laboratory.

Jonkman, J., Butterfield, S., Musial, W. & Scott, G. (2009), Definition of a 5-MW reference wind turbine for offshore system development, Technical report, National Renewable Energy Laboratory.

Jonkman, J. M. (2009), 'Dynamics of Offshore Floating Wind TurbinesModel Development and Verification', (June), 459–492.

Kim, T., Hansen, A. M. & Branner, K. (2013), 'Development of an anisotropic beam finite element for composite wind turbine blades in multibody system', *Renewable Energy* **59**, 172–183.

Klinkvort, R. (2012), Centrifuge modelling of drained lateral pile - soil response, PhD thesis, The Technical University of Denmark, DTU Civil Engineering.

Kriebel, D. L. (1992), 'Nonlinear Wave Interaction With A Vertical Circular Cylinder. Part II: Wave Run-Up', *Ocean Engineering* **19**(1), 75–99.

Krokstad, J., Stansberg, C., Nestegard, A. & Marthinsen, T. (1998), 'A new nonslender ringing load approach verified against experiments', *Journal of Offshore Mechanics and Arctic Engineering* **120**(1), 20–29.

Larsen, T. J. & Hansen, A. (2007), How to HAWC2, the users manual, Technical Report Risø-R-1597(en), Risoe National Laboratory - Technical University of Denmark.

Larsen, T. J., Kim, T., Schløer, S. & Bredmose, H. (2011*a*), 'Comparisons of wave kinematics models for an offshore wind turbine mounted on a jacket substructure', Poster at EWEA Offshore Wind 2011,Amsterdam, The Netherlands. Amsterdam, The Netherlands, November 2011.

Larsen, T. J., Madsen, H., Larsen, G. & Hansen, K. (2012), 'Evaluation of the Dynamic Wake Meander Model for Loads and Power Production in the Egmond aan Zee Wind Farm', *Accepted for publication in Wind Energy*.

Larsen, T., Kim, T., Schløer, S. & Bredmose, H. (2011*b*), Comparisons of wave kinematics models for an offshore wind turbine mounted on a jacket substructure, *in* 'Proceedings of the EWEA, Offshore 2011, Amsterdam, Netherlands'.

Leishman, J. & Beddoes, T. (1986), A generalized model for airfoil unsteady aerodynamic behaviour and dynamic stall using the indicial method, *in* 'Proceeding of the 42end Annual Forum of the American Helicopter Society'.

Madsen, H. A., Riziotis, V., Zahle, F., Hansen, M., Snel, H., Grasso, F., Larsen, T., Politis, E. & Rasmussen, F. (2011), 'BEM Blade element momentum modeling of inflow with shear in comparison with Advanced Model Results.', *Wind Energy* **15(1)**, 63–81. doi:10.1002/we.493.

Madsen, P. & Sørensen, O. (1993), 'Bound waves and triad interactions in shallow water', *Ocean Engineering* **20**(4), 359 – 388.

Madsen, P. A., Bingham, H. B. & Schäffer, H. A. (2003), 'Boussinesq-type formulations for fully nonlinear and extremely dispersive water waves: Derivation and analysis', *Proc. Roy. Soc. Lond. A* **459**(2033), 1075–1104.

Malenica, v. & Molin, B. (1995), 'Third-harmonic wave diffraction by a vertical cylinder', *Journal of Fluid Mechanics* **302**, 203–229.

Mann, J. (1998), 'Wind Field Simulation', *Prob. Engng. Mech., Elsevier Science* **vol. 13**(no. 4), pp. 269–283.

Manners, W. & Rainey, R. (1992), 'Hydrodynamic forces on fixed submerged cylinders', *Proceedings of the Royal Society of London. Series A: Mathematical and Physical Sciences* **436**(1896), 13–32.

Mariegaard, J. S. (2011), Task A1: Boundary conditions for phase resolving wave models, Technical report, DHI.

Mariegaard, J. S. (2013), Task A3: Study of the applicability of a new method with second order wave generation, Technical report, DHI.

MegaVind (n.d.), 'Denmark — supplier of competitive offshore wind solutions. MegaVind's strategy for offshore wind research, development and demonstration'. The Danish Wind Industry Association.

Morison, J., O'Brien, M., Johnson, J. & Schaaf, S. (1950), 'The forces exerted by surface waves on piles', *Journal Of Petroleum Technology* **2**(5), 149–154.

Nielsen, A. W., Schlütter, F., Sørensen, J. V. T. & Bredmose, H. (2012), Wave loads on a monopile in 3D waves, *in* 'Proc. of the ASME 31th 2012 Int. Conf. on Ocean, Offshore and Arctic Engng', ASME. Rio de Janeiro, Brazil.

Nielsen, J. K. & Dam, C. (2012), Numerical reproduction of measured wave loads and response for a monopile foundation, BSc project, DTU Wind Energy.

Nielsen, K. B. & Mayer, S. (2004), 'Numerical prediction of green water incidents', *Ocean Engng* **31**, 363–399.

Ning, D., Zang, J., Liu, S., Eatock Taylor, R., Teng, B. & Taylor, P. (2009), 'Free-surface evolution and wave kinematics for nonlinear uni-directional focused wave groups', *Ocean Engineering* **36**(15-16), 1226–1243.

Øye, S. (1996), Flex4 simulation of wind turbine dynamics, *in* '28th IEA Meeting of Experts Concerning State of the Art of Aeroelastic Codes for Wind Turbine Calculationsn (available through International Energy Agency)'.

Paulsen, B., Bredmose, H. & Bingham, H. (2013), 'An efficient 3D domain decomposition strategy for violent wave loads on surface piercing circular cylinders', *Submitted for publication*.

Paulsen, B., Bredmose, H., Bingham, H. & Jacobsen, N. (2011), Higher-harmonic hydrodynamic wave loads on a bottom fixed circular cylinder at finite water depth, *in* 'Proc. Eur. Offshore Wind'.

Paulsen, B., Bredmose, H., Bingham, H. & Schløer, S. (2013), Steep wave loads from irregular waves on an offshore wind turbine foundation: Computation and experiment, *in* 'International Conference on Ocean, Offshore and Arctic Engineering', Nantes.

Paulsen, B. T. (2013), Efficient computations of wave loads on offshore structures, Ph.d. thesis, The Technical University of Denmark, Department of Mechanical Engineering.

Paulsen, B. T., Bredmose, H. & Bingham, H. B. (2012), Accurate computation of wave loads on a bottom fixed circular cylinder, *in* '27. International Workshop on Water Waves and Floating Bodies, Denmark', Vol. m, pp. 137—-140.

Paulsen, B. T., Bredmose, H. & Bingham, H. B. (2013), Focused wave impact on a vertical cylinder : Experiment , numerical reproduction and a note on higher harmonics, *in* 'IWWWFB28', Nantes.

Paulsen, B. T., Bredmose, H., Bingham, H. B. & Jacobsen, N. G. (2013), 'Forcing of a bottom mounted circular cylinder by steep regular water waves at finite depth.', *Submitted for publication*.

Popko, W., Vorpahl, F., Zuga, A., Kohlmeier, M., Jonkman, J., Robertson, A., Larsen, T., Yde, A., Stertr, K., Okstad, K. M., Nichols, J., Nygaard, T. A., Gao, Z., Manolas, D., Kim, K., Yu, Q., Shi, W., Park, H., Vsquez-Rojas, A., Dubois, J., Kaufer, D., Thomassen, P., de Ruiter, M. J., Peeringa, J. M., Zhiwen, H. & von Waaden, H. (2012), Offshore Code Comparison Collaboration Continuation (OC4), Phase I - Results of Coupled Simulations of an Offshore Wind Turbine with Jacket Support Structure., *in* 'Proceedings of the Twenty-second (2012) International Offshore and Polar Engineering Conference Rhodes, Greece, June 17-22'.

Rainey, R. C. T. (1989), 'A new equation for calculating wave loads on offshore structures', *Journal of Fluid Mechanics* **204**, 295–324.

Rainey, R. C. T. (1995), 'Slender-body expressions for the wave load on offshore structures', *Proceedings of the Royal Society of London* **450**, 391–416.

Sand, S. E. & Mynett, A. (1987), Directional wave generation and analysis, *in* 'Proc. IAHR Seminar on Wave Analysis and Generation in Laboratory Basins, 22nd IAHR Congress, Lausanne, Switzerland', pp. 209–235.

Schløer, S. (2013), Fatigue and extreme wave loads on bottom fixed offshore wind turbines. Effects from fully nonlinear wave forcing on the structural dynamics, PhD thesis, DTU Wind Energy.

Schløer, S., Bredmose, H. & Bingham, H. (2011), Irregular wave forces on monopile foundations. Effect of full nonlinearity and bed slope, *in* 'Proceedings of the ASME 2011 30th International Conference on Ocean, Offshore and Arctic Engineering'.

Schløer, S., Bredmose, H. & Bingham, H. (2014), 'Fully nonlinear wave forces and their effect on monopile wind turbines', *Journal paper manuscript at submission stage*.

Schløer, S., Bredmose, H., Bingham, H. & Larsen, T. (2012), Effects from fully nonlinear irregular wave forcing on the fatigue life of an offshore wind turbine and its monopile foundation., *in* 'Proceedings of the ASME 2012 31th International Conference on Ocean, Offshore and Arctic Engineering'.

Schlütter, F. (2013), Wave loads on offshore wind turbine foundations. experiment description, Technical report, DHI. Prepared for the ForskEL2010 Wave Loads project.

Sharma, J. & Dean, R. (1981), 'Second-order directional seas and associated wave forces', *Society of Petroleum Engineers Journal*.

Slabiak, P. & Sahlberg-Nielsen, L. (2013), Dynamics of a monopile structure in irregular waves: Experimental and numerical investigation, Master's thesis, DTU Wind Energy.

Sumer, B. M. & Fredsoe, J. (2006), *Hydrodynamics around cylindrical structures*, World Scientific.

Taylor, G. (1937), 'The spectrum of turbulence', *Proc. R. Soc. Lond. A* **164**, 476–490.

Theodorsen, T. (1935), 'General theory of aerodynamic instability and the mechanism of flutter', *NACA Report 435* pp. 413–433.

Tromans, P. S. & Vanderschuren, L. (1995), Response based design conditions in the North Sea: Application of a new method, *in* 'OTC', Vol. 7683, pp. 387–397.

Vogt, Y. (2013), 'Windmills at sea can break like matches', `http://www.apollon.uio.no/english/articles/2013/windmills.html`. Accessed: 2013-06-27.

Vorpahl, F., Popko, W. & Kaufer, D. (2011), Description of a basic model of the "UpWind reference jacket" for code comparison in the OC4 project under IEA Wind Annex 30., Technical report, Frauenhofer university.

Vorpahl, F., Strobel, M., Jonkman, J., Larsen, T., Passon, P. & Nichols, J. (2013), ' Verification of aero-elastic offshore wind turbine design codes under IEA Wind Task XXIII.', *Wind Energ.*

WAFO-Tutorial (2011), *WAFO -a Matlab Toolbox for Analysis of Random Waves and Loads*, Lund University.

Williams, J. (1981), 'Limiting gravity waves in water of finite depth', *Philosophical Transaction of the Royal Society of London. Series A, Mathematical and Physical Sciences* **302**(1466), 139–188.

Zang, J. & Taylor, P. (2011), Steep and breaking wave impacts on offshore wind turbine columns, *in* 'Proceedings on the Third International Conference on the Application of Physical Modelling to Port and Coastal Protection'.

Zang, J., Taylor, P. H. & Tello, M. (2010), 'Steep wave and breaking wave impact on offshore wind turbine foundations - Ringing re-visited', *International workshop for water waves and floating bodies, IWWWFB.*